# Tailoring Thermal Radiation from Near Field to Far Field

Thesis by
Junlong Kou

In Partial Fulfillment of the Requirements for the
degree of
Doctor of Philosophy


CALIFORNIA INSTITUTE OF TECHNOLOGY
Pasadena, California

2019
Defended May 10, 2019

Junlong Kou
ORCID: 0000-0002-0481-5149

# ACKNOWLEDGEMENTS

Time flies! Caltech is an amazing place that has had a great impact on my life, and the years I have spent here have been a great adventure!

First, I would like to thank Prof. Austin J. Minnich, who has kindly accepted me into his group to do research for years, for his passion and curiosity about science, his mild personality, and his genuine care for the students. I have learned and experienced quite a lot from him that has changed the way I think.

My thanks to the members of my thesis committee, Prof. Lihong Wang, Prof. Austin J. Minnich, Prof. Axel Scherer, and Prof. Alireza Marandi for their valuable time and constructive advice. Thanks to Prof. Azita Emami, and Prof. Andrei Faraon for giving advice on my candidacy. Thanks to Prof. Shanhui Fan from Stanford University for his valuable suggestions.

My thanks to the entire Minnich Group for your kind help and useful suggestions. You guys have made the group organized and vital. Thanks to Dr. Xiangwen Chen for initial guidance on e-beam lithography. Thanks to Zoila for being a great help on making polymer films. Thanks to Nate for machining the holder for my experiment. Thanks to Andrew, Jaeyun, and Yang for organizing the activities in the group. Thanks to Ruiqiang for helping on cluster computing. Thanks to Nick for suggestions on drawing figures. Thanks to Taeyong, Erika, Alex, Adrain for being wonderful office-mates and lab-mates.

My thanks to Dr. Guy Derose, Dr. Matthew Sullivan, Melissa Melendes, Steven Martinez, Nils Asplund, and Alireza Ghaffari for their guidance on operating the fabrication facilities. Thanks to Dr. Eric Black for guiding me on electronics and optics - it really helps!

My thanks to Prof. George R. Rossman for allowing and guiding me to use his UV-Vis and FTIR facilities for my measurement and show me those beautiful stones. Thanks to Dr. Bruce S. Brunschwig from MMRC and Dr. Ke Sun for training me on using Cary 5000.

My thanks to Peng for our long time friendship. I will always remember our enjoyable discussions on everything. Thanks to Dr. Jeong Oen Lee, for helping

me overcome the difficulties, for always talking and giving me suggestions during my journey. Thanks to Zhaoxian for always being my buddy and supporting me whenever you can. Thanks to Xinyu, Chengzhe, Cai, and Ziyang for inspiring me outside research field.

I received great support from many Caltech staff, including the wonderful EE and MCE administrative assistants, Owen Tanya, Christine Garske, Sonya Lincoln, and Lynn Seymour, as well as the IPS officers, Laura Flower Kim, and Daniel Yoder.

Finally, I would like to thank my family for their love and support throughout all my life. Thanks to my parents for raising me up and educating me throughout the years. Thanks to my siblings for your care and support. Thanks to Zhen and Ya for the happiness you bring to me.

# ABSTRACT

Control of heat flow in both near and far field through thermal radiation is of fundamental interest for applications in thermal management and energy conversion.

One challenge is how we can realize high contrast control of heat flow with high temporal frequencies and without moving parts. We try to resolve this problem and propose two schemes in the near field: one based on electrical tuning of silicon and the other based on optical pumping of doped silicon slabs. Both methods rely on the change of free carriers, leading to tuning of the plasma frequency, resulting in modulation of near-field thermal radiation. Calculations based on fluctuational electrodynamics show that the electric method gives 10% tuning range. On the other hand, heat transfer coefficient between two silicon films can be tuned from near zero to 600 $Wm^{-2}K^{-1}$ with a gap distance of 100 nm at room temperature with the optical pumping method.

In the far field, we predict and demonstrate two spectrally selective absorbers based on semiconductors, by utilizing their band gap properties and dedicated photonic structure design. The germanium photonic crystals have around 95% absorption from 500 nm to 1000 $\mu$m and over 0.9 over the entire visible and near infrared spectrum. The effective absorptivity is as high as 0.91. The black silicon achieves 100% absorption for light with wavelength under 1 $\mu$m. The effective absorptivity is as high as 0.96. Field test shows that black silicon is able to maintain at 130 degrees Celcius under unconcentrated condition.

Another interesting topic is to achieve over 100 $Wm^{-2}$ electricity-free cooling power density with simple fabrication method by passive radiative cooling under direction sunlight. We theoretically predicted three schemes for achieving this goal and experimentally demonstrate that a polymer-coated fused silica mirror, as a near-ideal black-body in the mid-infrared and near-ideal reflector in the solar spectrum, achieves radiative cooling below ambient air temperature under direct sunlight (8.2 °C) and at night (8.4 °C). Its performance exceeds that of a multi-layer thin film stack fabricated using vacuum deposition methods by nearly 3 °C. Furthermore, we estimate the cooler has an average net cooling power of about 127 $Wm^{-2}$ during daytime at ambient temperature, more than twice that reported previously, even

considering the significant influence of external conduction and convection. Our work demonstrates that abundant materials and straight-forward fabrication can be used to achieve daytime radiative cooling, advancing applications such as dry cooling of thermal power plants.

# PUBLISHED CONTENT AND CONTRIBUTIONS

Kou, Junlong and Austin J Minnich (2018). "Dynamic optical control of near-field radiative transfer". In: *Optics Express* 26.18, A729–A736. DOI: 10.1364/OE.26.00A729.

J. Kou performed the calculation and analysis, and wrote the manuscript.

Kou, Junlong, Zoila Jurado, Zhen Chen, Shanhui Fan, and Austin J Minnich (2017). "Daytime radiative cooling using near-black infrared emitters". In: *ACS Photonics* 4.3, pp. 626–630. DOI: 10.1021/acsphotonics.6b00991.

J. Kou designed the experiment, performed the deposition of the device, performed the measurement and analysis, and wrote the manuscript.

# TABLE OF CONTENTS

# LIST OF ILLUSTRATIONS

*Chapter 1*

# BACKGROUND

Thermophotonics studies the control of emission and absorption of materials and structures and utilizes them for various applications, such as, improving the efficiency of solar cells (L. Zhu, A. P. Raman, and Fan, 2015), dynamic control of heat flux (Ito et al., 2017; Ding, T. Kim, and Minnich, 2016), exploring new schemes of cooling (A. P. Raman et al., 2014; K. Chen, Santhanam, Sandhu, et al., 2015; Xiao et al., 2018), designing new structures for solar heat harvesting (Kraemer et al., 2011; Ni et al., 2016), etc. From the view point of spatial distance between objects involved, we can categorize the thermal radiation into near field (distance comparable to or less than thermal wavelength) and far field (distance much larger than thermal wavelength).

## 1.1 Near field radiative heat transfer

With the decreasing of feature sizes of electronic and photonic devices and the development of micro-/nano-fabrication techniques, the mass and energy transfer could occur in confined space down to micro-/nano-regime, leading to significantly different behaviour. One of such example is the thermal radiation between objects in the near field.

In the late 1960s, Prof. Tien's group from University of California, Berkeley and C. Hargreaves from Netherlands first noticed the enhanced radiation effect in the near field (E. Cravalho, Domoto, and C. Tien, 1968; E. G. Cravalho, C. L. Tien, and Caren, 1967; Hargreaves, 1969). However, the study of this anomalous phenomenon did not improve much due to the limited fabrication techniques.

Later in the late 2000s, Prof. Chen's group from MIT confirmed the strong deviation of near field radiation from what Stefan-Boltzmann's law predicts in the far field (Hu et al., 2008; Narayanaswamy, Shen, and G. Chen, 2008; Shen, Narayanaswamy, and G. Chen, 2009). Since then, tremendous attention has been paid in the last decade

due to the fundamental importance and great potential for applications of near field radiation. For example, Ito et al. used phase change material $VO_2$ to achieve dynamic modulation of heat flux for thermal management (Ito et al., 2017). Fiorino systematically studied the near field thermo-photovoltaics and demonstrated near 40-fold enhancement in the power output compared to the far field for energy recovery from low-quality waste heat at an emitter temperature of 655 K (Fiorino, L. Zhu, et al., 2018). Many other researchers proposed different theoretical ways to improve the outpower and efficiency leveraging on the near field effect (Tong et al., 2015; K. Chen, Santhanam, and Fan, 2015; J. Z.-J. Lau and Wong, 2017; Bierman et al., 2016; Inoue, Watanabe, et al., 2018; Karalis and Joannopoulos, 2016; Zhao et al., 2017; S Basu, Y.-B. Chen, and ZM Zhang, 2007). More recently, Zhu et al.. experimentally demonstrated near field photonic cooling without lasers by controlling the chemical potential of the photons inside semiconductors, pointing out a new method of solid state refrigeration and chip-scale cooling (L. Zhu, Fiorino, et al., 2019).

Measuring the near field effect is extremely difficult due mainly to the requirements of surface smoothness and nanoscele gap distance and parallelism control over large area. Tremendous progress on detailed measurement and confirmation has been made from Prof. Reddy's group from University of Michigan to overcome the challenges involved (Jeong et al., 2015; B. Song, Ganjeh, et al., 2015; K. Kim et al., 2015; B. Song, Thompson, et al., 2016; L. Cui et al., 2017; Fiorino, Thompson, et al., 2018). Specifically, nanopositioning, calorimetry, and thermometry have enabled Prof. Reddy's group to precisely control the distance and angle for planar structures, as well as measure the temperature, and heat flux, as shown in Figure 1.1.

## 1.2 Far field radiative heat transfer

Far field radiative heat transfer has a much longer history than that of near field. In the beginning of last century, Max Planck derived the first version of the famous Planck black-body radiation law with his quantum theory. Now we know that this law is only valid in the far field domain. It predicts that every physical object emits broadband electromagnetic radiation with amplitude depending on its temperature. The spectral radiance $B_\lambda(\lambda, \mathrm{T})$ in unit of $\mathrm{Wsr^{-1}m^{-3}}$ for an ideal blackbody can be

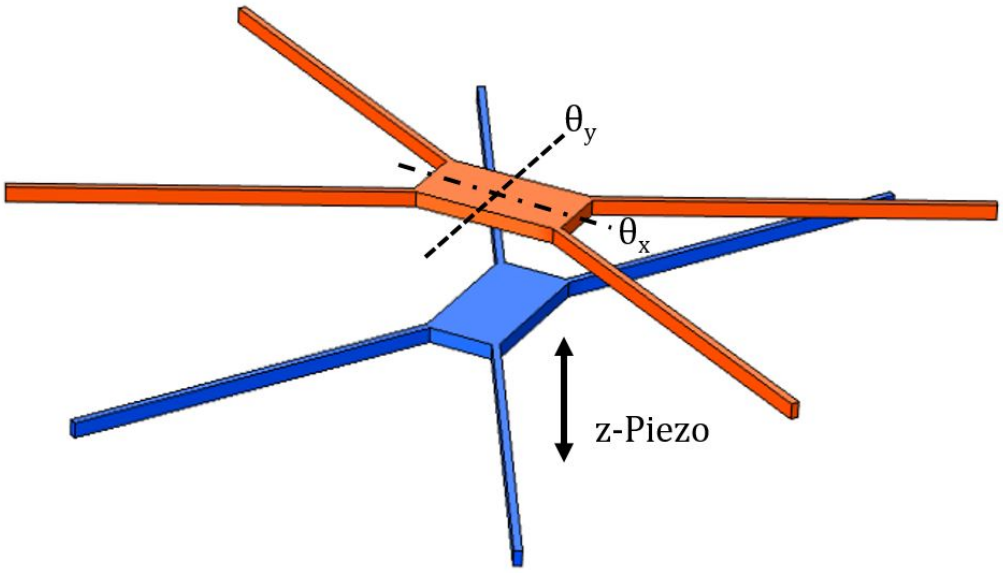


Figure 1.1: Schematic picture of the state-of-art structure for measuring the near field radiative heat transfer between emitter and receiver. The relative alignment of the emitter and receiver both in rotation and displacement is achieved by controlling a custom-built nanopositioner.

used for a detailed explanation.

$$B_\lambda(\lambda, T) = \frac{2hc^2}{\lambda^5} \frac{1}{exp(\frac{hc}{\lambda k_B T}) - 1}, \tag{1.1}$$

where $h$, $c$, and $k_B$ are the Planck constant, velocity of light, and Boltzmann constant, $\lambda$ is the wavelength, and $T$ is the temperature.

On the other hand, the spectral radiation of a real physical object depends on $B_\lambda(\lambda, T)\epsilon(\lambda)$ where $\epsilon(\lambda)$ is the object's spectral emissivity. Thus, tailing the spectral emissivity would modify the object's far field radiative property. Extensive research has been performed since Planck's time. We will only focus on two aspects, namely spectrally selective absorbers and passive radiative coolers.

Radiative heat transfer is the most fundamental means of heat transfer in our universe since there is no thermal conducting medium in between space objects for conduction and convection to occur. Take our earth, for example. It receives approximately 90 Petawatts solar energy from the sun all day round. This is about 5000 times of the global energy consumption (Abbott, 2010). Currently, photovoltaic and solar

thermal processes are being employed for solar energy harvesting. For the thermal process, there are concentrated solar power (CSP) (Mills, 2004), solar hot water system (SHWS) (Zhiqiang, 2005), solar thermophotovoltaics (STPV) (Lenert et al., 2014; N. Wang et al., 2011), and solar thermoelectric generators (STEG) (Kraemer et al., 2011). Among the four methods, CSP plants have been deployed around the world with a capacity of 5 GW, while SHWS has been widely used for domestic hot water. However, STPV and STEG are still in the stage of lab development.

CSP, SHWS, and STEG uses an absorber to harvest the solar energy and convert it into a useful form, either electricity or hot water. The schematic of a solar thermal system is shown in Figure 1.2. It consists of an absorber, a heat-to-heat or heat-to-electricity energy conversion system, and a heat sink. The absorber is responsible for receiving the solar energy. Considering that it is possible to considerably reduce the negative effect of thermal convection and conduction by using a high vacuum condition, an ideal spectrally selective absorber would have high absorption in the solar spectrum with low emissivity outside that spectrum range, mainly in mid-/far-infrared. The spectrum of an ideal absorber is shown as the red line in Figure 1.3.

During the last three decades, various spectrally selective absorbers have been explored as shown in Figure 1.4. They can be classified into six categories, namely (a) intrinsic absorbers, (b) semiconductor-metal tandem absorbers, (c) metal-dielectric multilayer absorbers, (d) metal-dielectric cermets, (e) surface textured absorbers, and (f) photonic crystal based absorbers. (Kennedy, 2002).

Intrinsic absorbers utilize their materials' intrinsic absorptive properties and are mainly found in semiconductors and transitional metals, such as tungsten, $Cu_2S$ (Lampert, 1979). However, their absorptive spectrum is far from ideal, either due to the position of the bandgap/plasmon frequency or high refractive index mismatch between the absorber and air.

For semiconductor-metal tandem absorbers, suitable semiconductor materials (such as Ge, Si and PbS) are used to absorb high energy solar radiation below their bandgap wavelength (Donnadieu and Seraphin, 1978; Okuyama et al., 1980). By placing them on top of a metal substrate, long wavelength radiation will get reflected. Typically, these semiconductor materials have a high refractive index in the absorption spectrum, creating undesired high reflection. Top anti-reflection layers are used to

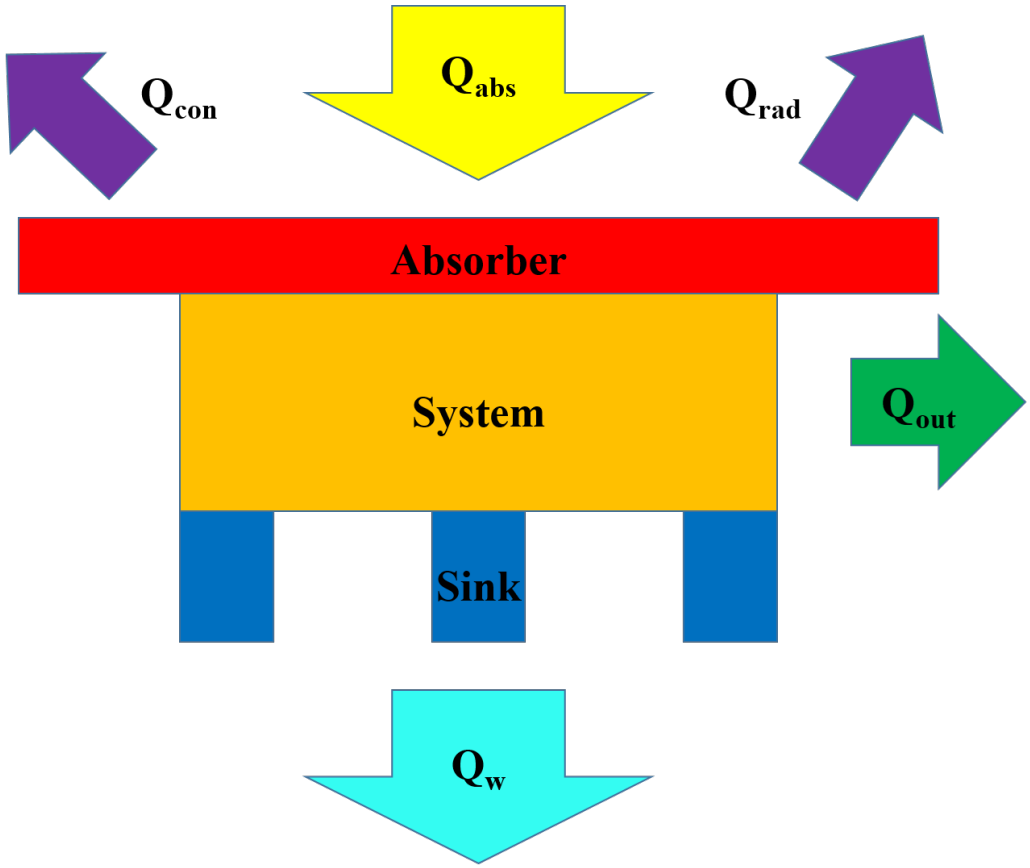


Figure 1.2: Schematic of a solar thermal system. The absorber receives $Q_{abs}$ from the sunlight while loses $Q_{con}$ and $Q_{rad}$ through conduction/convection and radiation. Typically, $Q_{con}$ can be minimized by using high vacuum system. The remaining heat is used to generate useful output power $Q_{out}$ via thermal processes such as Rankine cycle, thermoelectric generator, direct heat transfer to water, etc. Waste heat $Q_w$ is dissipated through heat sink.

suppress the reflection.

Metal-dielectric multilayer absorbers are composed of alternating metal (tungsten, silver, aluminium, etc) and dielectric layers ($SiO_2$, $TiO_2$ $Al_2O_3$) with the metal layer particularly thinner than the skin depth. These structures help to enhance some particular range of wavelengths and wide incident angles. Since there are typically over ten layers involved, numerical optimization methods are employed (X.-F. Li et al., 2007; Bermel et al., 2010). Due to the requirement of precise thickness control and multilayer structure, large-scale production remains a problem.

Metal-dielectric cermets are composites with nanoscale metal particles embedded

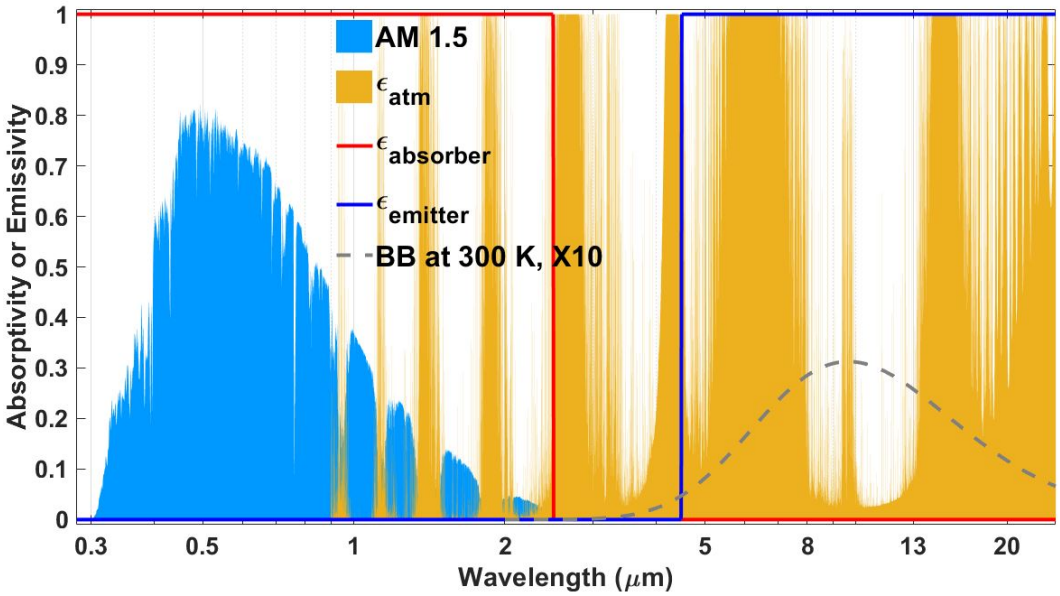


Figure 1.3: Spectrum of an ideal spectrally selective absorber (red line) and passive radiative cooler (blue line). The filled light blue area is the AM 1.5 solar spectrum while the filled orange area is the emissivity spectrum of the earth's atmosphere. The grey dashed line is the spectrum of a black body at 300 K.

in dielectric matrix. They are particularly interesting due to their good spectral performance, and flexibility, as well as their thermal stability, and are thus suitable for high temperature applications such as solar thermoelectric generators and concentrated solar power systems. Various combinations of matrix materials have been researched, including MgO, $Al_2O_3$, AlN, and $SiO_2$, with metallic particles made from high melting point metals such as Ni, Co, Ti, Mo, W, Pt, Cu, and Ag (Cao, Kraemer, et al., 2015; Barshilia et al., 2009; Sathiaraj et al., 1990; Soum-Glaude et al., 2017). Due to the same problem of impedance mismatch, anti-reflection layers are also required. These cermets can be prepared by metal electroplating, electrochemical anodization, physical and chemical vapor deposition, and solution-based fabrication methods.

To effectively increase the solar absorptivity in wide spectrum range, surface texturing can be used. It boosts the absorptivity by creating multiple reflections from the textured feature. The textured features typically range from tens of nanometers to hundreds of nanometers, providing smooth impedance transition from air to the bottom substrate for the solar spectrum while acting as a flat surface for long wave-

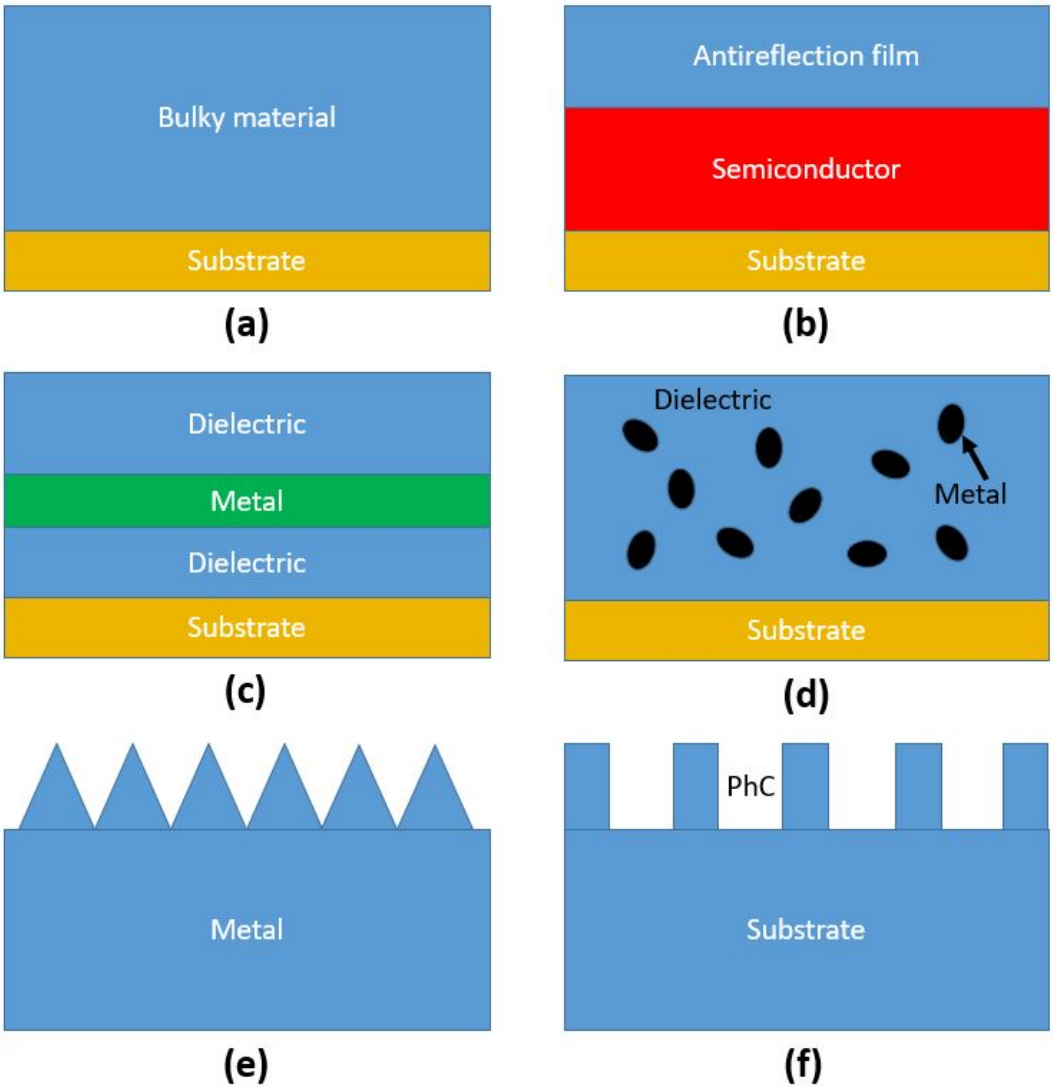


Figure 1.4: Different design of spectrally selective absorbers: (a) intrinsic absorbers, (b) semiconductor-metal tandem absorbers, (c) metal-dielectric multilayer absorbers, (d) metal-dielectric cermets, (e) surface textured absorbers, and (f) photonic crystal based absorbers.

length waves. From the experimental point of view, vapor deposition, ion-beam treatment, metal oxidation at high temperature, nanowire growth, dry etching, etc., are found to effectively create textured surfaces (Kennedy, 2002; Kussmaul, Mirtich, and Curren, 1992; J. Zhu, Z. Yu, et al., 2008). However, these nano-/micro-scale features suffers from damage upon contacting. Thus, protection layers are often required.

Photonic crystals provide a way for controlling the photon density of states and bandgap for electromagnetic waves. Photonic crystal structures with different dimensions have been explored in various material systems, for example, 1D tungsten gratings and 2D tungsten photonic crystals in square lattice by the use of a holographic mask and subsequent etching processes, 3D tungsten woodpile by modified silicon process, 3D tungsten inverse colloidal photonic crystals by self-assembly (S.-Y. Lin, Fleming, and El-Kady, 2003; S.-Y. Lin, Moreno, and Fleming, 2003; Rephaeli and Fan, 2008; Sai et al., 2003; Y.-B. Chen and ZM Zhang, 2007; Celanovic, Jovanovic, and Kassakian, 2008; Arpin et al., 2013). Due to its nanoscale feature size, nano-fabrication techniques, including lithography, nano-imprint, and self-assembly are typically used.

If we move our eyes away from the sun, we see the dark universe, which has an extremely low temperature of around 3 K. Essentially, objects on earth with ambient air temperature receive almost zero radiation power from the dark universe compared to the radiation of themselves. However, the radiation channel from objects on earth to the universe is blocked by the thick atmosphere which is spectrally opaque in a wide range, shown as the filled orange area in Figure 1.3. Fortunately, there are open windows where the atmosphere is mostly transparent, particularly the 8 to 13 $\mu$m window, corresponding to the peak of a black body radiation at 300 K (shown as the grey dashed line in Figure 1.3). Thus, nighttime radiative cooling is readily achievable as long as the emissivity in the window is high enough. In fact, nighttime radiative cooling has been known since ancient time. For example, 2000 years ago, people in Iran and India made ice through radiative cooling when the ambient air temperature is above zero degrees Celsius. In modern times, Alan Head patented the use of spectrally selective infrared radiators for nighttime use in 1959 (Head, 1959). Since then, researchers have put great effort to improve the cooling power or to get lower cooling temperature (C. Granqvist, Hjortsberg, and Eriksson, 1982; Eriksson, Lushiku, and C. Granqvist, 1984; Kimball, 1985; D. M. Diatezua et al., 1996).

However, it is much more challenging to achieve daytime radiative cooling under direct sunlight illumination with an average power density of 1 $kWm_2$, twice that of a blackbody's radiation at 300 K. Fortunately, most of the solar radiation that arrives on earth occurs at short wavelength below 2.5 $\mu$m, separated from the transparent atmospheric window as shown in Figure 1.3. Ideally, if an object has high reflectivity

in the solar spectrum and high emissivity in the transparent window as the solid blue line indicates, its radiation power could surpass the power received. In that case, its temperature could potentially drop to below ambient air temperature.

In fact, we have found daytime radiative cooling cases in nature. The Saharan silver ants use their hairs to increase the reflection of near infrared light as well as increase the mid-/far-infrared radiation, surviving in one of the hottest and driest environments on earth (Shi et al., 2015). In the early research stage of daytime radiative cooling, different investigators have proposed various schemes, such as evaporated aluminum on TEDLAR (a polyvinyl-fluoride plastic) film (Catalanotti et al., 1975), V-corrugated high-density polyethylene foils (N. Nilsson, Eriksson, and C. Granqvist, 1985), and pigmented polyethylene cover foils (T. M. Nilsson and Niklasson, 1995), optimized photonic crystal multilayer composed of SiC, quartz, $MgF_2$ and $TiO_2$ with a silver substrate (Rephaeli, A. Raman, and Fan, 2013). However, due to limitations of material synthesis, fabrication techniques, and measurement setups, requirement for high solar reflectivity and high mid-/far-infrared emissivity could not be met simultaneously. For a long time, researchers were not able to get sub-ambient temperature under direct sunlight illumination.

With the advance of new fabrication techniques, more efficient photonic structures are proposed and realized in recent years. Raman et al. first demonstrated sub-ambient temperature cooling by five degrees with dedicated material/structure selection and precise layer thickness control (A. P. Raman et al., 2014). Since then, different groups around the world have proposed or demonstrated sub-ambient cooling performance with different principles (Huang and Ruan, 2017; Zhai et al., 2017; Kecebas et al., 2017). For example, Zhai et al. manufactured in large-scale a daytime cooling structure using random-distributed micrometer-sized $SiO_2$ spheres embedded in polymer matrix and a silver back reflector (Zhai et al., 2017). Kecebas et al. demonstrated that repetitive high index-low index periodic layers could be used to replace a silver layer to get a broadband reflection with low absorption. Besides, an inserted $Al_2O_3$ film into conventional coating structures could improve radiative cooling power (Kecebas et al., 2017).

Moreover, potential applications of modified radiative coolers have also been intensively studied. For example, Zhu et al. studied how to preserve the original color of an object while achieve radiative cooling (L. Zhu, A. Raman, and Fan, 2013).

Zhu et al. also applied the cooling concept to solar cells to help improve the cells' efficiency and increase their lifetime (L. Zhu, A. Raman, K. X. Wang, et al., 2014; L. Zhu, A. P. Raman, and Fan, 2015). Hsu et al. demonstrate a dual-mode textile composed of a bilayer emitter embedded inside an infrared-transparent porous polyethylene matrix. It can be used in both passive radiative heating and cooling mode using the same piece of textile without any energy input (Hsu, C. Liu, et al., 2017; Y. Cui et al., 2019). Peng et al. fabricated porous polyethylene microfibers, and used them for indoor personal temperature regulation to get 2.3 degrees Cesius cooling performance (Peng et al., 2018). Cai et al. extended the idea to outdoor personal temperature regulation where nanocomposite textiles made from embedding zinc oxide, Prussian blue, iron oxide, and silicon nanoparticles into nanoporous polyethylene provide spectrally selective performance (Cai, A. Y. Song, et al., 2018; Cai, Peng, et al., 2019). Goldstein et al. demonstrated fluid cooling panels which combined radiative cooler to cool fluids below ambient air temperature without evaporative losses (Goldstein, A. P. Raman, and Fan, 2017).

Passive radiative coolers can be classified into the following categories: (a) foil-covered black emitter cooler, (b) multilayer photonic radiative cooler, (c) dielectric-particle-dispersed cooler, (d) double-layer nanoparticle-based cooler, and (e) Periodically structured cooler. They are schematically shown in Figure 1.5.

In a foil-covered black emitter, the top foil is responsible for absorbing or reflecting the sunlight and it is highly transparent in the atmospheric window. The foil is made of polyethylene or ethylene with reflective and absorptive pigments or dyes such as cobalt oxide, $TiO_2$, ZnS, and MgO. In addition, the foil layer is typically physically separated from the bottom emitter to avoid direct heat conduction. The bottom black emitter is responsible for mid-far-infrared radiation (T. M. Nilsson, Niklasson, and C. G. Granqvist, 1992; Silvestrini, Peraldo, and Monza, 1982).

Powerful photonic design and optimization tools are used for creating multilayer photonic radiative coolers. Multilayer interference helps to generate the desired spectrum from ultraviolet to far-infrared (M. Diatezua, Thiry, and Caudano, 1995; A. P. Raman et al., 2014; Kecebas et al., 2017; Suichi et al., 2017; J.-Y. Wu et al., 2017; Zou et al., 2017). Furthermore, armed with advanced fabrication techniques, thin layers with precise thickness control become available (A. P. Raman et al., 2014).

The dielectric-particle-dispersed cooler achieves high radiation in the mid-/far-infrared resulting from the resonant absorption of micro-sized dielectric particles embedded in transparent matrix materials (A. R. Gentle and G. B. Smith, 2010; Bao et al., 2017; Zhai et al., 2017; Hsu, C. Liu, et al., 2017). These particles are transparent in the solar spectrum. This type of cooler could be manufactured in large scale due to its simple material and fabrication requirement.

In contrary to the dielectric-particle-dispersed cooler, a double-layer nanoparticle-based cooler uses the top matrix layer to reflect the sunlight and the bottom matrix layer for thermal radiation (Bao et al., 2017; Huang and Ruan, 2017). The particles in the top layer are $TiO_2$, while the bottom layers are carbon, SiC, and $SiO_2$. In addition, this method avoids the introduction of a back reflection layer, which typically requires high vacuum deposition of metals.

Periodically structured coolers utilize their unique structures to boost the mid-/far-infrared radiation which is limited by their materials' intrinsic properties. During recent research, 2D photonic crystals and metamaterials have been proposed (Hossain, Jia, and Gu, 2015; Rephaeli, A. Raman, and Fan, 2013; L. Zhu, A. Raman, K. X. Wang, et al., 2014; L. Zhu, A. P. Raman, and Fan, 2015). 2D photonic crystals have a feature size of several micrometers and require UV lithography while metamaterials contain multilayers and are more demanding in terms of fabrication methods.

## 1.3 Thesis overview

In this thesis, we report the results obtained in tailoring thermal radiation from near field to far field.

In Chapter 2, we numerically study the near field radiative heat transfer under electrical tuning. Porous doped silicon slabs are periodically gated with an external voltage, resulting in the change of carrier concentration under different electrical stimulus, further leading to the change of relative permittivity, particularly in the infrared regime. Thus, the radiative heat transfer could be changed. With this method, we are able to modulate the heat flux by 10%.

In Chapter 3, we resolve to optical pumping of the porous doped silicon to further

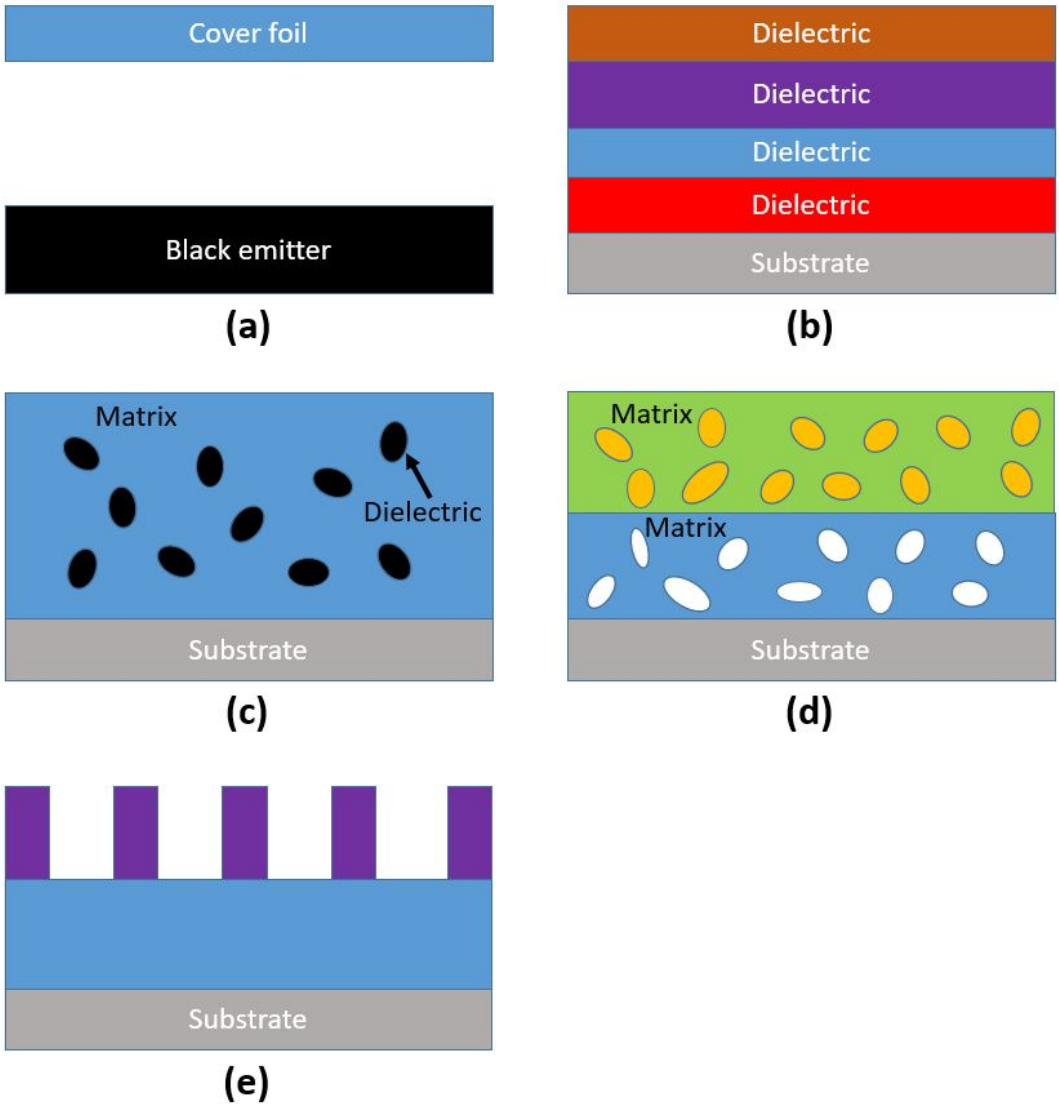


Figure 1.5: Different design of daytime passive radiative cooler: (a) foil-covered black emitter cooler, (b) multilayer photonic radiative cooler, (c) dielectric-particle-dispersed cooler, (d) double-layer nanoparticle-based cooler, and (e) periodically structured cooler.

increase the modulation contrast. By optically pumping the carriers inside the material, the heat transfer coefficient can be tuned from near zero to 600 $\mathrm{Wm^{-2}K^{-1}}$, a significant improvement.

In Chapter 4, we divert to far field where we theoretically designed and experimentally demonstrated spectrally selective absorbers based on germanium photonic crystals and black silicon. Both schemes achieve higher than 90% absorption in

the solar spectrum. Specifically, the germanium photonic crystal structure has a emissivity less than 10% in the mid-/far-infrared.

In Chapter 5, we theoretically design three schemes for realizing passive radiative cooling with direct sunlight illumination and experimentally demonstrated one of them in a field test. Results show that the simple scheme is able to achieve 8.2 °C below ambient air temperature under direct sunlight. The net cooling power at ambient temperature is calculated to be 127 $Wm^{-2}$

In Chapter 6, we conclude and give future directions in the related fields.

*Chapter 2*

# ELECTRICALLY CONTROLLED RADIATIVE TRANSFER IN THE NEAR FIELD

Active control of heat flow is of great importance in areas such as energy conversion, industrial and civil cooling/heating process, and thermal logic. Conventionally, through controlling the valves in heat transfer systems, heat flow can be achieved. Alternatively, electrostatic actuation has been employed as a thermal switch in a mechanical way (R. Ma et al., 2017). Although, difficulties exist for thermal heat flow in solid state systems without introducing moving parts, various attempts have been made. Nanotubes with external mass load yield asymmetrical axial thermal conductance (Chang et al., 2006). Nanoscale ferroelectric domain film can madulate the thermal conductivity by 11% with applied electric fields (Ihlefeld et al., 2015). Vanadium dioxide was used to construct a three-terminal temperature gated rectifier and near field radiative heat flux modulator by phase changing under different temperatures (J. Zhu, Hippalgaonkar, et al., 2014; Ito et al., 2017). However, a high contrast modulation of the heat flow with potential high speed remains elusive.

In this chapter, we focus on near field to study radiative heat transfer that is controlled via external electrical modulation of the carrier concentrations inside porous silicon. Results show that the total heat flux can be changed by 11% through external gate voltages.

## 2.1 Introduction to near field radiative heat transfer

Radiative heat transfer in the far field is governed by the Stefan-Boltzmann law which predicts that the maximum radiative heat flux J (in unit of $W/m^2$) between two identical flat plates separated by a vacuum to be $J = \epsilon\sigma(T_1^4\text{-}T_2^4)$, where $\epsilon$ is the emissivity, $\sigma$ is the Stefan-Boltzmann constant ($5.670367\times10^{-8}Wm^{-2}K^{-4}$), and $T_1$ and $T_2$ are the temperatures of the two plates under investigation.

However, the Stefan-Boltzmann law is only valid when the distance between the

two plates is much larger than the characteristic thermal wavelength which can be deduced from the Wien's displacement law according to the temperature T ($\lambda_m$ = 2898 $\mu$m K/T). As the distance approaches $\lambda_m$, near field radiation becomes significant. At the regime where the distance is much smaller than the $\lambda_m$, the near field radiation dominates the heat flux (Shen, Narayanaswamy, and G. Chen, 2009).

The theory behind the near field radiative heat transfer is described by the combination of fluctuation dissipation theorem and Maxwell's equations pioneered by Rytov and co-workers in 1950s (Rytov, 1959). According to the fluctuation dissipation theorem, the thermal emission is caused by the current from random running of charges. The fluctuating current density can be fourier transformed to $\mathbf{j}(\mathbf{x},\omega)$ in the frequency domain. This current term could be used as the excitation to solve the Maxwell's equations. With the help of dyadic Green's function $\mathbf{G}(\mathbf{x},\mathbf{x'},\omega)$, the induced electric fields could be written as the integration of Green's function multiplied by the fluctuating current density over the volume $V$.

$$\mathbf{E}(\mathbf{x},\omega) = i\omega\mu_0 \int_V \mathbf{G}^E(\mathbf{x},\mathbf{x'},\omega)\cdot\mathbf{j}(\mathbf{x'},\omega)d\mathbf{x'}. \tag{2.1}$$

Similarly, the corresponding magnetic field could be written as

$$\mathbf{H}(\mathbf{x},\omega) = \int_V \mathbf{G}^H(\mathbf{x},\mathbf{x'},\omega)\cdot\mathbf{j}(\mathbf{x'},\omega)d\mathbf{x'}, \tag{2.2}$$

where $\mu_0$ denotes the magnetic permeability of vacuum. $\mathbf{G}^E$ and $\mathbf{G}^H$ are related by each other.

$$\mathbf{G}^H(\mathbf{x},\mathbf{x'},\omega) = \nabla_{x'}\times\mathbf{G}^E(\mathbf{x},\mathbf{x'},\omega) \tag{2.3}$$

In this method, the key is to find the analytical expression of the dyadic Green's function $\mathbf{G}^E(\mathbf{x},\mathbf{x'},\omega)$ and $\mathbf{G}^H(\mathbf{x},\mathbf{x'},\omega)$, which relates the current source $\mathbf{j}$ at $\mathbf{x'}$ and electric field $\mathbf{E}$ at $\mathbf{x}$. It depends on the geometry of the materials under study. For a plannar structure, the Green function can be described as the following (Sipe, 1987):

$$\mathbf{G}^E(\mathbf{x},\mathbf{x'},\omega) = \frac{i}{8\pi^2}\int d\mathbf{K}^2\frac{1}{\gamma_2}(\hat{s}t_{21}^s\hat{s} + \hat{p}_1^+t_{21}^p\hat{p}_2^+)e^{i\mathbf{K}\cdot(\mathbf{X}-\mathbf{X'})}e^{i\gamma_1(z-d)e^{-i\gamma_2 z'}} \tag{2.4}$$

$$\mathbf{G}^H(\mathbf{x},\mathbf{x'},\omega) = -\frac{n_1\omega}{8\pi^2 c}\int d\mathbf{K}^2\frac{1}{\gamma_2}(\hat{s}t_{21}^p\hat{p}_2^+ - \hat{p}_1^+t_{21}^s\hat{s})e^{i\mathbf{K}\cdot(\mathbf{X}-\mathbf{X'})}e^{i\gamma_1(z-d)e^{-i\gamma_2 z'}}, \tag{2.5}$$

where $\mathbf{k}_i = \beta_{z,i}\hat{\mathbf{z}} + \beta_r\hat{\mathbf{r}} = \gamma_i\hat{\mathbf{z}} + K\hat{\mathbf{r}}$ and $k_i^2 = \beta_{z,i}^2 + \beta_r^2 = \gamma_i^2 + K^2$, $\hat{s} = \hat{K} \times \hat{z}$ and $\hat{p}_i^{\pm} = (K\ \hat{z} \pm \gamma_i\ \hat{K})/(n_i k_0)$. The spectral energy flux (Poynting vector) can be further derived as

$$< \mathbf{S}(\mathbf{x}, \omega) >= \frac{1}{2}\int_0^{\infty} < Re[\mathbf{E}(\mathbf{x}, \omega) \times \mathbf{H}^*(\mathbf{x}, \omega')] > d\omega', \tag{2.6}$$

where <> and $^*$ denote the ensemble averaging and complex conjugate, respectively, and $\omega$ and $\omega'$ are the angular frequencies.

The ensemble average of the spatial and spectral correlation of the fluctuating current density is expressed as

$$< j_p(\mathbf{x}, \omega) j_q(\mathbf{x'}, \omega') >= \frac{4}{\pi}\omega\epsilon_0 Im[\epsilon(\omega)]\delta_{mn}\delta(\mathbf{x} - \mathbf{x'})\Theta(\omega, T)\delta(\omega - \omega'), \tag{2.7}$$

where $j_p$ and $j_q$ (p, q = x,y,z) represent the corresponding component of $\mathbf{j}$ and $\delta_{mn}$ is the Kronecker delta function, while $\delta(\mathbf{x}\text{-}\mathbf{x'})$ and $\delta(\omega - \omega')$ are Dirac delta functions. $\Theta(\omega, T)$ is the mean energy of the Planck harmonic oscillator at temperature T.

$$\Theta(\omega, T) = \frac{\hbar\omega}{exp(\hbar\omega/k_B T) - 1}, \tag{2.8}$$

where $\hbar$ is the reduced Planck constant and $k_B$ is the Boltzmann constant.

Here, we consider the case where two semi-infinitely thick slabs with different temperature ($T_1$ and $T_2$) and relative permittivity ($\epsilon_1$ and $\epsilon_2$) separated by a vacuum gap with thickness of $d$ shown in Figure 2.1. Although the whole system is not in thermal equilibrium, each side of the slabs is assumed to be in thermal equilibrium because of the relatively large thermal conductivity of the constitutive materials. To calculate the radiative heat transfer between the two slabs, we choose the coordinate system as shown in 2.1, with $\mathbf{z}$ denoting the direction perpendicular to the interface while $\mathbf{r}$ being the in-plane direction. Correspondingly, we choose $\beta_z$ and $\beta_r$ to be the wavevector component, namely, $\mathbf{k}_i = \beta_{z,i}\hat{\mathbf{z}} + \beta_r\hat{\mathbf{r}}$ and $k_i^2 = \beta_{z,i}^2 + \beta_r^2$. Note that the wavevector parallel to the interface is conserved. The magnitude of the wavevector is obtained via $k_i = \sqrt{\epsilon}_i k_0$ with $k_0 = \omega/c$ being the wavevector in vacuum.

The net heat flux between the two slabs can be found by

$$q = \frac{1}{\pi^2}\int_0^{\infty} d\omega[\Theta(\omega, T_1) - \Theta(\omega, T_2)]\int_0^{\infty} d\beta_r[\Gamma_s(\omega, \beta_r) + \Gamma_p(\omega, \beta_r)] \tag{2.9}$$

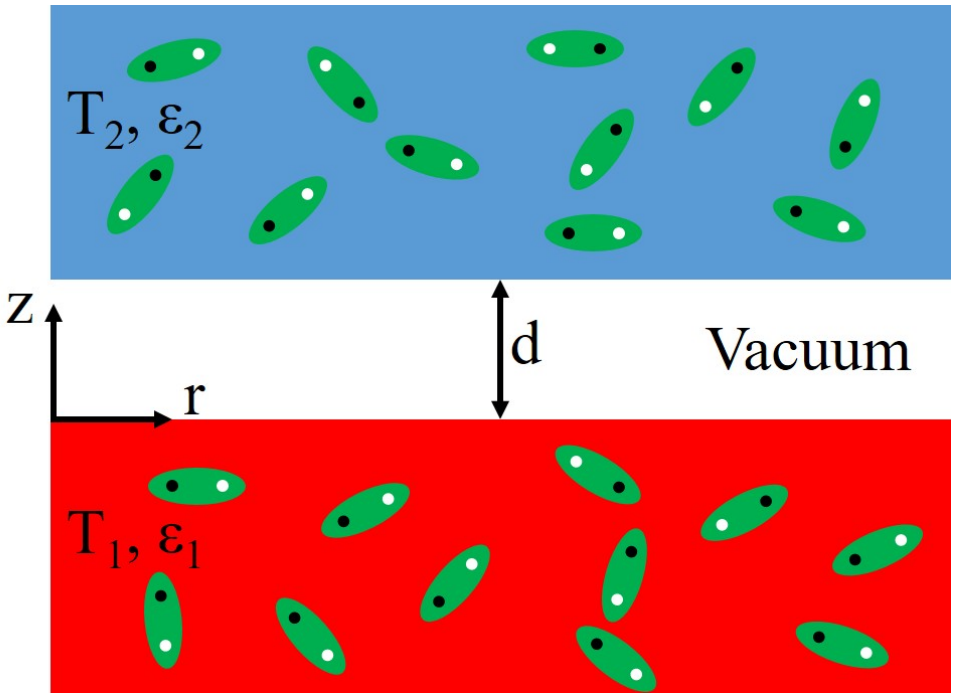


Figure 2.1: Schematic configuration of the near-field radiative heat transfer between two semi-infinitely thick slabs with different temperature and relative permittivity separated by a vacuum gap with thickness of $d$.

and the heat transfer coefficient is shown as the following:

$$h = \frac{1}{\pi^2}\int_0^\infty d\omega \frac{\partial\Theta(\omega,T)}{\partial T}\int_0^\infty d\beta_r[\Gamma_s(\omega,\beta_r)+\Gamma_p(\omega,\beta_r)], \tag{2.10}$$

where $\Theta(\omega,T)$ is the mean energy of a harmonic oscillator metioned before. The exchange function $\Gamma$ for the $s$ and $p$ modes in the second integral is expressed as

$$\Gamma_{\alpha=s,p}(\omega,\beta_r) = \begin{cases} \beta_r \dfrac{(1-|R_\alpha^1|^2)(1-|R_\alpha^2|^2)}{4|1-R_\alpha^1 R_\alpha^2 e^{i2\beta_z d}|^2}, & \text{for } \beta_r < \omega/\mathrm{c}; \\ \beta_r \dfrac{Im[R_\alpha^1]Im[R_\alpha^2]e^{i2\beta_z d}}{|1-R_\alpha^1 R_\alpha^2 e^{i2\beta_z d}|^2}, & \text{for } \beta_r > \omega/\mathrm{c}. \end{cases} \tag{2.11}$$

Here, $R_\alpha^i$ is the reflection coefficient of the multilayer system as seen from inside the vacuum gap, where i denotes the domain with i = 1, 2 and $\alpha$ denotes the polarization. If the constitutive materials of the slabs are assumed to be same and the difference of electromagnetic properties with temperature is neglected, we obtain $R_\alpha^1 = R_\alpha^2$.

The contribution of both propagating ($\beta_r < \omega/c$) and evanescent waves ($\beta_r > \omega/c$) to the radiative transfer is included.

## 2.2 Optical properties of silicon

The relative permittivity of doped silicon ($\epsilon_m$) in the infrared can be described by the Drude model where carriers are assumed to travel freely inside the materials.

$$\epsilon_m = \epsilon_\infty - \omega_p^2/(\omega^2 + i\gamma\omega), \tag{2.12}$$

where $\epsilon_\infty$ is the permittivity at high frequency limit, $\omega$ is the angular frequency of interest while $\omega_p$ is the plasma frequency that is related to the carrier concentration which can be tuned via external stimulation, $\gamma$ is the damping rate. The detailed relation between plasma frequency and carrier concentration could be found in Ref. (S Basu, B. J. Lee, and ZM Zhang, 2010). Here, we plot the relative permittivity of bulk doped silicon with different carrier concentrations in Figure 2.2. It can be easily identified that the real part of the permittivity is negative and its magnitude is much larger than 1.

## 2.3 Effective medium theory

The effective permittivity of the porous silicon films is obtained using the Maxwell-Garnett equation (Garnett, 1905):

$$\epsilon_{eff} = \epsilon_m \frac{2f(\epsilon_i - \epsilon_m) + \epsilon_i + 2\epsilon_m}{2\epsilon_m + \epsilon_i + f(\epsilon_m - \epsilon_i)}, \tag{2.13}$$

where $\epsilon_m$ is the relative permittivity of the matrix medium (doped silicon assumed here) and $\epsilon_i$ is the relative permittivity of the inclusions (for vacuum, $\epsilon_i = \epsilon_3 = 1$), and $f$ is the porosity or the volume fraction of the inclusions.

Figure 2.3 is the results of the relative permittivity of porous silicon with different porosities at a carrier concentrations of $10^{19}$ cm$^{-3}$. We can clearly observe that the real part of the permittivity is greatly improved compared to bulk value. We should

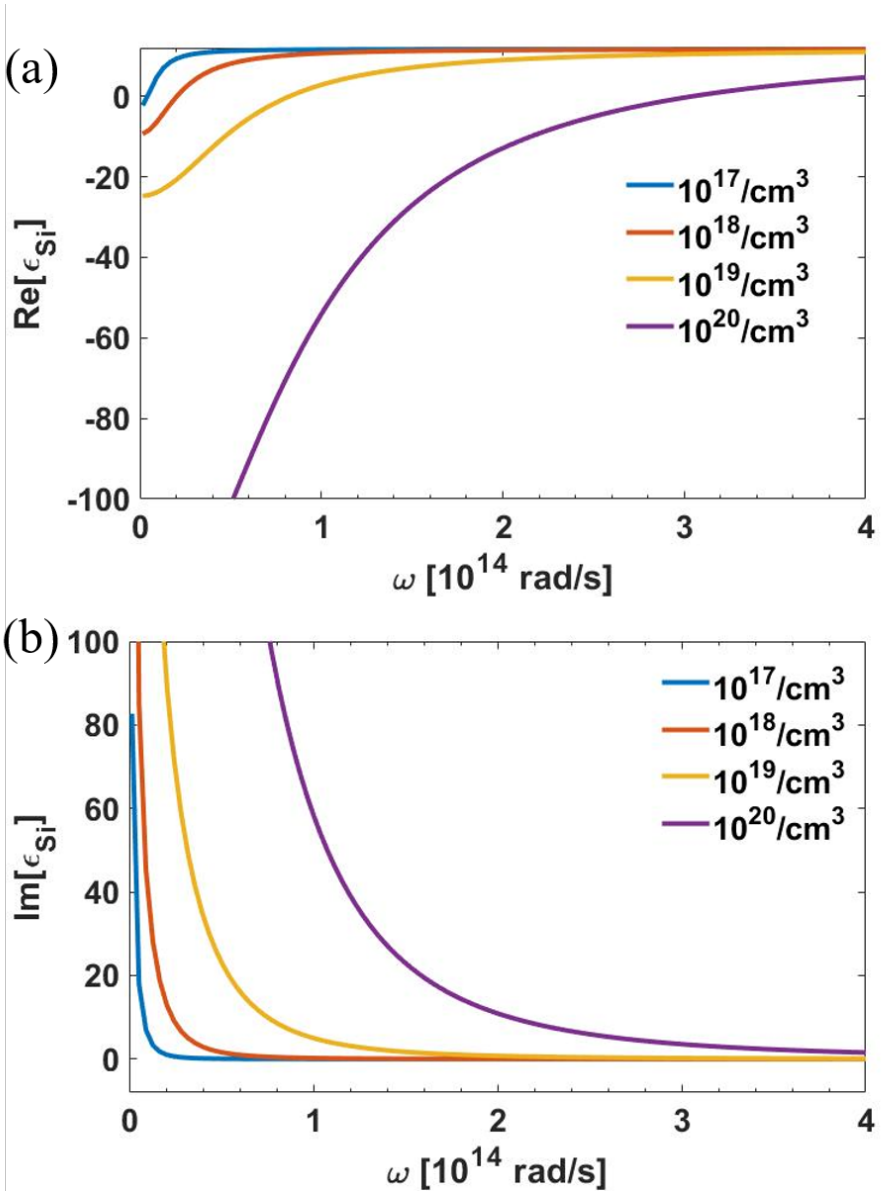


Figure 2.2: The (a) real and (b) imaginary part of the relative permittivity of bulk silicon with different carrier concentrations in the infrared frequency.

also note that porous silicon has been experimentally realized for gradient refractive index devices (Krueger et al., 2016) and distributed Bragg reflectors (Ocier et al., 2017) in the visible regime.

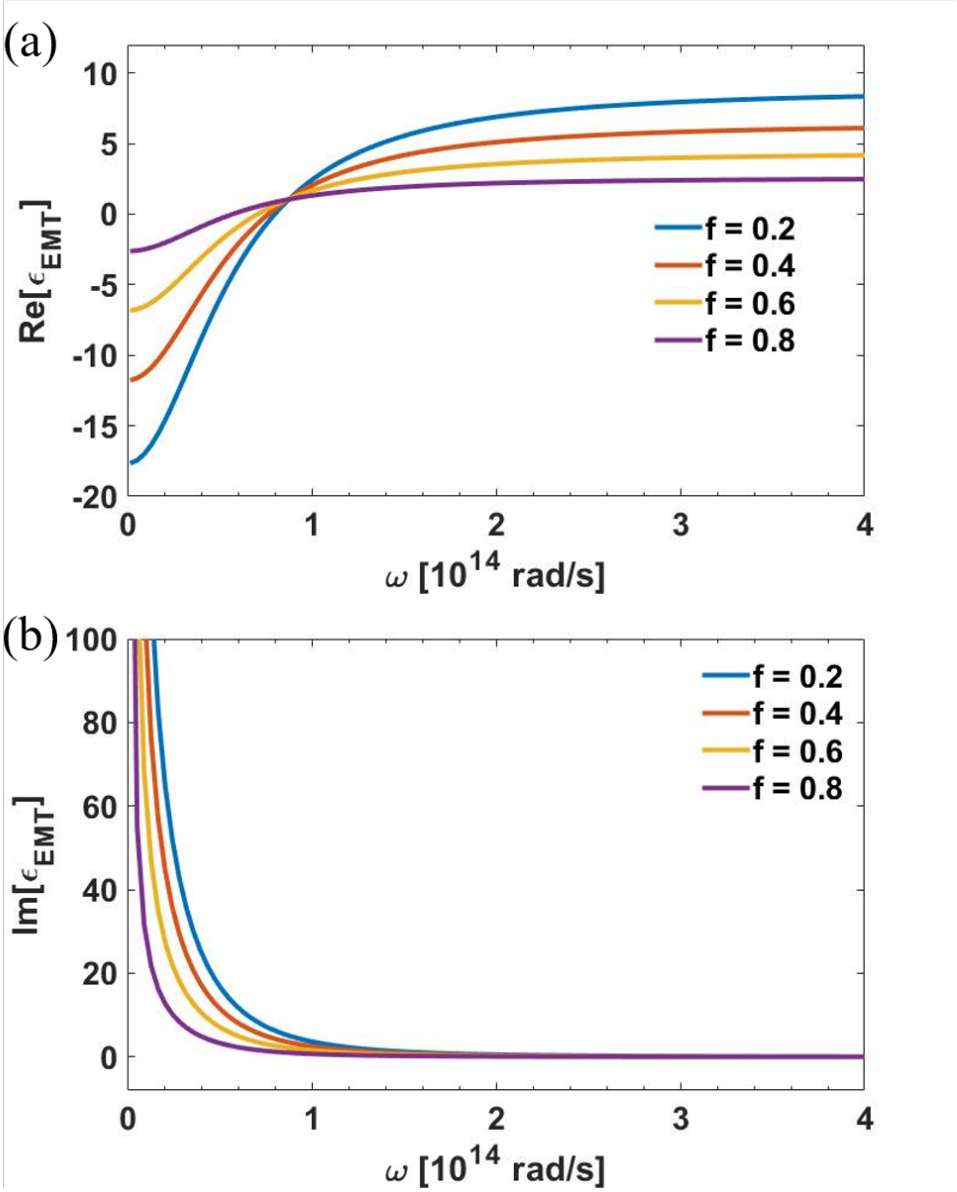


Figure 2.3: The (a) real and (b) imaginary part of the relative permittivity of porous silicon with different porosity in the infrared frequency at a carrier concentrations of $10^{19}$ $cm^{-3}$.

## 2.4 Recombination mechanism in silicon

A Shockley-Read-Hall (SRH) model is used for the trap-assisted recombination with effective SRH rate as follows (Chuang, 2012):

$$R_{SRH} = \frac{np - n_i^2}{\tau_p(n + n_i) + \tau_n(p + n_i)} \tag{2.14}$$

$$n_i = \sqrt{N_c N_v} exp(-\frac{E_g}{2k_B T}), \tag{2.15}$$

where $n$ and $p$ are the concentration of electrons and holes, respectively, and $n_i$ is the intrinsic concentration. $N_c$ and $N_v$ are the effective density of states in the conduction and valence band. $E_g$ is the bandgap. The electron and hole lifetime parameters are assumed to be $\tau_n = \tau_p = 10$ $\mu$s.

In later section and chapter, we use porous silicon as the work horse for near field radiative heat transfer. Due to the large surface area involved in porous materials, special care should be taken on surfaces. Here, surface recombination is included with parameters from Ref. (Yablonovitch et al., 1986).

$$R_{Surface} = S(p - p_0) \tag{2.16}$$

with $S$ being the surface recombination velocity, $p_0$ being the initial concentration of holes, and $A_s$ being the surface area.

Auger recombination should also be included, especially when the carrier concentration is large since the recombination rate depends on the third order of carrier concentration.

$$R_{Auger} = (C_n n + C_p p)(np - n_i^2), \tag{2.17}$$

where $C_n = C_p = 2{\times}10^{-32}$ cm$^6$s$^{-1}$ is the Auger recombination factor of electrons and holes (Huldt, 1971).

## 2.5 Results and discussion of electrically controlled near field radiative heat transfer

Figure 2.4 shows the schematic of the proposed structure under study. Two doped silicon slabs with thickness of 50 nm are placed in close proximity with a gap

distance of 100 nm. The porous silicon is chosen to be doped with a concentration of $2\times10^{17}$ cm$^{-3}$ (purple color in figure). The electrodes are separated by 200 nm with an electrode width of 80 nm. One set of the electrodes (the red color) is assumed to be separated from the silicon slab by a thin layer of oxide, working as the gate electrodes. These values are chosen based on the following considerations. The breakdown electric field of silicon is $3\times10^5$ V/cm for a n-type doping level of $2\times10^{17}$ cm$^{-3}$ (Sze and Ng, 2006). Thus, the maximum width of the depletion region is limited to 65 nm (Sze and Ng, 2006), meaning that we are not able to significantly change the carrier concentration with a distance over 65 nm. Higher doping levels lead to narrower widths of the depletion region. Another estimation could be performed about the maximum voltage applied on the electrodes $V_{max} \approx$ 100 nm $\times$ $3\times10^5$ V/cm = 3 V.

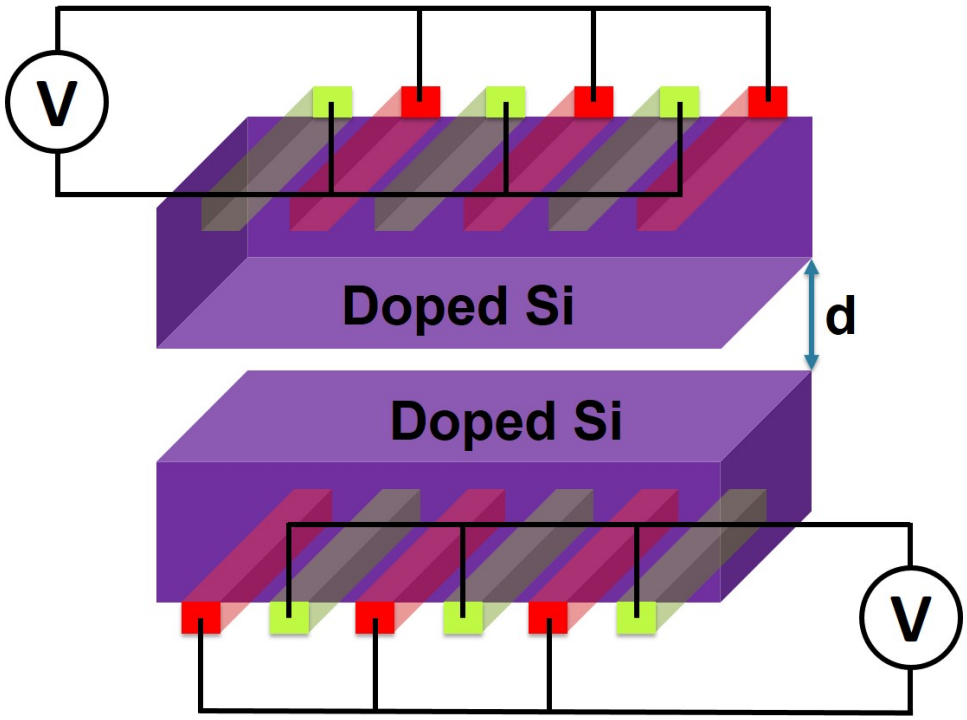


Figure 2.4: Schematic configuration of the near-field radiative heat transfer via external electrical tuning. Two doped silicon slabs with thickness of 50 nm are separated by a distance $d$ = 100 nm. On the back side of each slab, interdigitated electrodes are used to deplete carriers in certain areas. Note that there is an oxide layer between the red electrodes (gate) and the silicon slabs and this is not drawn in the figure.

We first set out to get the carrier concentration distribution of the proposed structure.

Figure 2.5 is the electron (first row in each figure) and hole (second row in each figure) distribution of the silicon slab under different external gate voltage. At zero voltage, the electron has a concentration of $2\times10^{17}$ $cm^{-3}$ while the concentration of holes can be neglected considering its effect on relative permittivity. With the decreasing gate voltage, the electrons will be depleted. The concentration of electrons could be tuned from its intrinsic doping level of $2\times10^{17}$ $cm^{-3}$ (completely ionized at this level) to an average of $1\times10^{16}$ $cm^{-3}$ by changing the external gate voltage from 0 to -1.74 V. With the change of carrier concentrations, we expect the relative permittivity of the slab to change accordingly as discussed above. We set out to calculate the near field radiative heat flux change.

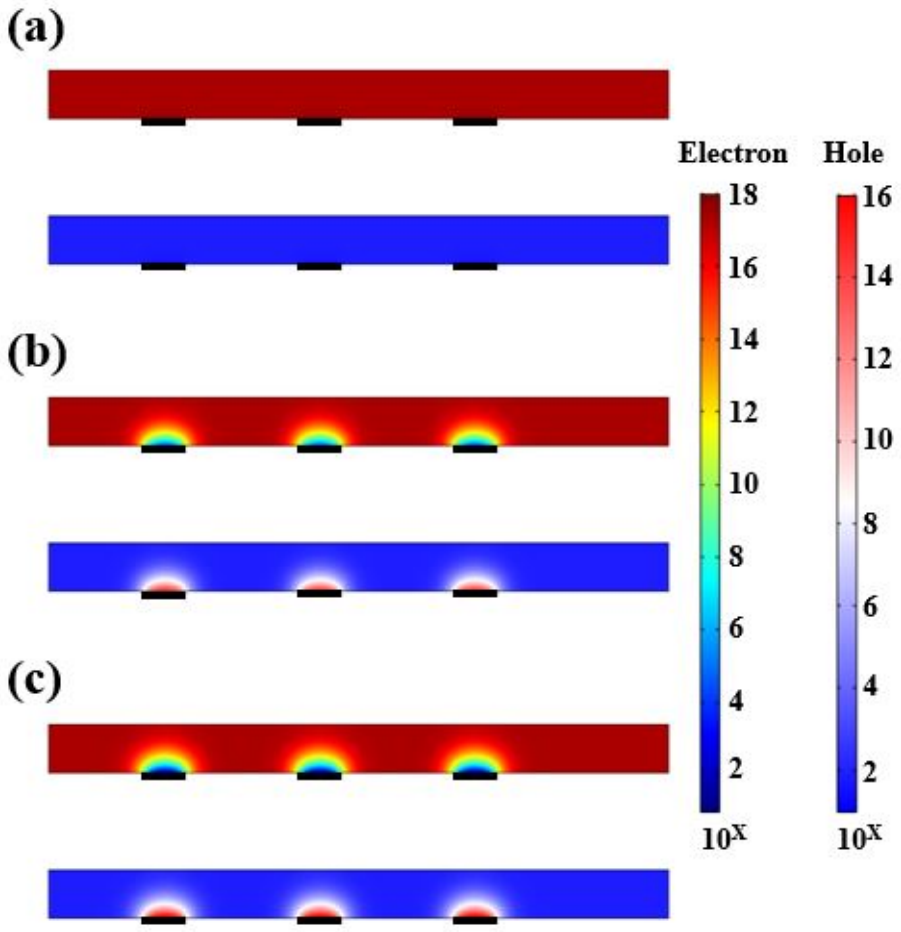


Figure 2.5: Electron (first row in each figure) and hole (second row in each figure) concentration under external gate voltage at (a) 0, (b) -1.5, (c) -1.74 V. The black bars under the slabs denote the gate electrodes. The silicon slabs have background n-type doping of $2\times10^{17}$ $cm^{-3}$.

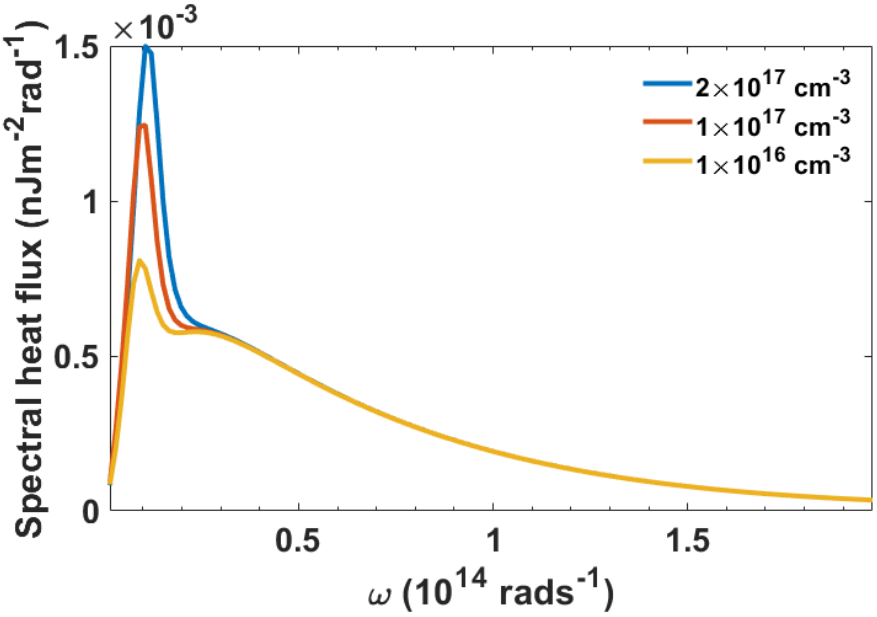


Figure 2.6: Spectral heat flux as a function of angular frequency with different carrier concentrations tuned by external gate voltage.

Figure 2.6 is the result of the calculated spectral heat flux. The magnitude changes dramatically in the low frequency range where the plasmonic effect is the strongest. The total heat flux is calculated to be 56.9 $Wcm^{-2}$ at 0 V and 50.6 $Wcm^{-2}$ at -1.74 V, 11% change in modulation.

## 2.6 Conclusions

We have described the physical mechanism of near field radiative heat transfer and proposed a method for controlling the near field radiative heat transfer via external electrical tuning. By changing the gate voltage from 0 V to -1.74 V, the total heat flux can be changed by 11%.

*Chapter 3*

# DYNAMIC OPTICAL CONTROL OF NEAR-FIELD RADIATIVE TRANSFER

Part of this chapter has been adapted from:

Kou, Junlong and Austin J Minnich (2018). "Dynamic optical control of near-field radiative transfer". In: *Optics Express* 26.18, A729–A736. DOI: 10.1364/OE.26.00A729.

Dynamic control of radiative heat transfer is of fundamental interest as well as for applications in thermal management and energy conversion. However, realizing high contrast control of heat flow without moving parts and with high temporal frequencies remains a challenge. Here, we propose a thermal modulation scheme based on optical pumping of semiconductors in near-field radiative contact. External photo-excitation of the semiconductor emitters leads to increases in the free carrier concentration that in turn alters the plasma frequency, resulting in modulation of near-field thermal radiation. The temporal frequency of the modulation can reach hundreds of kHz limited only by the recombination lifetime, greatly exceeding the bandwidth of methods based on temperature modulation. Calculations based on fluctuational electrodynamics show that the heat transfer coefficient between two silicon films can be tuned from near zero to 600 $\mathrm{Wm^{-2}K^{-1}}$ with a gap distance of 100 nm at room temperature.

## 3.1 Introduction

Active control of heat flow has long been of interest in various fields (Inoue, De Zoysa, et al., 2014; Otey, W. T. Lau, and Fan, 2010; J. Zhu, Hippalgaonkar, et al., 2014; K. Chen, Santhanam, Sandhu, et al., 2015; Ding, T. Kim, and Minnich, 2016; Xinyu Liu and Padilla, 2017; Ito et al., 2017; Kats et al., 2013; Brar et al., 2015; Ihlefeld et al., 2015; Ilic, Thomas, et al., 2018; Ilic, Jablan, et al., 2012; Zheng et al., 2011). The possibility to modulate radiative transfer is especially interesting

due to its noncontact nature. The simplest mechanism to actively control radiative transfer by modulating the temperature of the emitter is limited to relatively low frequencies (Hildenbrand et al., 2010). More quantitatively, consider the use of an optical beam to modulate the temperature of a radiative emitter. Assuming the light is absorbed near the sample surface, the amplitude of the temperature change of the film is given by $\Delta T = Q_0/\sqrt{\kappa C \omega}$, where $Q_0$ is the input power density, $\kappa$ is the thermal conductivity, $C$ is the volumetric heat capacity, and $\omega$ is the external modulation angular frequency (Carslaw and Jaeger, 1959). Let us take the input power density $Q_0 = 10^2$ $\mathrm{Wcm^{-2}}$, $\kappa = 1$ $\mathrm{Wm^{-1}K^{-1}}$, $C = 10^6$ $\mathrm{Jm^{-3}K^{-1}}$ and $\omega = 2\pi\times10^5$ rad/s. The amplitude of the temperature oscillation of the films is only about 1.3 K, corresponding to a small heat transfer modulation of $8.0\times10^{-4}$ $\mathrm{Wcm^{-2}}$ despite the large input power density. Thus simply modulating the temperature of a radiative emitter does not result in substantial radiative flux modulation as frequency increases.

Prior works aimed to overcome this limitation by, for example, altering emissivity with temperature-dependent phase-change materials (Kats et al., 2013; Ito et al., 2017), carrier-injection-induced modification of band structure in quantum wells (Inoue, De Zoysa, et al., 2014), and electrostatic gating of graphene plasmonic resonators (Brar et al., 2015), among other schemes. However, these schemes modulated the far-field radiation, which significantly limits the maximum heat flux. Further, the broadband nature of thermal radiation imposes stringent requirements on any method as a wide spectrum of electromagnetic waves must be manipulated.

On the other hand, near-field radiative transfer is capable of supporting heat fluxes that are orders of magnitude larger than that in the far-field (Shen, Narayanaswamy, and G. Chen, 2009; Rousseau et al., 2009; B. Song, Thompson, et al., 2016; Y. Yang and L. Wang, 2016; St-Gelais et al., 2016) through a relatively narrow bandwidth (Shchegrov et al., 2000). These properties have been exploited in various applications, including thermophotovoltaics (Karalis and Joannopoulos, 2016; Laroche, Carminati, and Greffet, 2006; Messina and Ben-Abdallah, 2013; Zhao et al., 2017), solid-state cooling (K. Chen, Santhanam, Sandhu, et al., 2015), thermal rectification (Otey, W. T. Lau, and Fan, 2010; Soumyadipta Basu and Francoeur, 2011), and active extraction of bound surface waves (Ding, T. Kim, and Minnich, 2016), among others. A method that is capable of dynamically modulating near-field radiative heat transfer would be of great interest. As doped semiconductors possess surface

resonance frequencies in the infrared that vary with carrier concentration (S Basu, B. Lee, and ZM Zhang, 2010), actively altering carrier concentration could provide a mechanism to modulate radiative transfer. However, although optical pumping has been used for tuning the permittivity of different materials via carrier photoinjection with high speed (Dunkelberger et al., 2018; Guo et al., 2016; Kinsey et al., 2015), the effects on radiative transfer have not yet been studied.

Here, we propose a scheme for dynamically controlling near-field radiative transfer between semiconductors by external optical illumination with hundreds of kHz. A change of carrier concentration induced by the optical pumping shifts the plasma frequency of the semiconductor, altering the near-field radiative heat transfer coefficient. Our results show that heat transfer coefficient can be tuned from near zero to 600 $\mathrm{Wm^{-2}K^{-1}}$ at room temperature with a bandwidth on the order of hundreds of kHz. Our work introduces a promising method to realize dynamic external control of heat flow.

## 3.2 Theory

The system we consider is shown in Figure 3.1. Two parallel porous silicon films (denoted as Region 1 and 2) are put in close proximity to each other with a vacuum gap distance $d$ (denoted as Region 3). The two films are supported by two substrates in contact with separate thermal reservoirs. We choose porous silicon rather than fully dense silicon to enable the formation of surface plasmon polaritons (SPPs) with high near-field energy density as discussed in the next section. Optical elements composed of porous silicon have been fabricated for gradient refractive index devices (Krueger et al., 2016) and distributed Bragg reflectors (Ocier et al., 2017) in the visible regime. These two films are optically pumped by two laser beams with wavelength 400 nm corresponding to an absorption coefficient of $1.06\times10^5$ $\mathrm{cm^{-1}}$. Although the absorption depth is around 100 nm, smaller than the thickness of the films (1 $\mu$m), the fast carrier diffusion process on the order of 1 ns leads to a nearly uniform free carrier concentration in the film during modulation with period over 1 $\mu$s. The background doping concentration is taken to be $10^{15}$ $\mathrm{cm^{-3}}$. We assume that the steady power of the lasers and the temperatures of the thermal reservoirs are chosen so that each film is at a specified temperature. For the purpose of calculating

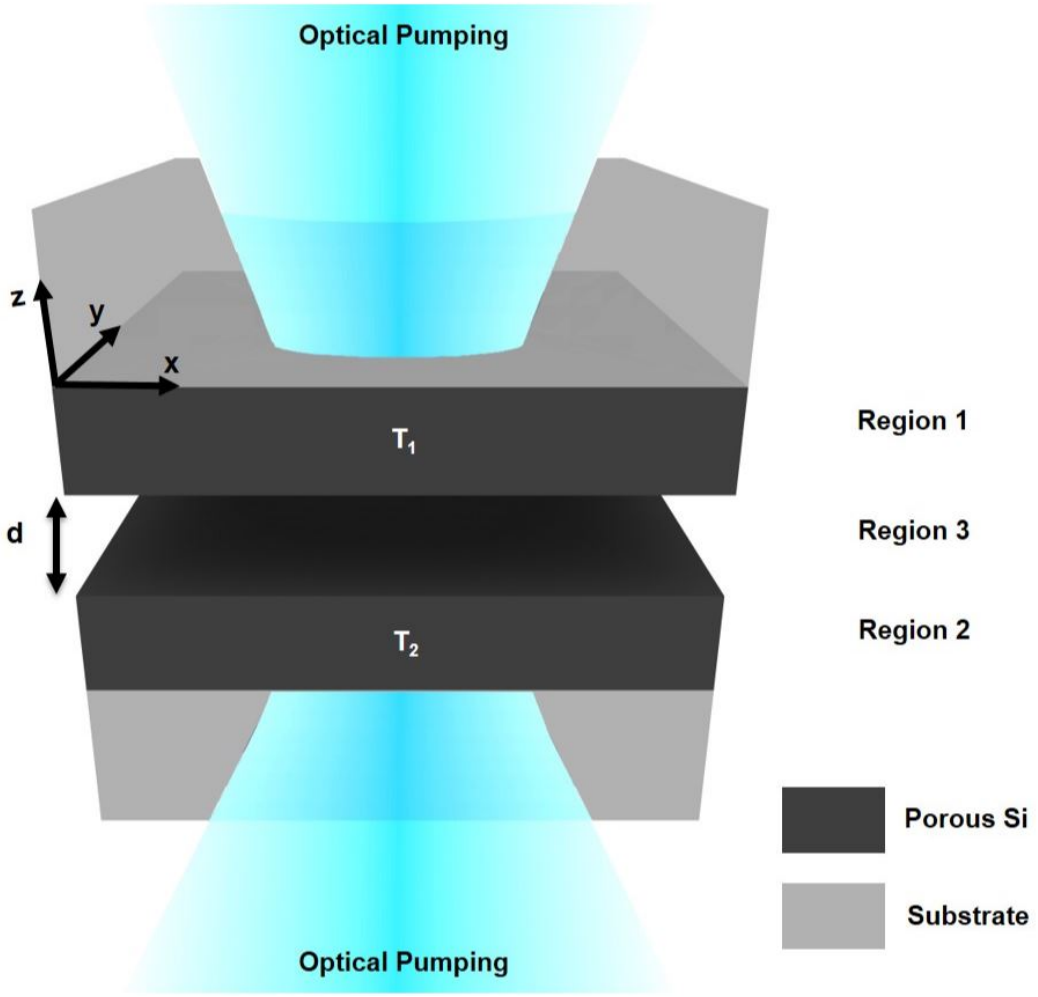


Figure 3.1: Schematic of the configuration for near-field radiative transfer dynamically controlled by external optical excitation. The two porous semiconductor films of thickness $t$ on two substrates are maintained at constant temperature of $T_1$ and $T_2$ ($T_1 > T_2$) with a vacuum gap distance of $d$. Free carriers are excited by the external illumination from both sides, leading to the formation of surface plasmons and resulting in a modulation of near-field radiative heat transfer.

the heat transfer coefficient, the temperatures of the two films are taken to be $T_1$ = 300 K and $T_2$ = 299 K, but in an actual application the temperature difference could be much larger. Under external optical pumping, excited free carriers result in the change of its relative permittivity, leading to an increase of near-field radiative heat transfer. Moreover, when the pumping is off, carriers recombine and the radiative heat transfer decreases to near zero, providing a mechanism to rapidly modulate near-field radiative transfer.

We calculate the near-field radiative heat transfer coefficient for this scheme using the standard formalism of fluctuational electrodynamics (Rytov, 1959). The heat transfer coefficient ($h$) is given as

$$h = \frac{1}{\pi^2}\int_0^\infty d\omega \frac{\partial\Theta(\omega,T)}{\partial T}\int_0^\infty d\beta[\Gamma_s(\omega,\beta)+\Gamma_p(\omega,\beta)], \tag{3.1}$$

where $\Theta(\omega,T) = \hbar\omega/[\exp(\hbar\omega/k_BT)-1]$ is the mean energy of a harmonic oscillator, $\hbar$ is the reduced Planck constant, $k_B$ is the Boltzmann constant, $\beta$ is the wave vector in the x-y plane, and $T$ is the absolute temperature. The exchange function $\Gamma$ for the $s$ and $p$ modes in the second integral is expressed as

$$\Gamma_{\alpha=s,p}(\omega,\beta) = \begin{cases} \beta\dfrac{(1-|R_\alpha^1|^2)(1-|R_\alpha^2|^2)}{4|1-R_\alpha^1R_\alpha^2e^{i2\beta_z d}|^2}, & \text{for } \beta < \omega/\text{c}; \\ \beta\dfrac{Im[R_\alpha^1]Im[R_\alpha^2]e^{i2\beta_z d}}{|1-R_\alpha^1R_\alpha^2e^{i2\beta_z d}|^2}, & \text{for } \beta > \omega/\text{c}. \end{cases} \tag{3.2}$$

Here, $R_\alpha^i$ is the reflection coefficient of the multilayer system as seen from inside the vacuum gap, where i denotes the domain with i = 1, 2 and $\alpha$ denotes the polarization. We neglect the difference of electromagnetic properties with temperature, leading to $R_\alpha^1 = R_\alpha^2$. $\beta_z$ is the wave vector along the z-direction inside vacuum. The contribution of both propagating ($\beta < \omega/c$) and evanescent waves ($\beta > \omega/c$) to the radiative transfer are included.

The effective permittivity of the porous silicon films is obtained using the Maxwell-Garnett equation (Garnett, 1905):

$$\epsilon_1 = \epsilon_2 = \epsilon_{eff} = \epsilon_m\frac{2f(\epsilon_i-\epsilon_m)+\epsilon_i+2\epsilon_m}{2\epsilon_m+\epsilon_i+f(\epsilon_m-\epsilon_i)}, \tag{3.3}$$

where $\epsilon_m = \epsilon_\infty - \omega_p^2/(\omega^2+i\gamma\omega)$ is the relative permittivity of the matrix medium (silicon) (S Basu, B. Lee, and ZM Zhang, 2010) and $\epsilon_i$ is the relative permittivity of the inclusions (vacuum, $\epsilon_i = \epsilon_3 = 1$), and $f$ is the porosity or the volume fraction of the inclusions. The plasma frequency ($\omega_p$) is directly related to the carrier concentration which is controlled by the external illumination intensity. The effect of illumination is thus modeled simply as an altered permittivity of the porous silicon matrix.

The external optical power needed to create a steady state concentration of photoexcited carriers depends on the relevant carrier recombination mechanisms of silicon.

A Shockley-Read-Hall (SRH) model is used for the trap-assisted recombination which is described in last chapter and is adopted here again considering the volume ($V$). The electron and hole lifetime parameters are assumed to be $\tau_n = \tau_p = 10$ $\mu$s with a trap density of $5{\times}10^{13}\text{cm}^{-3}$ (Sze and Ng, 2006).

$$R_{SRH} = \frac{np - n_i^2}{\tau_p(n + n_i) + \tau_n(p + n_i)}V \tag{3.4}$$

with $n$ and $p$ being the concentrations of electrons and holes, $n_i$ being the intrinsic carrier concentration and $V$ being the volume of the solid portion of the porous medium. Auger recombination is also included as the following by considering the volume ($V$):

$$R_{Auger} = (C_n n + C_p p)(np - n_i^2)V, \tag{3.5}$$

where the factor $C_n = C_p = 2{\times}10^{-32}$ $\text{cm}^6\text{s}^{-1}$ (Huldt, 1971).

Surface recombination is included considering the total surface:

$$R_{Surface} = S(p - p_0)A_s \tag{3.6}$$

with $S$ being the surface recombination velocity, $p_0$ being the initial concentration of holes and $A_s$ being the surface area. The surface recombination velocity is obtained from Ref. (Yablonovitch et al., 1986). To account for the large surface area of porous materials, we assume that the pores are spheres with radius $r$ arranged in period of $a$ with porosity $f = 4\pi r^3/3a^3$ which leads to a large surface to volume ratio $A_s/V = 4\pi r^2/a^3$. Although the large surface area leads to appreciable surface recombination, we note that even if the surface recombination velocity is an order of magnitude larger than the value chosen here, the required optical power to achieve a given modulation only increases by a factor of two due to the influence of Auger recombination. Therefore, our scheme is still applicable even for less ideal surfaces.

## 3.3 Results

We first examine the heat transfer coefficient versus porosity for a specific carrier concentration of $10^{19}$ $\text{cm}^{-3}$ in Figure 3.2(a). For these calculations, the carrier

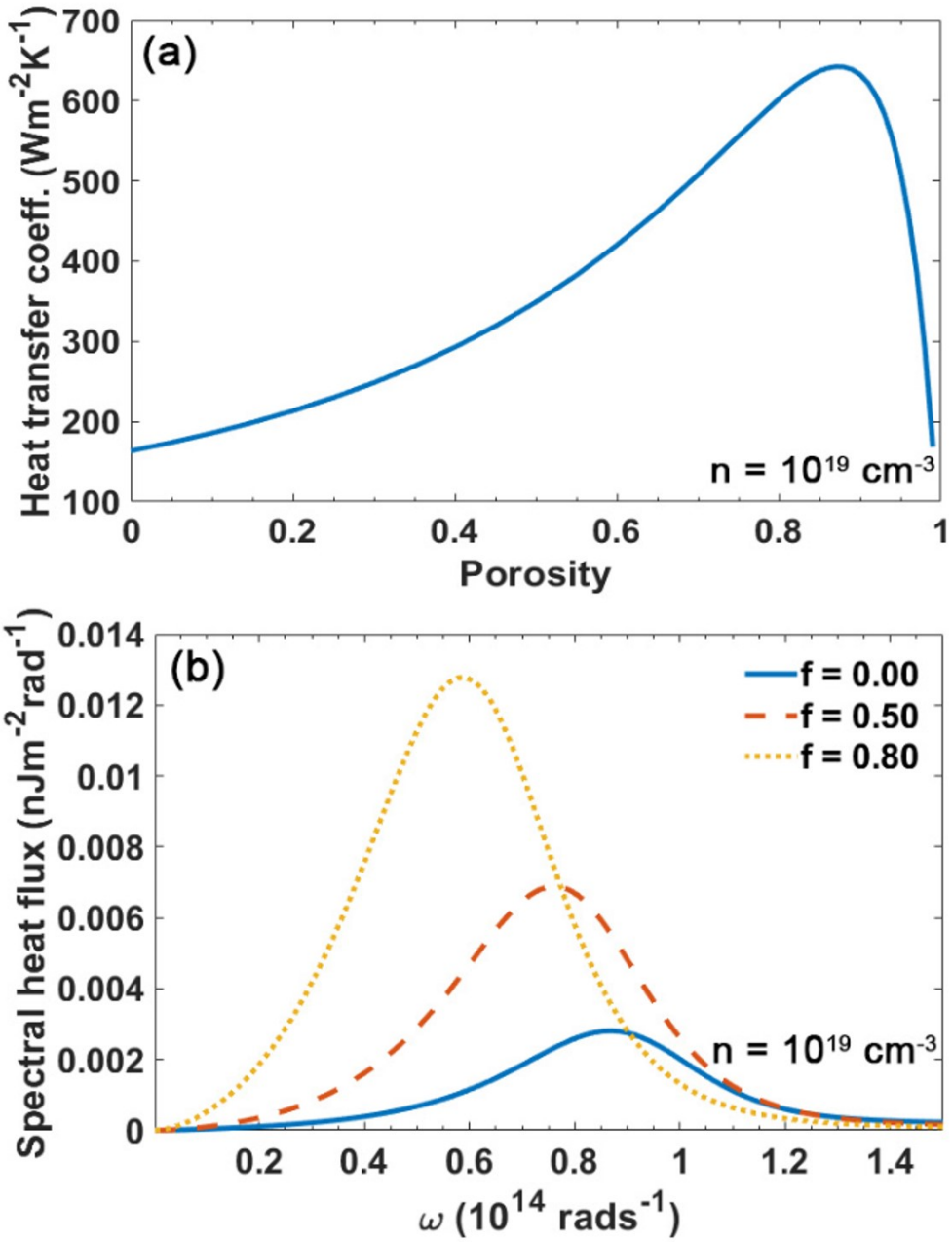


Figure 3.2: (a) Heat transfer coefficient versus porosity. (b) Spectral heat flux versus frequency for different porosities. Both calculations are performed with a carrier concentration of $10^{19}$ cm$^{-3}$

.

concentration and film thickness are chosen to be $10^{19}$ cm$^{-3}$ and 1 $\mu$m, respectively. The maximum heat transfer coefficient of 640 Wm$^{-2}$K$^{-1}$ is achieved at $f = 0.87$.

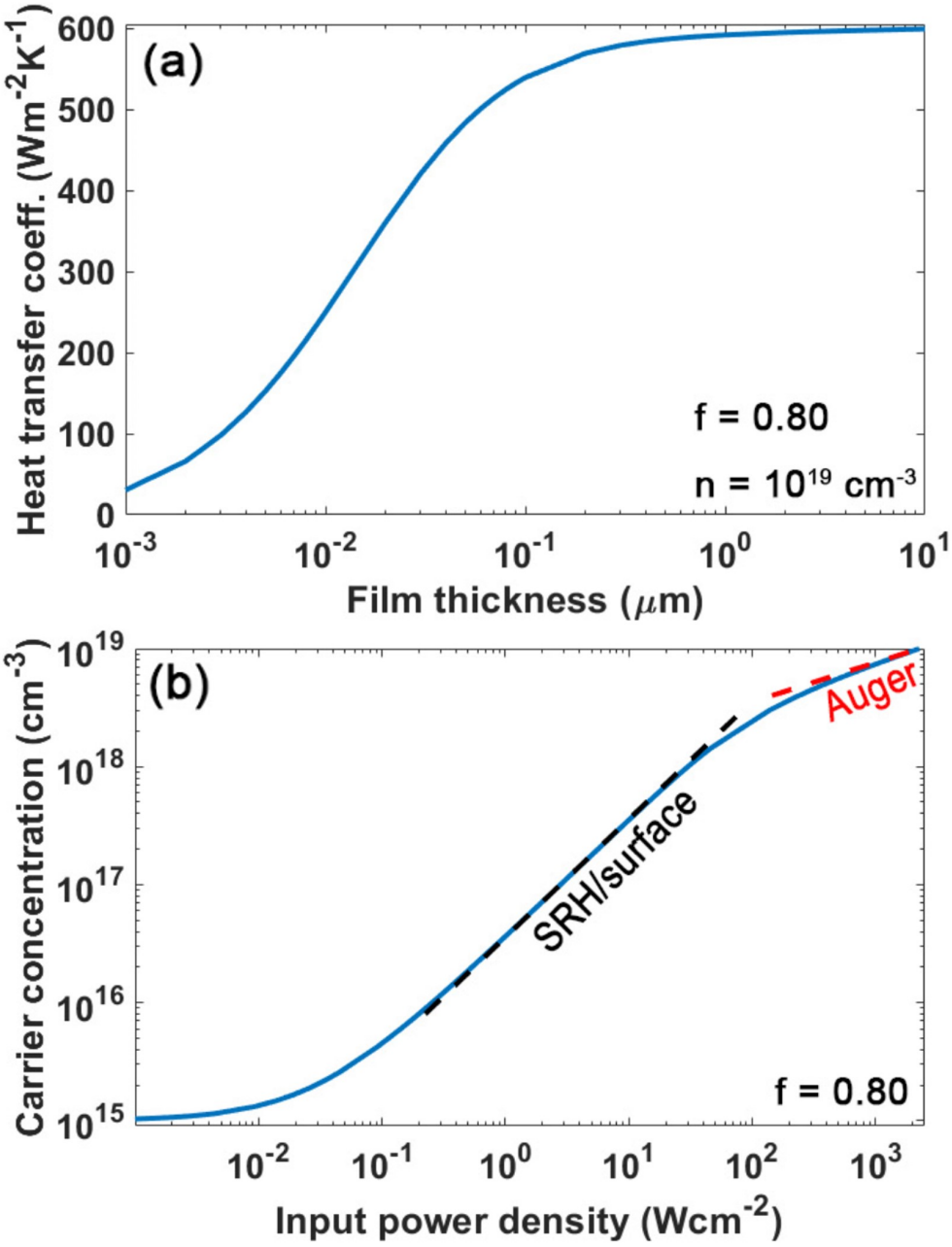


Figure 3.3: (a) Heat transfer coefficient versus film thickness at $f = 0.80$. The heat transfer coefficient remains almost constant beyond 1 $\mu$m. (b) Carrier concentration versus input power density. The black and red dashed lines are the asymptotes considering only trap-assisted/surface recombination mechanism and Auger recombination mechanisms, respectively. Both calculations are performed with a carrier concentration of $10^{19}$ cm$^{-3}$

.

Previously, porous silicon with porosity of 0.85 has been experimentally realized (Krueger et al., 2016). Here, we set $f$ = 0.80 for future calculations. As shown in Figure 3.2(b), lower values of $f$ lead to a decrease of the overall spectral heat flux value and shifts the peak of the spectral heat flux to higher frequency for which the thermal occupancy is smaller, leading to a lower heat transfer coefficient according to Equation 1. On the other hand, a higher value of $f$ indicates less silicon and more vacuum, resulting in lower spectral heat flux, and decreasing the heat transfer coefficient. We note that the optimal value of $f$ for maximum heat transfer coefficient depends on temperature and carrier concentration.

Figure 3.3(a) plots the heat transfer coefficient versus thickness of the films. With a film thickness larger than 1 $\mu$m, the heat transfer coefficient remains almost constant at 600 $\mathrm{Wm^{-2}K^{-1}}$. For subsequent calculations, we assume the thickness of the films to be 1 $\mu$m unless specifically specified.

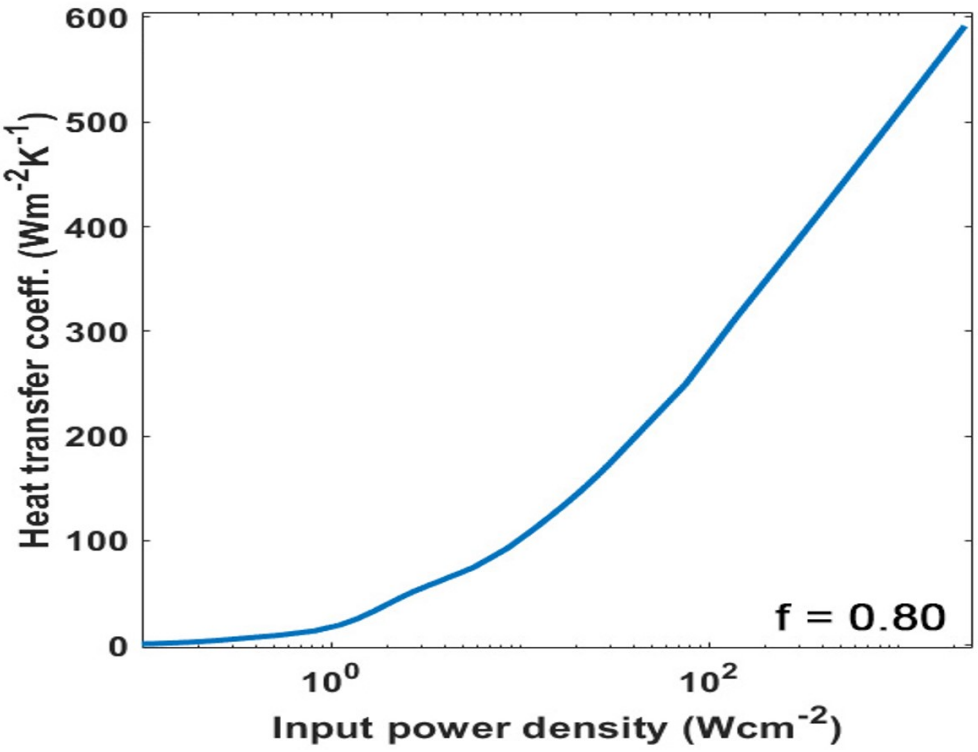


Figure 3.4: (a) Heat transfer coefficient versus input power density with $f$ = 0.80. The heat transfer coefficient is nearly zero at low optical pumping and increases to 600 $\mathrm{Wm^{-2}K^{-1}}$ with power density of $2.3\times10^3$ $\mathrm{Wcm^{-2}}$.

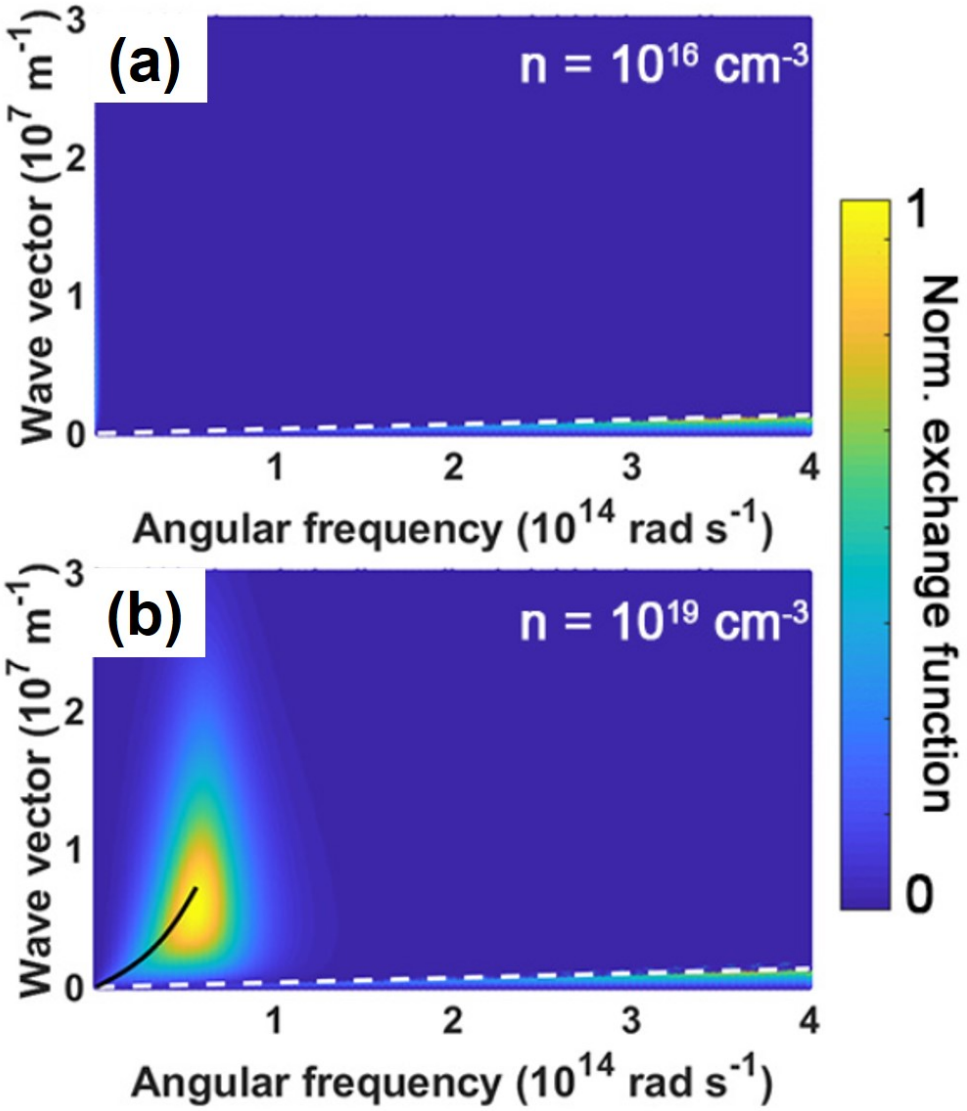


Figure 3.5: Normalized exchange function versus angular frequency and wave vector. The carrier concentration is set at (a) $10^{16}$ cm$^{-3}$, (b) $10^{19}$ cm$^{-3}$ with $f = 0.80$. The black solid curve in (b) denotes the dispersion relation of the SPP mode where the real part of $\epsilon_1$ is negative. The white dashed line is the light line in vacuum. Significant enhancement of heat transfer coefficient results from the increase of exchange function in (b) compared with (a).

External optical pumping leads to the excitation of free carriers inside the films. The curve in Figure 3.3(b) depicts the carrier concentration as a result of external pumping. At low input power, the carrier concentration remains at $10^{15}$ cm$^{-3}$ because of background doping. An increase in the optical excitation power leads to

an increase in free carrier concentration with the steady-state value determined by the recombination mechanisms. The required input power density first increases linearly with the carrier concentration in the region from $1\times10^{16}$ to $1\times10^{18}$ $cm^{-3}$ where the trap-assisted recombination and surface recombination dominates at lower carrier concentrations. However, for carrier concentrations beyond $5\times10^{18}$ $cm^{-3}$, a dramatic increase of input power density is needed to maintain the carrier concentration because the Auger recombination becomes the dominant recombination mechanism.

The heat transfer coefficient versus external optical power is shown in Figure 3.4(a). A large variation in heat transfer coefficient is observed as the pumping power is varied. Without pumping, the heat transfer coefficient is near zero. This low heat transfer coefficient results from the absolute positive value of the silicon permittivity with negligible imaginary part for the background doping of $10^{15}$ $cm^{-3}$, resulting in little emission or absorption in the infrared wavelengths. As the carrier concentration increases due to the increased optical pumping, the real part of the silicon permittivity at low frequency becomes negative while the imaginary part increases. The material is able to support surface plasmons which contribute to the near-field radiative transfer. The maximum heat transfer coefficient is 600 $Wm^{-2}K^{-1}$ for the considered input powers occurs at an input power density of $2.3\times10^{3}$ $Wcm^{-2}$.

We now compare the modulation depth of our scheme to those in prior reports. Previously, dynamic tuning of emissivity was reported with modulation of emissivity from 0.24 to 0.74 through intersubband absorption (Inoue, De Zoysa, et al., 2014) and from 0.5 to 0.95 with reconfigurable microelectromechanical systems (Xinyu Liu and Padilla, 2017) in the far field, corresponding to heat transfer coefficients of 1.5 to 4.5 $Wm^{-2}K^{-1}$ and 3.1 to 5.8 $Wm^{-2}K^{-1}$ around room temperature. In the near field, Ref. (Ito et al., 2017) reported dynamic modulation of radiative heat transfer coefficient from 17 to 30 $Wm^{-2}K^{-1}$ via phase-change material with a gap distance of 370 nm. To compare with this latter result, we recalculated the maximum variation in heat transfer coefficient for a gap distance of 370 nm. With our scheme, a modulation of heat transfer coefficient from near zero to 44 $Wm^{-2}K^{-1}$ can be achieved for the same gap distance, substantially larger than that reported earlier.

We investigate the origin of the modulation by calculating the exchange function, Eq. (2), versus angular frequency and wave vector in Figs. 3.5(a) and 3.5(b). For films with carrier concentration of $10^{16}$ $cm^{-3}$, only propagating waves under the light

line contribute to radiative transfer, leading to negligible heat transfer coefficient. However, for films with carrier concentration of $10^{19}$ cm$^{-3}$, enhanced radiative heat transfer occurs in the near field as a result of the increase in exchange function appearing above the light line, as pointed out in (S Basu, B. Lee, and ZM Zhang, 2010). Thus, the heat transfer coefficient increases quickly from 5 Wm$^{-2}$K$^{-1}$ at a carrier concentration of $10^{16}$ cm$^{-3}$ to 600 Wm$^{-2}$K$^{-1}$ at a carrier concentration of $10^{19}$ cm$^{-3}$.

To further investigate the origin of the heat transfer coefficient at a carrier concentration of $10^{19}$ cm$^{-3}$, we examine the surface mode supported by two infinitely thick porous silicon slabs. The dispersion relation of the SPPs supported in this geometry can be described by $\tanh(k_3 d/2) = -(k_3\epsilon_1)/(k_1\epsilon_3)$ and $\tanh(k_3 d/2) = -(k_1\epsilon_3)/(k_3\epsilon_1)$, where $k_j = \sqrt{k_{SPP}^2 - k_0^2\epsilon_j}$ is the wave vector in z-direction within corresponding medium with $j = 1, 3$(Maier, 2007). In the electrostatic limit ($k_{SPP} \gg \omega/c$), the dispersion relation is simplified as follows:

$$k_{SPP} \approx \frac{1}{d} \ln\left(\pm\frac{\epsilon_1(\omega) - \epsilon_3}{\epsilon_1(\omega) + \epsilon_3}\right). \tag{3.7}$$

We superimposed the results from the dispersion relation in Figure 3.5(b) as the black solid line in the region where the real part of $\epsilon_1$ is negative. It is clear that the dispersion relation matches with the peak values of the exchange function, confirming that the broadband SPP mode with high propagation constant is responsible for the enhanced heat transfer coefficient.

Next, we consider some typical values for relevant parameters for an experimental study. We take the films to have dimensions 1 cm × 1 cm, separated by a 100 nm gap. The two films are maintained at temperature of 300 and 500 K, respectively. With a tuning input power from zero to 2 W, we find that the heat transfer power can be tuned from near zero to 0.8 W. This result is significantly improved over previous results regarding the modulation depth (Inoue, De Zoysa, et al., 2014; Ito et al., 2017; Xinyu Liu and Padilla, 2017) and exceeds the blackbody limit for radiative transfer for the same temperatures by nearly a factor of three.

Finally, we consider the maximum bandwidth of modulation of the radiative flux. Modulation by simply changing the temperature of an emitter with a modulated heat flux becomes increasingly challenging as frequency increases, as discussed in the introduction. In contrast, the bandwidth of our scheme is limited only by the

recombination lifetime. A tradeoff exists between bandwidth and required optical power as a shorter recombination time implies high bandwidth but requires more power to maintain a given free carrier concentration. For the parameters chosen here, at a carrier concentration of $10^{18}$ $cm^{-3}$, the lifetimes corresponding to trap-assisted, surface and Auger recombination are around 20, 1.8 and 23 $\mu$s, respectively, leading to a modulation bandwidth of around 600 kHz. Generally, the maximum modulation frequency will be on the order of hundreds of kHz for typical values of recombination lifetimes, which is faster than or comparable to previous results (Hildenbrand et al., 2010; Inoue, De Zoysa, et al., 2014; Ito et al., 2017; Xinyu Liu and Padilla, 2017).

## 3.4 Conclusions

In summary, we have proposed a dynamic modulation scheme for near-field radiative transfer using free carrier changes induced by external optical pumping. For the materials considered here, we show that the heat transfer coefficient can be tuned from near zero to around 600 $Wm^{-2}K^{-1}$ with bandwidths of hundreds of kHz. Our work introduces a promising method to address the challenge of dynamic external control of heat flow.

*Chapter 4*

# SPECTRALLY SELECTIVE SOLAR ABSORBER BASED ON GERMANIUM PHOTONIC CRYSTALS AND BLACK SILICON

Spectrally selective absorbers with high absorption in the solar spectrum from ultra-violet to near infrared and low emissivity in the mid-/far-infrared are critical for efficient solar energy conversion. Conventionally, spectrally selective solar absorbers are widely used in solar hot water systems and concentrating solar power plants, as well as being actively studied in solar thermoelectric generators and solar thermophotovoltaic systems.

In this chapter, we describe two different spectrally selective solar absorbers, one made from germanium photonic crystals and the other from black silicon. Both numerical simulation and experimental results are presented.

## 4.1 Introduction

Harvesting the solar energy is of great benefit due to its unmatched resource potential. The majority of efforts have been focused on the research and development of photovoltaics for electricity, solar thermal techniques for electricity or heat, and artificial photosynthesis for fuels (Kraemer et al., 2011; Green et al., 2011; Bard and Fox, 1995). Among them, the solar-heat conversion is particularly useful due to its high conversion efficiency (Ni et al., 2016; Weinstein et al., 2015). In order to harvest the heat generated from the absorption more efficiently, a high temperature heat source is preferred according to Carnot's theorem. Thus, an absorber with unity absorption in the solar spectrum and zero emissivity in the mid-/far-infrared is ideal for this purpose (Cao, McEnaney, et al., 2014).

In history, different schemes of spectrally selective surfaces have been investigated. Among them is the cermet that includes single, double and triple layers. Various combinations of host materials have been demonstrated, including $Al_2O_3$, AlN, and $SiO_2$ with metallic filling materials such as Ni, Co, Ti, Mo, W, Pt, Cu, and Ag (Cao,

Kraemer, et al., 2015; Barshilia et al., 2009; Sathiaraj et al., 1990; Soum-Glaude et al., 2017). Another type is based on nano-/micro-scale photonic engineering. Nickel nanopyramid arrays with anti-reflection coating (P. Li et al., 2015). For example, two dimensional photonic crystals made from thin film tungsten were shown to support wideband absoprtion due to the multiple resonance (Yeng et al., 2012). Three dimensional metallic photonic crystals were also experimentally realized and can sustain high temperature up to 1400 degrees Celcius (Arpin et al., 2013). Multilayer dielectric/semiconductor materials achieved an absorptance of 76% in the solar spectrum and a low emissivity of around 5% at thermal wavelengths (Thomas et al., 2017). However, most of them do not have a high enough absorption in the solar spectrum (typically less than 90%) and low enough emissivity in the mid-/far-infrared (typically less than 10%). Besides, the transition region from high absorption to low absorption is broad (typically wider than 1 $\mu$m).

Here, we theoretically designed and experimentally fabricated two different spectrally selective absorbers based on interband transition of two semiconductor materials: germanium and silicon. Simulations show that both absorbers have a high absorption in the solar spectrum while maintaining a low emissivity in the mid-/far-infrared and the transition region is less than 1 $\mu$m. Experimental results shown that the germanium photonic crystals have a similar spectrum as predicted by the simulation, and the black silicon could achieve a steady state temperature of 130 degrees Celsius under unconcentrated solar illumination and over 200 degrees in concentrated (4×) illumination. This opens up great potential in solar thermal energy applications including thermophotovoltaics, solar steam generation, and seawater desalination, etc.

## 4.2 Theory

Spectrally selective absorbers must efficiently convert solar energy into heat. Here, we define an effective absorptivity (or equivalently emissivity) by taking the spectral absorptivity into consideration.

$$\epsilon_{eff} = \frac{\int d\lambda \epsilon_{dev}(\lambda, \Psi) I_{AM1.5}(\lambda)}{\int d\lambda I_{AM1.5}(\lambda)} \tag{4.1}$$

with $\epsilon_{dev}(\lambda, \Psi)$ being the emissivity or absorptivity of the absorber as a function of wavelength while $I_{AM1.5}(\lambda)$ is the spectral radiance of the solar illumination, in unit of $\mathrm{Wm^{-2}nm^{-1}}$.

On the other hand, to study the steady state temperature that the absorber can achieve, we first investigate the energy balance of the spectrally selective absorber under solar illumination. We take the absorber to be at temperature $T_{dev}$ and the ambient atmospheric temperature to be $T_{amb}$. At steady state, the energy balance equation is shown as the following:

$$P_{sun} = P_{rad}(T_{dev}) + P_{con}(T_{amb}, T_{dev}), \tag{4.2}$$

where the absorbed power density by the device with surface facing the sun at angle $\Psi$ is given by

$$P_{sun} = \cos(\Psi) \int d\lambda \epsilon_{dev}(\lambda, \Psi) I_{AM1.5}(\lambda). \tag{4.3}$$

$P_{rad}$ denotes the radiated power density of the device:

$$P_{rad}(T_{dev}) = \int d\Omega \cos(\theta) \int d\lambda I_{BB}(T_{dev}, \lambda) \epsilon_{dev}(\lambda, \theta) \tag{4.4}$$

with $I_{BB}(T_{dev}, \lambda)$ indicating the spectral radiance of a blackbody at temperature $T_{dev}$.

The last term $P_{con}(T_{amb}, T_{dev})$ is the power density of thermal conduction and convection parasitically transferred from the absorber:

$$P_{con}(T_{amb}, T_{dev}) = h_{con}(T_{dev} - T_{amb}), \tag{4.5}$$

where $h_{con}$ is the thermal coefficient.

The green shaded area in Figure 4.1 shows the solar spectral radiance from UV to infrared named as AM 1.5 while the solid purple line is the blackbody radiation at 600 K. We can easily identify that if the spectrally selective absorber has a sharp transition from high absorption to low absorption around 1.5 $\mu$m, it will collect most of the solar radiation while emitting little, being able to boost its steady state temperature.

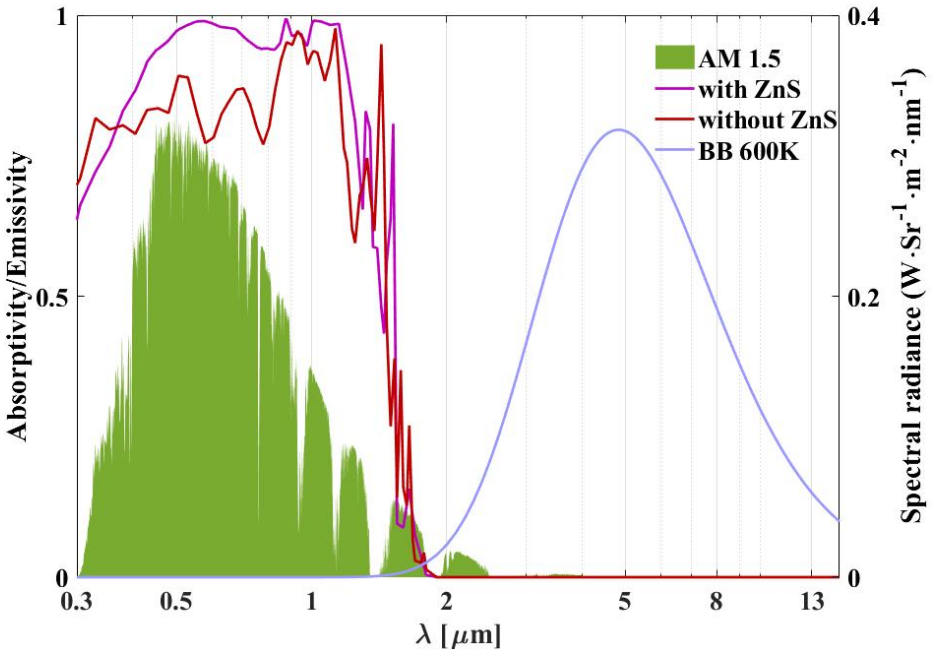


Figure 4.1: Simulated absorption (or emissivity) spectrum of the germanium photonic crystal with and without the top ZnS thin film coating. The later has a higher absorption from 400 nm to 1 $\mu$m where the solar spectrum has its highest value while remains almost the same otherwise.

### 4.3 Results and discussion of germanium photonic crystals

The first structure we designed is the germanium photonic crystal structure consisting periodic germanium holes covered with a conformal ZnS thin layer schematically illustrated in Figure 4.2. The whole structure sits on top of a silicon wafer that is back-coated with a silver layer, minimizing the emission from the backside. The photonic crystals are arranged in a hexagonal lattice with closest lattice distance of $p$ = 1 $\mu$m. The germanium holes have diameter of $d$ = 475 nm and height of $t$ = 1.2 $\mu$m. The silver layer underneath the germanium works as a reflector in the mid-/far-infrared. Finally, the patterned germanium layer is covered with a thin layer of ZnS, working as an air-insulation layer for the germanium and also as a absorption boosting layer as will be discussed later.

We first simulate the absorption spectrum of the structure without ZnS thin film in the spectral range of interest. The simulation is performed on a unit cell (Figure 4.3(h)) with the finite element method and finite-difference time-domain (FDTD)

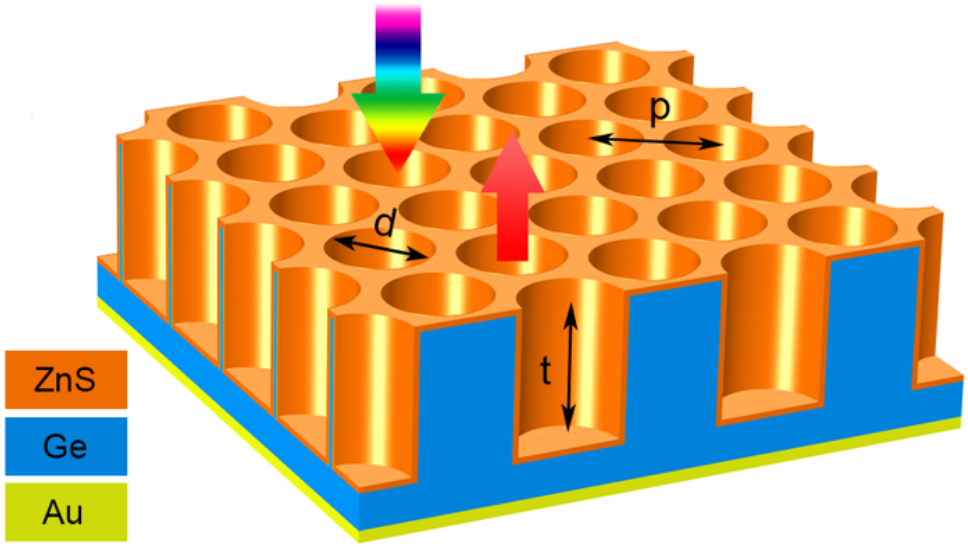


Figure 4.2: Schematic diagram of the spectrally selective solar absorber based on Ge photonic crystals. $p$ = 1 $\mu$m, $d$ = 475 nm and $t$ = 1.2 $\mu$m are the period of the photonic crystals, diameter of the holes and depth of the holes, respectively. Different colors represent different materials as shown in the figure. The supporting substrate (silicon wafer) is not shown in this picture.

with periodic boundary conditions in the x-z and y-z plane. During the simulation, a perfectly matched layer is used for absorbing the reflection from the structures. The results are shown as the red line in Figure 4.1. As can be seen, the absorption is about 80% from 300 nm to 1.5 $\mu$m. To increase the absorption, we added a thin layer of ZnS with thickness of 60 nm on the top and sidewall of the patterned germanium photonic crystals. In this way, the absorption of the structure is boosted to about 95% from 500 nm to 1 $\mu$m, where the solar spectrum has its highest value while remaining almost the same in the other spectrum region. The detailed electric field distribution at different wavelengths is plotted in 4.3. In this particular simulation, an incident field with x-polarization from normal direction is assumed.

With the design in hand, we set out to experimentally fabricate the device with process shown in Figure 4.4.

(a) A double-side polished silicon wafer is first cleaned and coated with a titanium/silver with electron beam evaporation on the bottom side. It works to minimize the thermal emission from the bottom side since silver has a high reflection (or low emissivity) from visible to far-infrared. The wafer is then flipped and coated

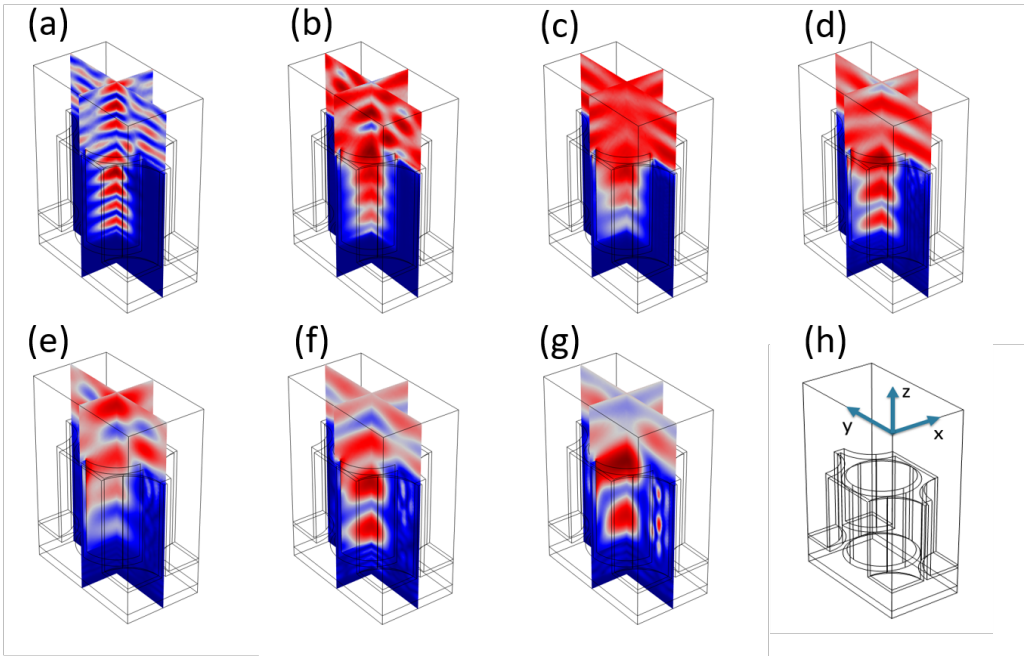


Figure 4.3: (a) - (g) The simulated electric field distribution of a unit cell of the germanium photonic crystal with periodic boundary conditions at wavelengths from 400 nm to 1000 nm with 100 nm interval. (h) The unit cell under study.

sequentially with a titanium layer (5 nm) at a speed of 0.05 nm/s, a silver layer (100 nm) at a speed of 0.1 nm/s and a germanium layer (2.5 $\mu$m) at a speed of 0.15 nm/s. The titanium layer works as an adhesion layer between silver and silicon.

(b) The coated wafer is then spin-coated with a photoresist layer (PMMA) at a speed of 4000 round per minute. The photoresist is then written by a 100 keV electron beam lithography system, followed by developing.

(c) The wafer is then transferred again to the electron beam deposition chamber and a 30 nm $Al_2O_3$ layer is deposited at a speed of 0.1 nm/s. The $Al_2O_3$ hard mask layer is further formed by a lift-off process in acetone. The SEM top view of the $Al_2O_3$ hard mask is shown in Figure 4.5 (a).

(d) With the hard mask, the wafer is processed in an inductively coupled plasma – reactive ion etching (ICP-RIE) etcher with a pseudo-Bosch technique. The active gas used is $O_2$ and $SF_6$. The forward power is 25 W. The wafer temperature during etching is set at 15°. The whole dry etching process lasts about 5 minutes. The pseudo-Bosch technique gives a sharp and smooth vertical wall for the germanium

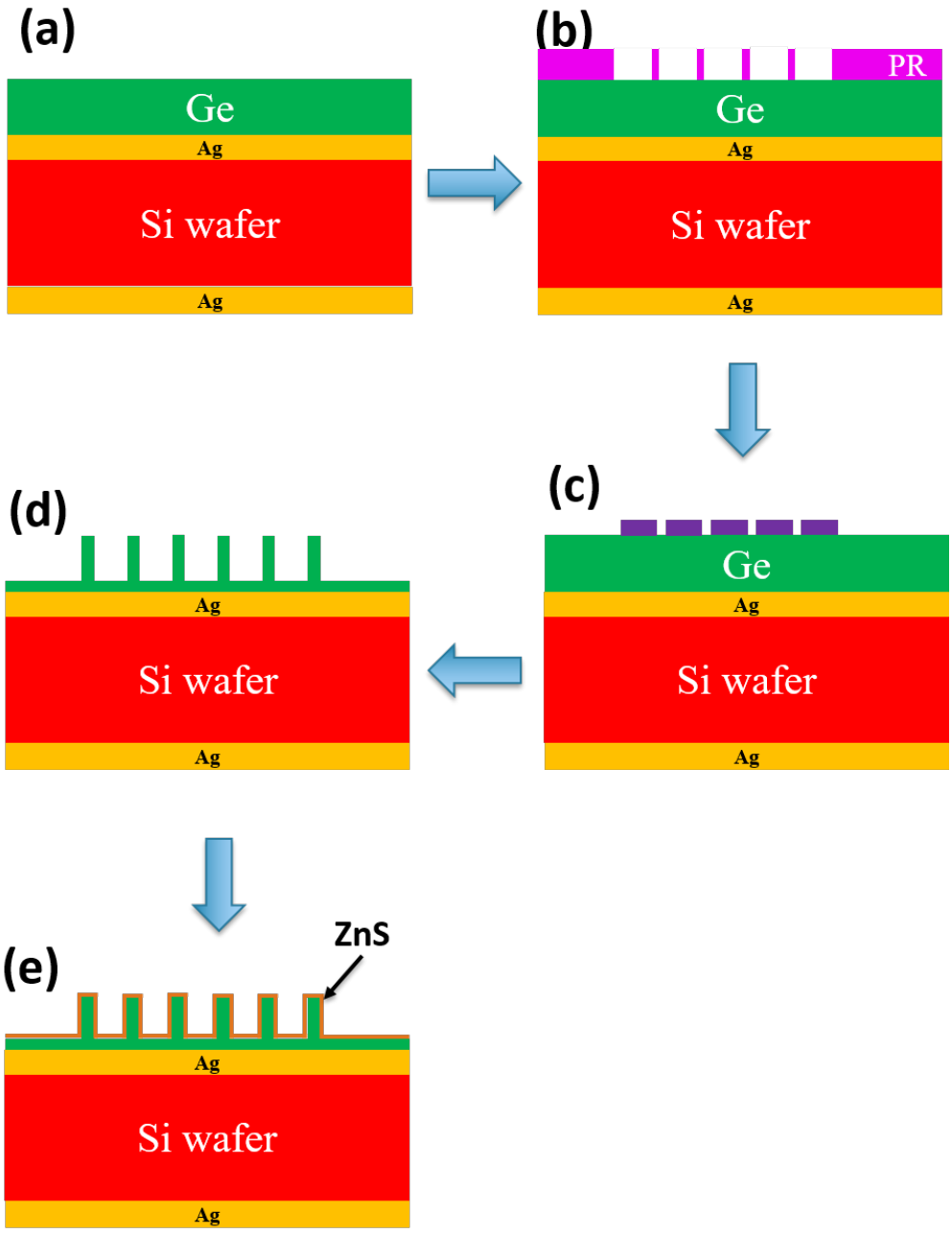


Figure 4.4: (a) Thin film coating on both sides of polished silicon handling wafer. Note that the Ti layer is not shown in figure. (b) E-beam lithography of the photonic crystal pattern. (c) Hard mask making with $Al_2O_3$ deposition and lift-off. (d) Dry etching to form the germanium photonic crystals. (e) Conformal coating of ZnS layer.

photonic crystal, as the SEM image shows in Figure 4.5 (b).

(e) The structure is finally coated with a ZnS layer of 60 nm by sputtering.

The spectrum of the sample is measured in two setups. For the short wavelength range from 300 nm to 1100 nm, a UV-Vis-NIR spectrum analyzer in reflection mode is used. For the mid-/far-infrared spectrum, a Fourier transform infrared spectroscopy (FTIR) system is used. The absorption (or emissivity) spectrum are shown in Figure 4.6 through converting reflection ($R$) to absorption by 1 - $R$, since there is no transmission. The measured results show high absorption from 300 nm to 1100 nm, close to the simulated results. According to the previous definition of effective absorptivity, we calculate its value to be 0.91 for normal incidence considering the wavelength length range we can measure. The emissivity in the mid-far-infrared is mostly low except a peak around 8 $\mu$m with a maximum value of 0.15. The temperature stability of the sample is tested by recording the infrared spectrum under different temperatures shown in Figure 4.7. Experimental results show that the sample is able to sustain temperature as high as 200 degrees Celcuis for over two hours.

## 4.4 Results and discussion of black silicon

Due to the fact that the feature size of the germanium photonic crystals are around hundreds of nanometer and the patterns are dense, very long time electron beam lithography needs to be employed if a feasibly large sample is to be fabricated. To enable the fabrication of large spectrally selective absorber samples, we further tried another solution, the black silicon.

The spectrally selective absorber made from black silicon is schematically shown in Figure 4.8. It consists of a top impedance matching silicon grass layer (approximately 5 $\mu$m thick), an undoped silicon base layer (approximately 520 $\mu$m thick), a bottom germanium layer (1.5 $\mu$m thick) and a final Ti/Ag (5 nm/100 nm) back reflector. Germanium layer is used since it has a lower band gap and helps increase the absoprtion in the spectrum beyond the band gap of silicon which is 1.12 eV.

Since the thickness of the base layer of silicon is much larger than the wavelength, it results in great difficulty in full wave simulation. To overcome that and give

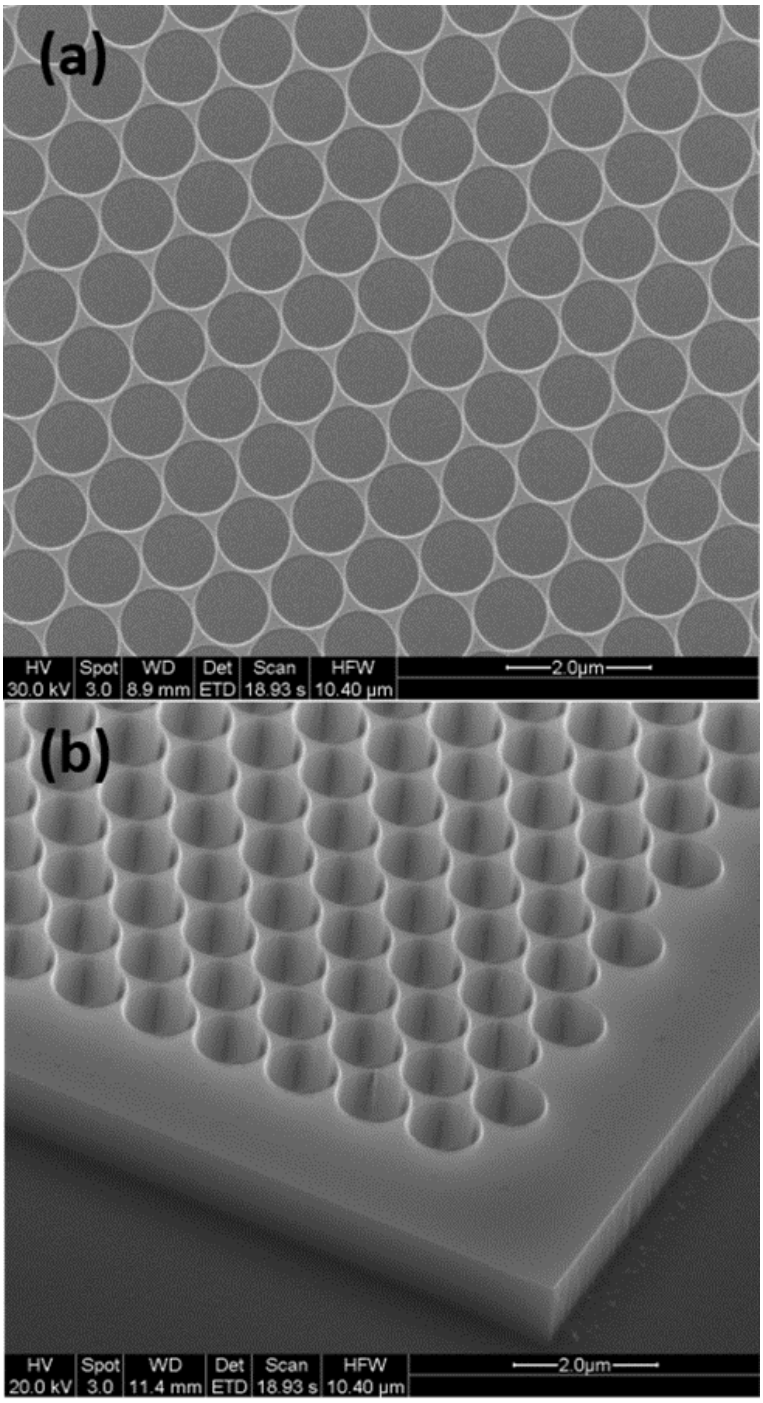


Figure 4.5: (a) SEM top view of the $Al_2O_3$ hard mask after lift off, corresponding to Figure 4.4 (c). (b) SEM tilted view of the germanium photonic crystals after dry etching, corresponding to Figure 4.4 (d).

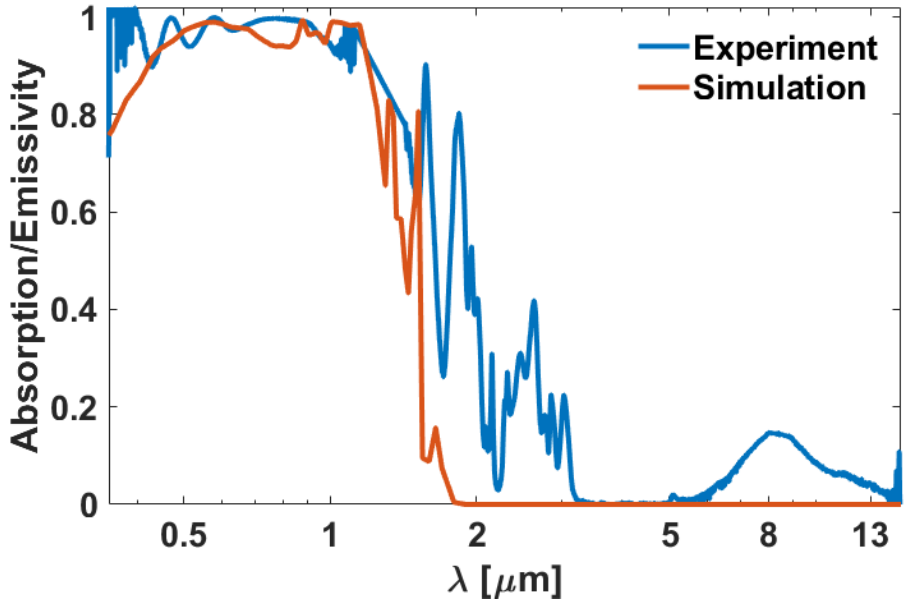


Figure 4.6: Absorption (or emissivity) spectrum of the germanium photonic crystals from visible to infrared.

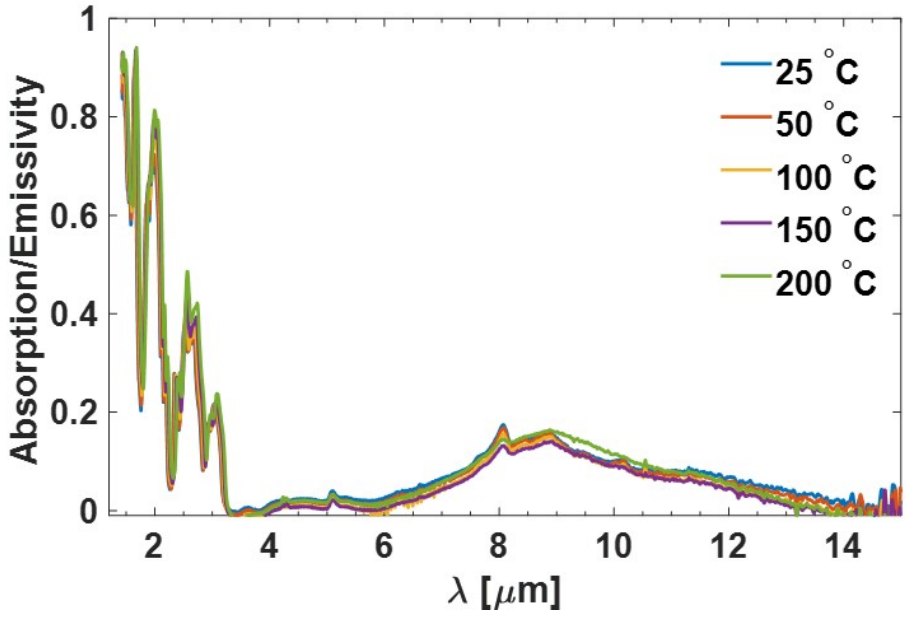


Figure 4.7: Absorption (or emissivity) spectrum of the germanium photonic crystals in the infrared under different temperature.

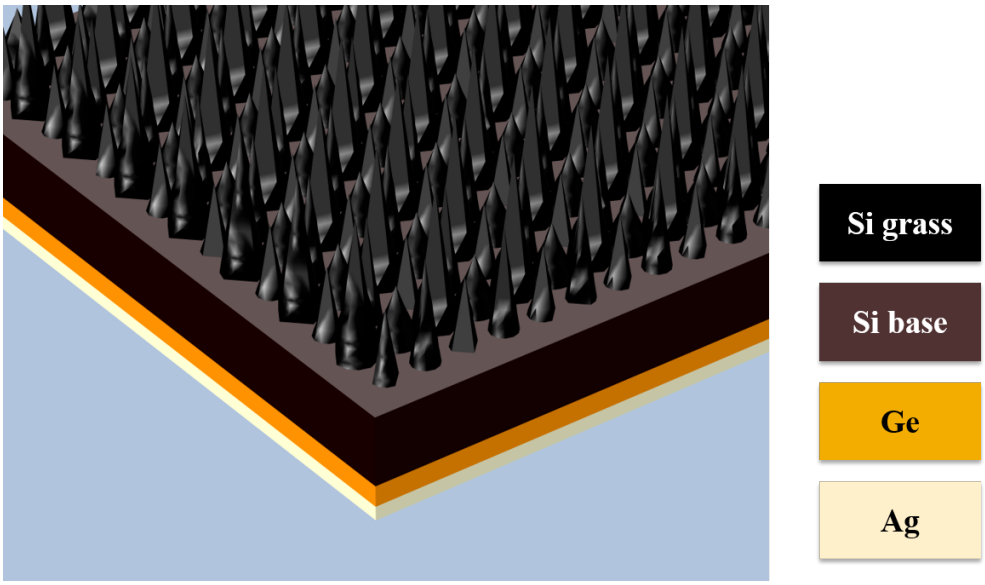


Figure 4.8: Schematic illustration of the black silicon spectrally selective absorber. It consists of a top impedance matching silicon grass layer, an undoped silicon base layer, a bottom germanium layer, and a final Ti/Ag back reflector.

reasonable results, we set the imaginary part of the refractive index of the base layer to be 150 times larger than its original value and the thickness of the base layer to be 3 $\mu$m.

Although the top grass is randomly distributed, to minimize the simulation volume, periodic boundary conditions of a unit cell are employed. A port is set at the top of the unit cell, lunching the input electromagnetic wave. A perfectly matched layer is used above the port, minimizing any reflection that will cause error for the simulation.

The simulated results with the electric field distribution at different wavelength are shown in Figure 4.9 (a) to (e) and the absorption (or emissivity) spectrum in Figure 4.9 (f). For light with short wavelength less than 0.8 $\mu$m, absorption occurs at the top grass layer (Figure 4.9 (a)), while for light at 1.0 $\mu$m, most of the absorption happens in the thick base layer (Figure 4.9 (b)). For even longer wavelength that is below the bandgap of silicon but above the bandgap of germanium, absorption occurs in the germanium layer (Figure 4.9 (c)). For wavelengths in the mid-/far-infrared, there is no absorption and all the wave gets reflected by the bottom reflector (Figure 4.9 (d) and (e)). The transition from hight absorption to low absorption is around the

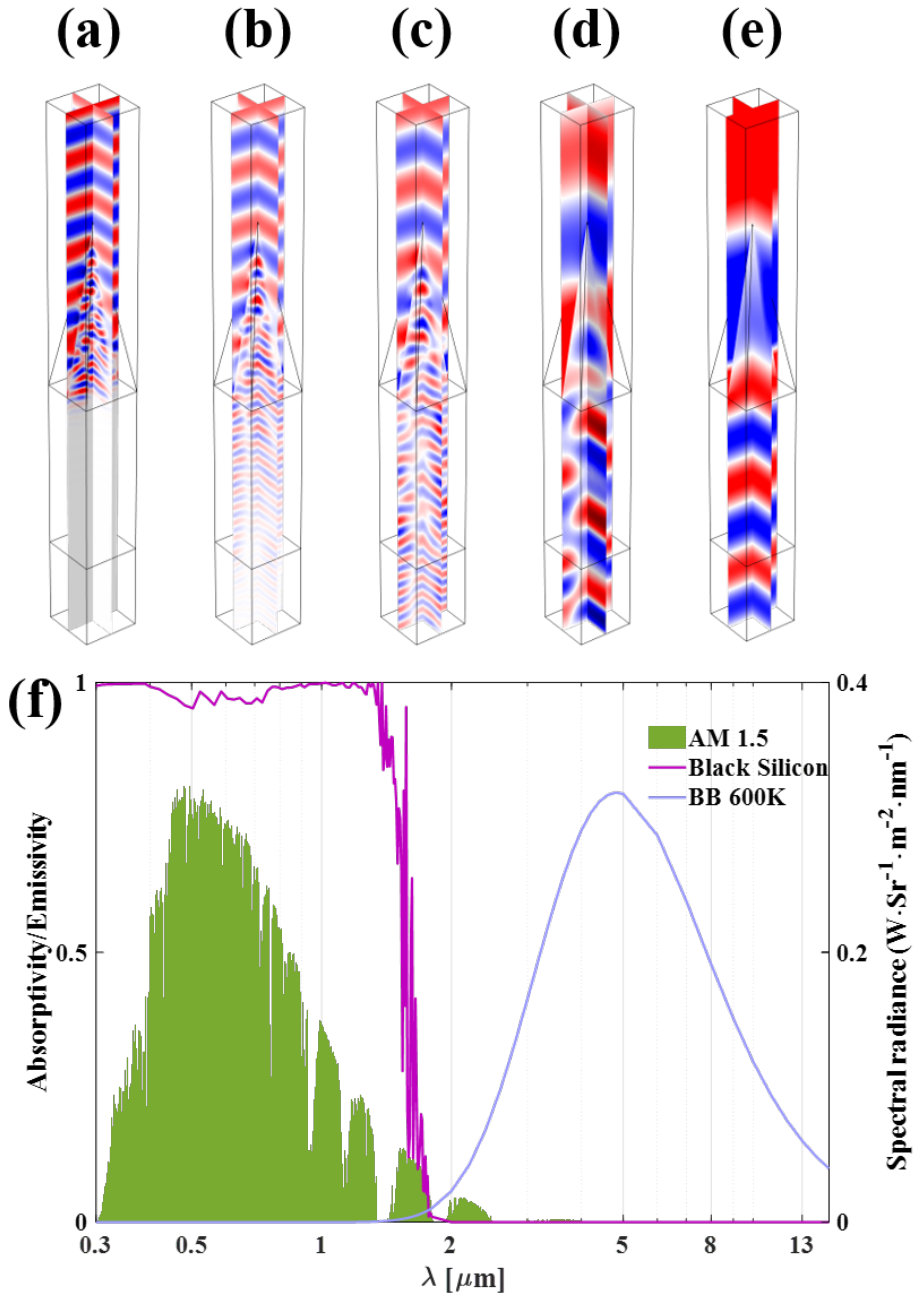


Figure 4.9: Electromagnetic simulation of the black silicon spectrally selective absorber under with different wavelengths: (a) 0.8 $\mu$m, (b) 1.0 $\mu$m, (c) 1.3 $\mu$m, (d) 3.0 $\mu$m, and (e) 6.0 $\mu$m. (f) The simulated absorption (or emissivity) spectrum from visible to infrared.

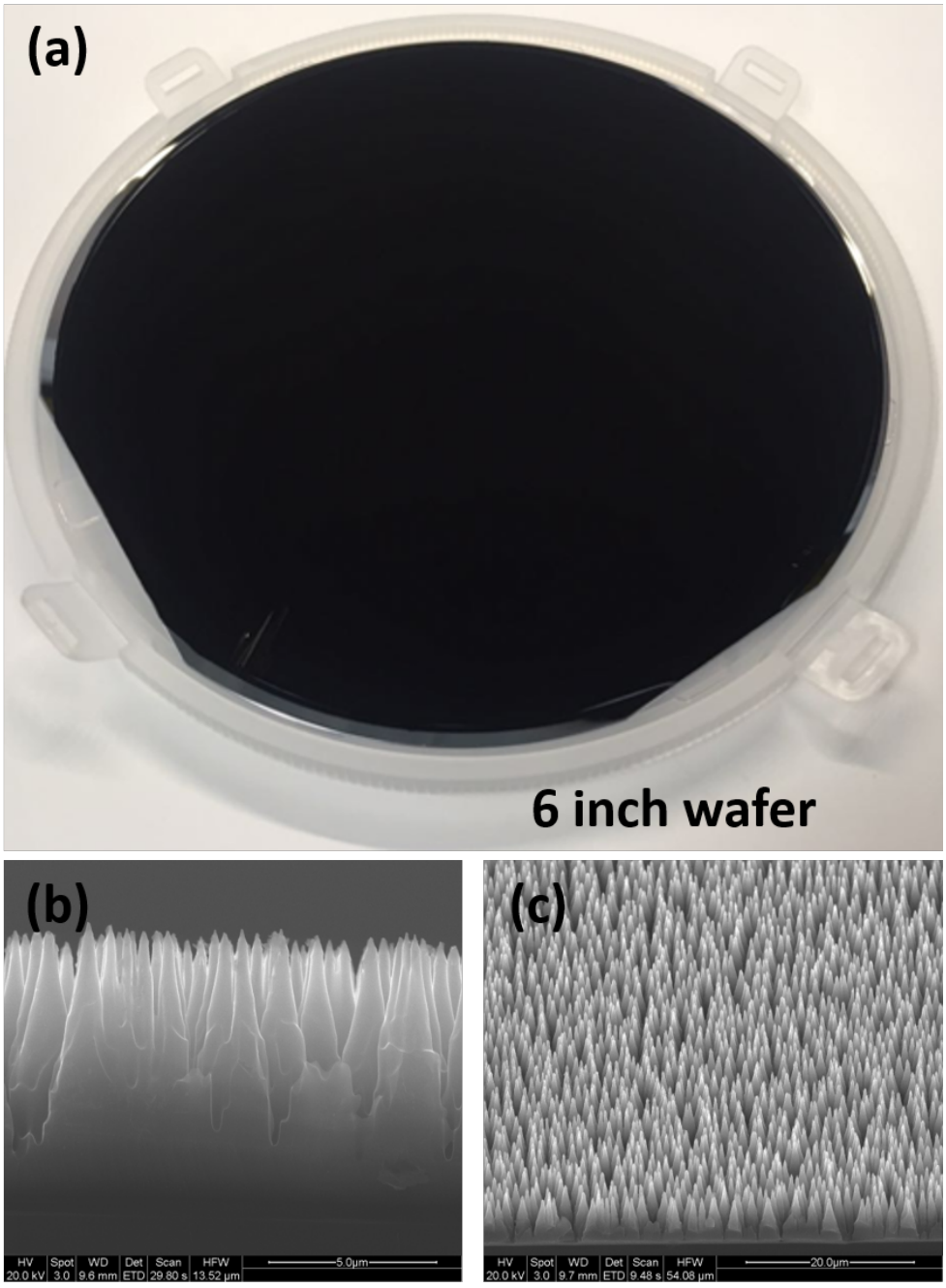


Figure 4.10: (a) A 6-inch-size black silicon wafer. (b) and (c) Side view and tilted view of the black silicon taken with SEM.

bandgap wavelength of germanium as shown in Figure 4.9 (f).

Experimentally, the sample is fabricated with an double-side polished undoped silicon wafer with resistivity larger than 10k Ohm-cm. The cleaned wafer is first

processed with a two-step etching process A and B by inductively coupled plasma reactive ion etching (ICP-RIE). In Process A, we use 85 sccm (sccm stands for standard cubic centimeters per minute) $SF_6$ and 20 sccm $O_2$ under pressure of 10 mTorr. The forward power is set at 8 W while the ICP (ICP stands for inductively coupled plasma) power is set at 1000 W. In Process B, the forward power is changed into 6 W and the flow rate of $O_2$ is changed into 12 sccm. Both steps are maintained at -145 degree Celsius. The back side of the silicon wafer is further coated with a 1.5 $\mu$m thick germanium layer and a Ti/Ag (5 nm/100 nm) back reflector using electron beam evaporation method. The front side of the final sample is shown in Figure 4.10 (a) which is visually black. Its corresponding SEM image is shown in (b) and (c). The silicon grass features a height of about 4.5 $\mu$m with a density of about $2.5\times10^7$ $cm^{-2}$.

Due to the fact that the randomly distributed grass could potentially cause strong scattering from the input light, the spectrum measurement should be performed with integration sphere. Here, we utilized the Cary 5000 UV/vis/NIR armed with an integrating sphere for characterizing the spectrum from UV to near infrared. Figure 4.11 shows the measurement results for two different samples, one is the silicon grass with back reflector coating (Ti/Ag) and the other is the silicon grass with a coating of Ge/Ti/Ag on the back. It is easily identified that the absorption below 1.1 $\mu$m (corresponding to the band gap of silicon) is nearly 100% and decreases with longer wavelength. According to the previous definition of effective absorptivity, we calculate its value to be 0.96 for normal incidence considering the wavelength length range we can measure. However, with an additional germanium layer of 1.5 $\mu$m in thickness, the absorption from 1.1 $\mu$m to 1.8 $\mu$m can be boosted by 10%.

We were not able to measure the spectrum in the mid-far-infrared due to a lack of integration sphere in the spectrum range. We further set out to test its temperature under solar illumination. The performance of the black silicon wafer is tested inside a vacuum chamber under the illumination of a solar simulator. The temperature of the wafer and the ambient air of the chamber is monitored by two K-type thermal couples. To ensure good thermal contact, the head of the thermal couple is bonded to the back surface of the absorber with thermal cement (Omegabond OB-700). In order to achieve high temperature, special care needs to be taken of the measurement setup, especially reducing parasitic conduction and convection. The chamber pressure is kept below 0.01 Pa during the entire measurement period to cut down air conduction

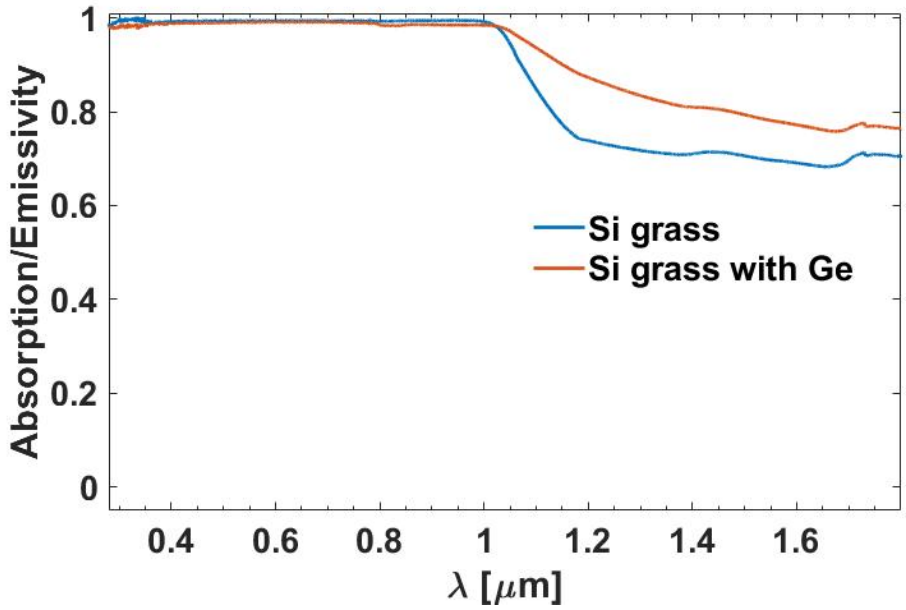


Figure 4.11: Measured absorption (or emissivity) spectrum of the silicon grass with and without germanium back coating from UV to near infrared.

and convection.

We test the fabricated black silicon spectrally selective absorber under both unconcentrated and concentrated (4×) conditions with the measurement results shown in Figure 4.12. In both cases, after the solar simulator is turned on, the temperature of the black silicon first rises from room temperature and gradually stabilizes at a steady state temperature of 131 and 214 degrees Celsius, respectively. After the solar simulator is turned off, its temperature drops off and finally reaches the temperature of the air. The measured temperature is lower than that of the commercially available spectrally selective absorber tested under the same condition. The later reaches 200 degrees Celsius under unconcentrated condition. We attribute the difference to the potentially high emissivity of our sample in the mid-/far-infrared. Although we were not able to measure the emissivity directly in that spectrum range, we can infer from Figure 4.12 that the black silicon has high emissivity beyond its band gap. For example, at the wavelength of 1.8 $\mu$m (the longest wavelength we can measure with an integration sphere), the emissivity is 78%.

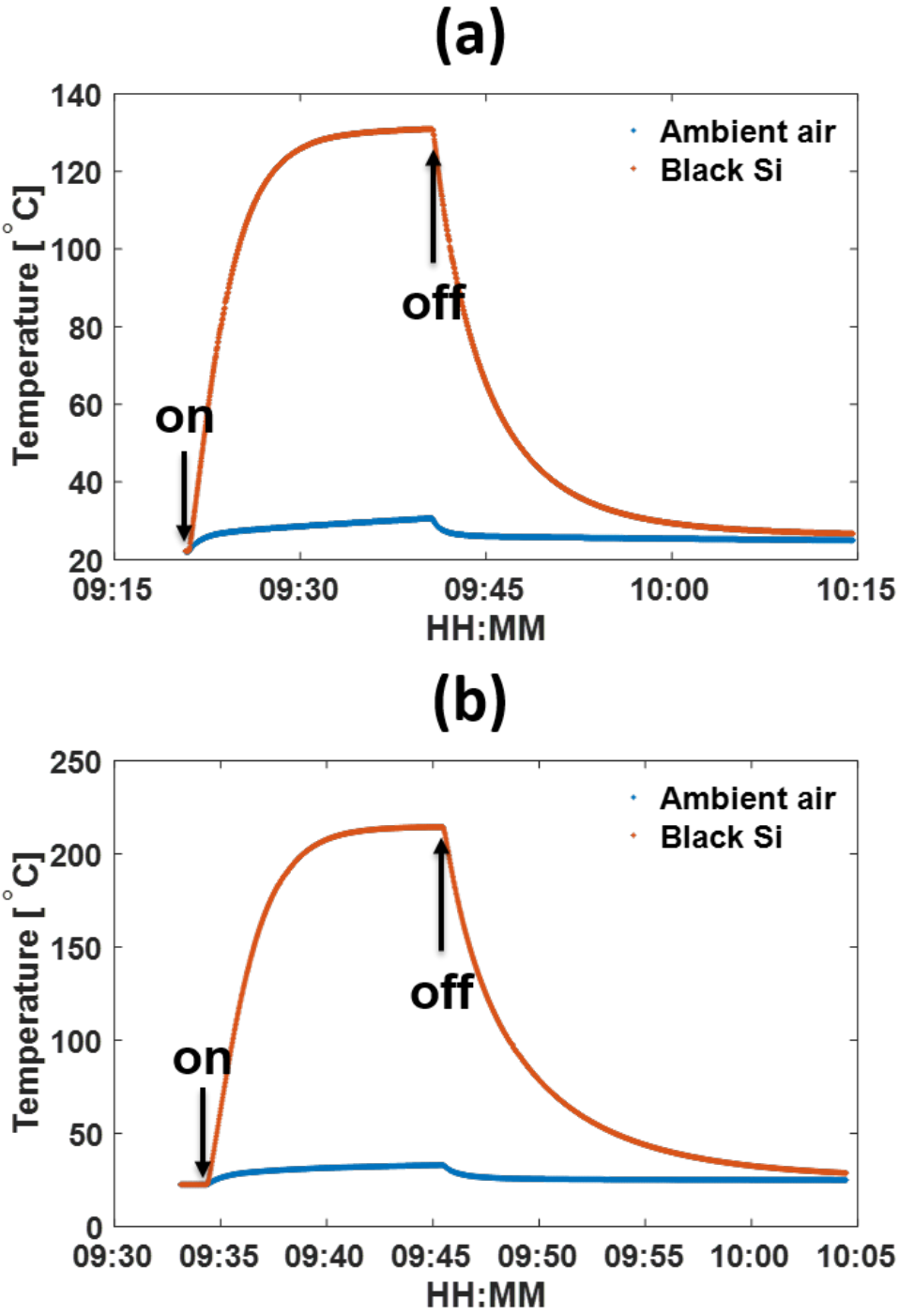


Figure 4.12: Temperature measurement of the black silicon spectrally selective absorber under (a) unconcentrated and (b) concentrated solar illumination. The arrows denote the moment when the solar simulator is turned on and off.

## 4.5 Conclusions

In this chapter, we have numerically designed and experimentally fabricated two spectrally selective absorbers based on semiconductors. These two schemes both exploit the advantage of the sharp absorption transition of germanium and silicon as well as structural design that minimize the reflection in the visible and near infrared region. The germanium photonic crystal structure is able to get > 90% absorption from UV to near infrared while the black silicon achieves near 100% absorption. The drawback of the germanium photonic crystal structure is that it requires b-beam lithography, which is expensive and time consuming, and thus not suitable for large scale fabrication.

*Chapter 5*

# DAYTIME RADIATIVE COOLING USING INFRARED BLACKBODIES

Part of this chapter has been adapted from:

Kou, Junlong, Zoila Jurado, Zhen Chen, Shanhui Fan, and Austin J Minnich (2017). "Daytime radiative cooling using near-black infrared emitters". In: *ACS Photonics* 4.3, pp. 626–630. DOI: 10.1021/acsphotonics.6b00991.

Recent works have demonstrated that daytime radiative cooling under direct sunlight can be achieved using multilayer thin films designed to emit in the infrared atmospheric transparency window while reflecting visible light. Here, we demonstrate that a polymer-coated fused silica mirror, as a near-ideal blackbody in the mid-infrared and near-ideal reflector in the solar spectrum, achieves radiative cooling below ambient air temperature under direct sunlight (8.2 °C) and at night (8.4 °C). Its performance exceeds that of a multilayer thin film stack fabricated using vacuum deposition methods by nearly 3 °C. Furthermore, we estimate that the cooler has an average net cooling power of about 127 $Wm^{-2}$ during daytime at ambient temperature even considering the significant influence of external conduction and convection, more than twice that reported previously. Our work demonstrates that abundant materials and straight-forward fabrication can be used to achieve daytime radiative cooling, advancing applications such as dry cooling of thermal power plants.

## 5.1 Introduction

Manipulating thermal emission from surfaces by thermal photonic design has received great attention in recent years (Xianliang Liu et al., 2011; Greffet et al., 2002; Schuller, Taubner, and Brongersma, 2009; De Zoysa et al., 2012; Yeng et al., 2012; A. P. Raman et al., 2014; Inoue, De Zoysa, et al., 2014; L. Zhu, A. P. Raman, and Fan, 2015; Bierman et al., 2016; Ilic, Bermel, et al., 2016; L. Zhou et al., 2016). In particular, passive radiative cooling schemes that do not require external

active devices such as fans, air conditioners, or thermoelectrics are of much interest because of their potential to reduce energy consumption (Rephaeli, A. Raman, and Fan, 2013; C. Granqvist and Hjortsberg, 1980; A. Gentle, Aguilar, and G. Smith, 2011; Shi et al., 2015; Hsu, A. Y. Song, et al., 2016). Radiative cooling refers to the physical process by which a body dissipates heat to another body of lower temperature via thermal radiation. The coldest known heat sink is the universe with a temperature of around 3 K, and radiative thermal contact can be made with this thermal reservoir by exchanging energy through the transparency window of the atmosphere. Historically, radiative cooling during nighttime has been widely studied and employed for rooftop cooling (Michell and Biggs, 1979; A. Gentle, Aguilar, and G. Smith, 2011; T. M. Nilsson and Niklasson, 1995; T. M. Nilsson, Niklasson, and C. G. Granqvist, 1992; Catalanotti et al., 1975). However, radiative cooling during daytime is more useful as cooling demand peaks during daytime hours.

Recently, a passive radiative cooling scheme has been reported by Raman et al. that achieves this goal by radiating energy through the main atmospheric transparency window in the range of 8 - 13 $\mu$m while reflecting incident sunlight (A. P. Raman et al., 2014). Their radiative cooler consisted of seven alternating layers of $SiO_2$ and $HfO_2$ on top of a silver back reflector, resulting in 97% reflection of solar illumination and an average emissivity of about 0.65 in the transparency window. With a relatively simple experimental apparatus, Raman et al. was able to achieve a 5 °C degree reduction below the ambient air temperature under direct sunlight. Subsequently, Chen et al. was able to demonstrate an average temperature reduction of 37 °C below ambient by combining a selective emitter with an apparatus consisting of a vacuum chamber (Z. Chen et al., 2016). Related to these experiments, there have been other recent theoretical works in designing various photonic structures for radiative cooling purposes (L. Zhu, A. Raman, and Fan, 2013; Rephaeli, A. Raman, and Fan, 2013; A. R. Gentle and G. B. Smith, 2010; Hossain, Jia, and Gu, 2015; Huang and Ruan, 2017).

Most of these radiative coolers are designed to emit only in the atmospheric transparency window to avoid exchanging radiation with the atmosphere. This requirement leads to complex photonic designs, for instance consisting of multilayer stacks that require vacuum deposition methods. It is interesting to consider whether emitting and absorbing outside of the main atmospheric transparency window is necessarily detrimental. If not, materials that are naturally visibly transparent yet

emit strongly over a broad bandwidth in the mid-infrared, such as glasses, could perform as well as other more complex photonic structures reported previously.

## 5.2 Different design for passive radiative cooling

Here, we designed three different structures for passive radiative cooling purpose. The first one is based on $Si_3N_4$ photonic crystals with a unit cell shown in Figure 5.1. We choose photonic crystal structure since it has been shown in the last chapter that photonic crystals are able to achieve broadband absorption. After dedicated design, the final photonic crystals are arranged in a hexagonal lattice in the x-y plane. The final optimized structure has a substrate base height $h_{base}$ of 1 $\mu$m, a hole height $h_{hole}$ of 5 $\mu$m, a hole radius $r_{hole}$ of 3.5 $\mu$m and a lattice period $period$ of 8 $\mu$m. The back side is assumed to be coated with a silver layer for high reflection in the visible and near infrared region.

The complex refractive index of $Si_3N_4$ is adapted from (Kischkat et al., 2012) and is plotted here in Figure 5.2. For wavelength less than 3 $\mu$m, $Si_3N_4$ is transparent ($n_{imag}$ less than 0.0003) and it has been used for achieving low-loss waveguide and high-$Q$ resonators in photonics in the visible and near infrared (K. Y. Yang et al., 2016; Okawachi et al., 2011; Moss et al., 2013). In the mid-/far-infrared, a clear broadband peak for the imaginary part is seen from 8 to 15 $\mu$m, resulting from the strong phonon polariton resonances, indicating potentially high absorption (or equivalently emissivity). However, the strong refractive index mismatch between air and $Si_3N_4$ will result in strong reflection (or low emissivity) for bulk materials. Thus, photonic crystal structure is employed to solve this problem. The simulation is performed with finite-difference time-domain (FDTD) method by setting periodic boundary conditions in the x and y direction. The top and bottom regions in z-direction are set to be perfectly matched layers (PMLs). The incident wave is characterized by the polar angle $\theta$, azimuthal angle $\phi$ and polarization.

Figure 5.3 and Figure 5.4 shows the simulated spectrum in the atmospheric window with different polar angles and azimuthal angles for the two polarizations.

The second scheme we explored is the $Si_3N_4$ pyramid structure arranged in a square lattice. The tapered pyramid structure provides a smooth transition from the air to

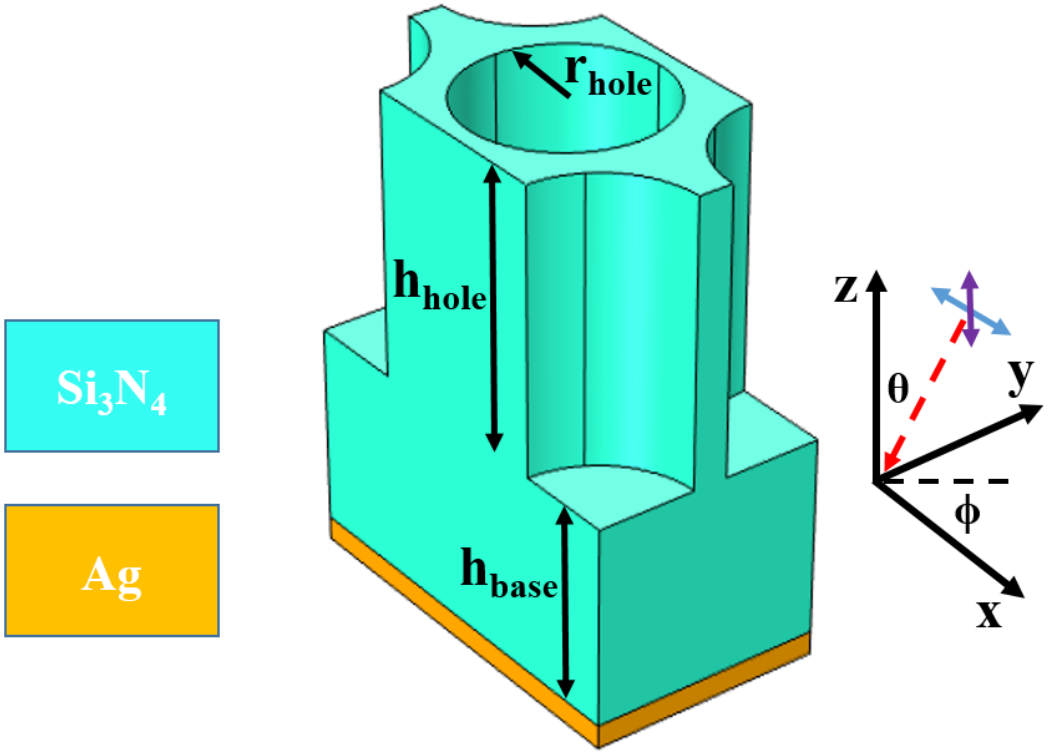


Figure 5.1: Schematic illustration of the $Si_3N_4$ photonic crystal unit cell and corresponding coordinate system for passive radiative cooling purpose. The direction of the incident electromagnetic wave is shown as the red arrow with spherical coordinate of polar angle $\theta$ and azimuthal angle $\phi$. The physical parameters are $h_{base}$ = 1 $\mu$m, $h_{hole}$ = 5 $\mu$m, $r_{hole}$ = 3.5 $\mu$m, and $period$ = 8 $\mu$m.

the bottom $Si_3N_4$ substrate. The working mechanism is similar to what we described in previous chapter about black silicon. A unit cell of the structure is shown in Figure 5.5. The final optimized structure has $period$ = 3.5 $\mu$m, $h_{base}$ = 10 $\mu$m and $h_{pyramid}$ = 6 $\mu$m. We can easily identify that the emissivity from 10 $\mu$m to 13 $\mu$m is close to unity for polar angle of 0 and 30 degrees and is regardless of azimuthal angle. A decrease occurs below 10 $\mu$m due to the decrease of the imaginary part of relative permittivity of $Si_3N_4$. This could be improved by increasing the thickness of the $Si_3N_4$ substrate. With increasing polar angle, the emissivity decreases beyond 10 $\mu$m while increases below 10 $\mu$m with an average higher than 0.9.

The third scheme we explored is a multilayer thin films structure called polymer-silica-mirror. It is based on silica and infrared absorptive polymer polydimethylsiloxane (PDMS), which is used in flexible optics (Kamali et al., 2016). We choose

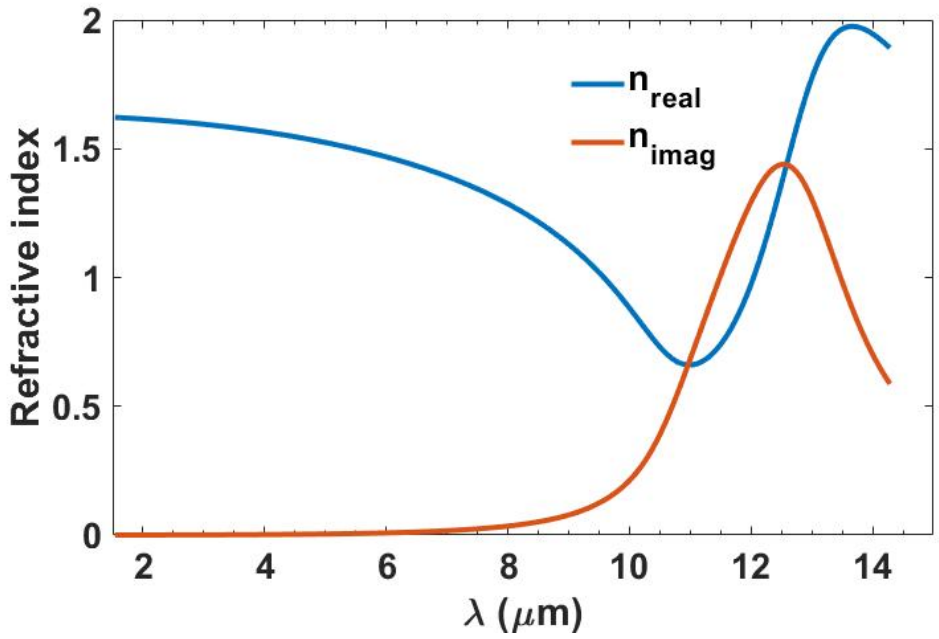


Figure 5.2: The real and imaginary part of the refractive index of $Si_3N_4$ with data adapted from (Kischkat et al., 2012).

these materials since it is mostly transparent in the visible and near infrared over the solar spectrum while absorptive in the mid-far-infrared. The refractive index of silica and PDMS is plotted in Figure 5.8 with data adapted from (Kischkat et al., 2012; Querry, 1987). The detailed structure of the multilayer stacks is shown as the inset of Figure 5.10.

The emissivity (or equivalently absorption) spectrum of multilayer structure can be calculated by transfer matrix method (Yariv and Yeh, 2006). Here, we employ the open source code $Openfilter$ for all the calculations. The results for two polarizations are plotted in Figure 5.9. In the mid-/far-infrared spectrum range beyond 5 $\mu$m, the emissivity remains at a value higher than 0.9 for normal direction except for a small dip (with emissivity of 0.85) around 13 $\mu$m. When the polar angle is 60 degrees, the emissivity beyond 5 $\mu$m is still higher than 0.8 for p-polarization and higher than 0.7 for s-polarization in most spectrum range. The emissivity in the solar spectrum is very low (0.03) due to the high transparency of silica and PDMS, as well as the high reflectivity of silver.

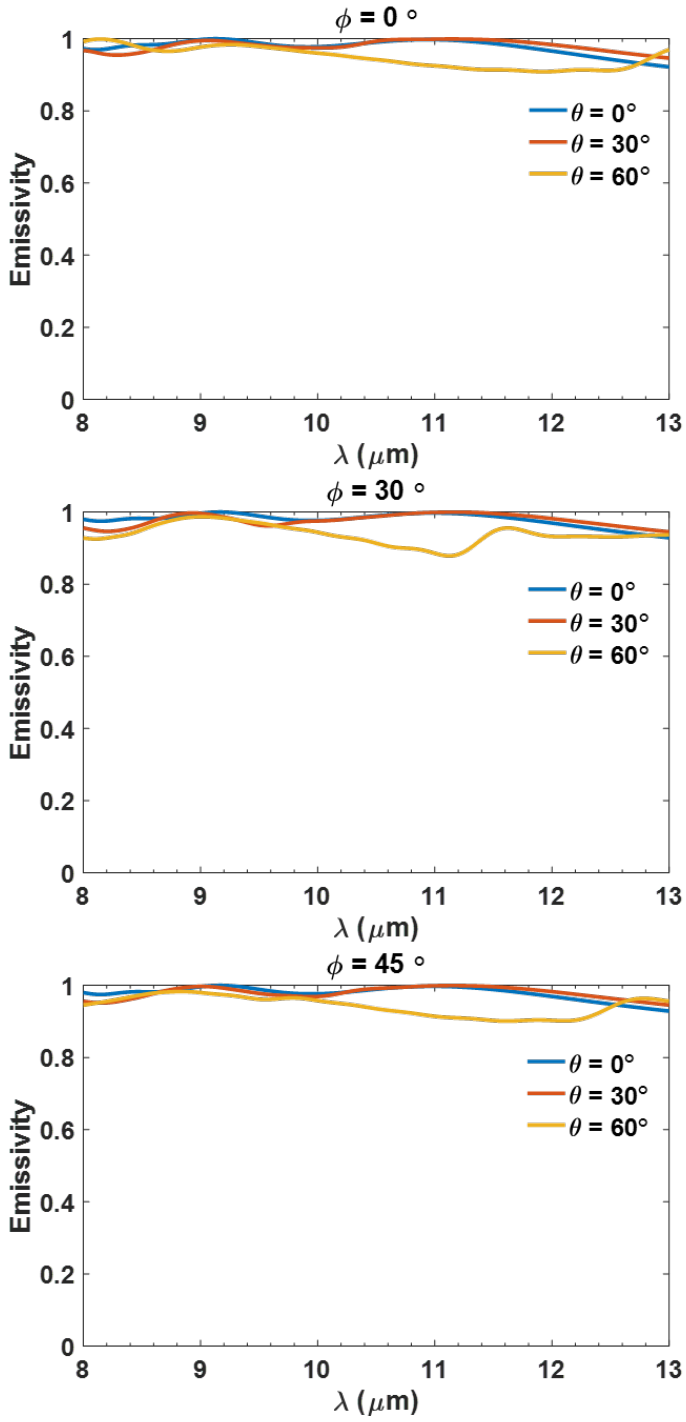


Figure 5.3: Emissivity spectrum of the $Si_3N_4$ photonic crystal for *s* polzrization under different combinations of $\theta$ and $\phi$.

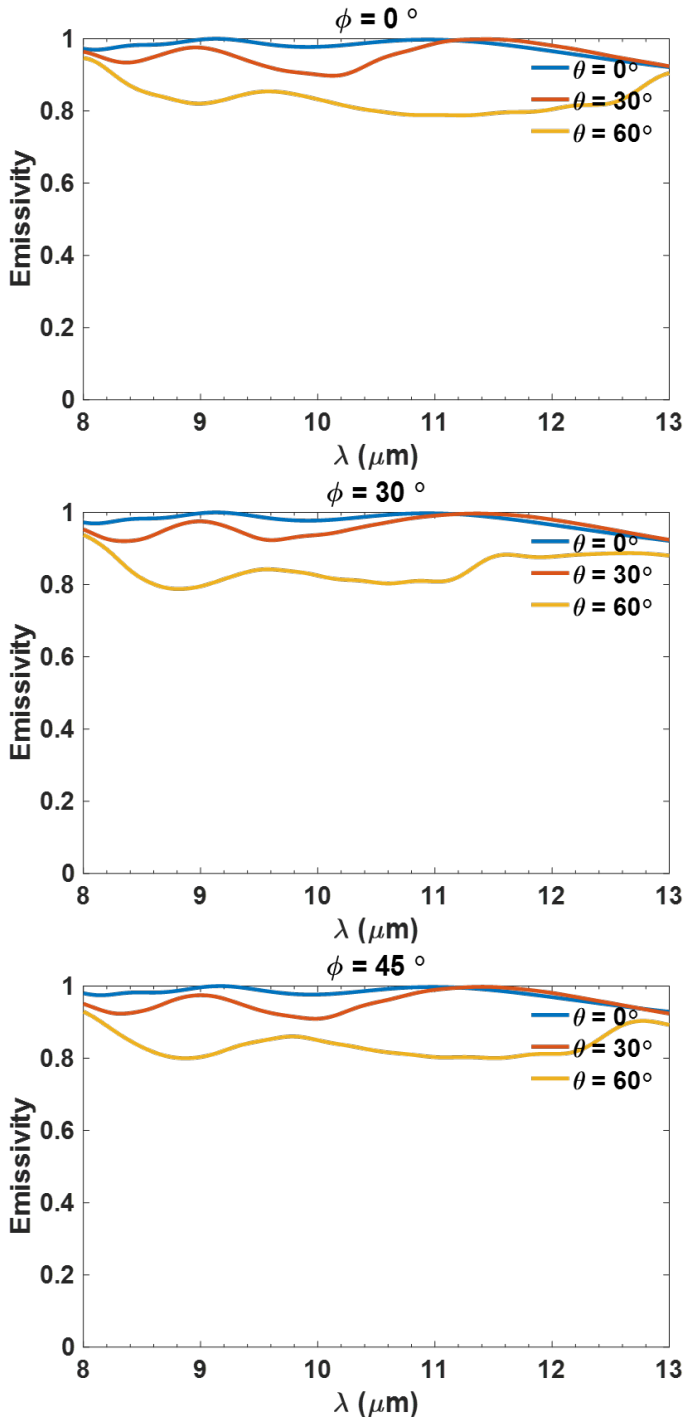


Figure 5.4: Emissivity spectrum of the $Si_3N_4$ photonic crystal for $p$ polzrization under different combinations of $\theta$ and $\phi$.

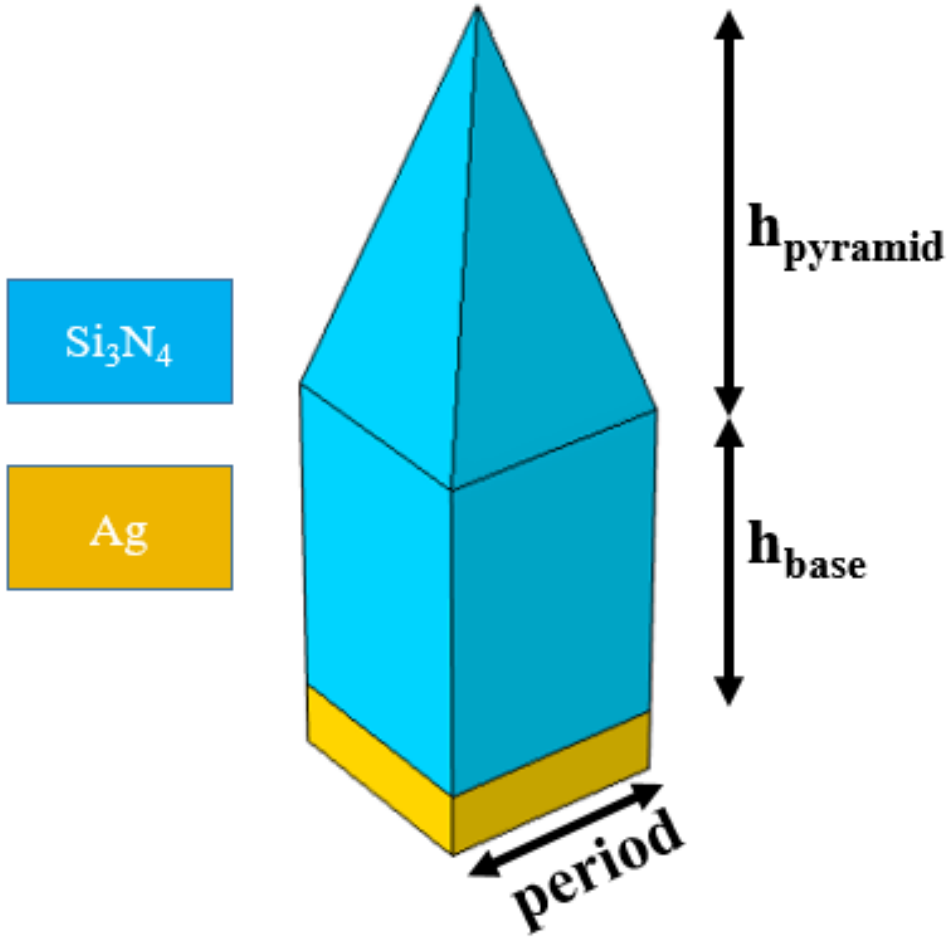


Figure 5.5: Schematic illustration of the unit cell of $Si_3N_4$ pyramid structure. The physical parameters are $h_{base}$ = 10 $\mu$m, $h_{pyramid}$ = 6 $\mu$m, and $period$ = 3.5 $\mu$m.

## 5.3 Experimental results

Here, we experimentally demonstrate passive radiative cooling under direct sunlight and at night using only a polymer-silica-mirror consisting of a fused silica wafer coated with a polymer top layer, and a silver back reflector as described in last section. This simple scheme achieves daytime cooling temperature differentials of 8.2 °C under direct sunlight and 8.4 °C at night, nearly 3 °C larger than that achieved by the nanophotonic structure in daytime. Our work demonstrates that inexpensive, bulk materials can be used for applications in energy such as dry cooling for power

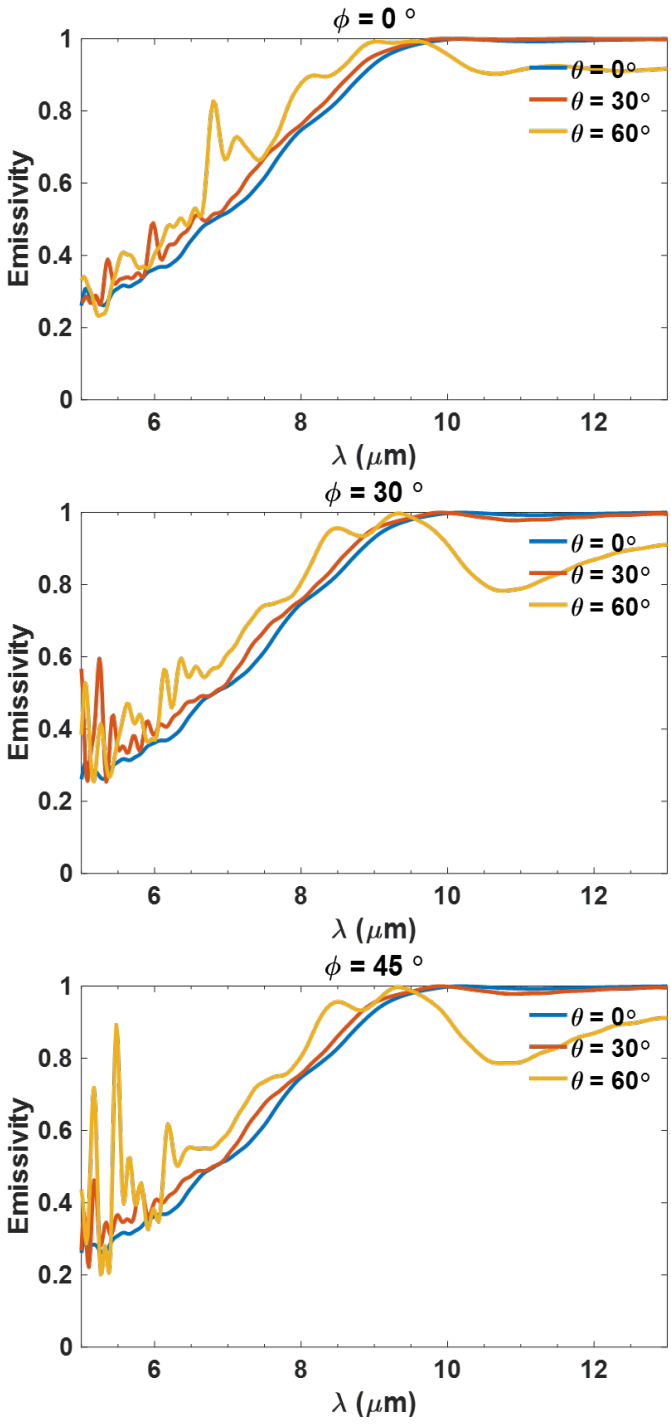


Figure 5.6: Emissivity spectrum of the $Si_3N_4$ pyramid for $s$ polzrization under different combinations of $\theta$ and $\phi$.

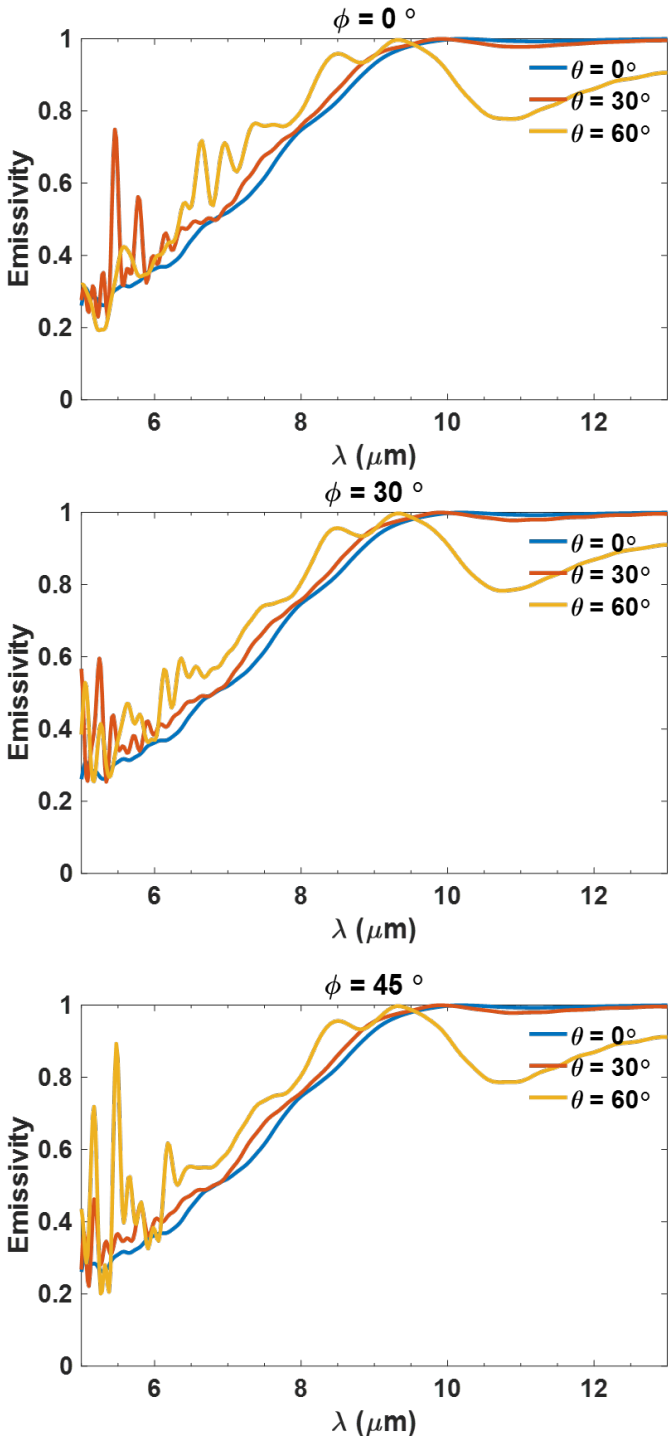


Figure 5.7: Emissivity spectrum of the $Si_3N_4$ pyramid for $p$ polzrization under different combinations of $\theta$ and $\phi$.

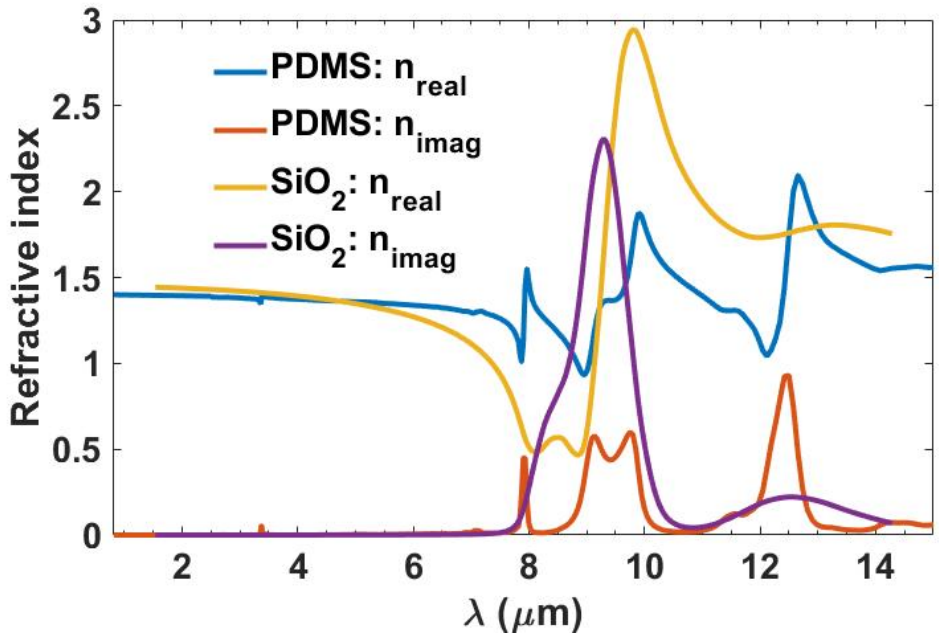


Figure 5.8: The real and imaginary part of the refractive index of silica and PDMS with data adapted from (Kischkat et al., 2012; Querry, 1987).

plants by realizing daytime radiative cooling without the need for complex photonic structures.

We experimentally examine the radiative cooling performance of the polymer-silica-mirror by coating a 4-inch fused silica wafer of 500 $\mu$m thickness with a 100-$\mu$m-thick PDMS film as a top layer and 120-nm-thick silver film as a back reflector. The performance of the device is tested on the roof of a building in Pasadena, California by exposing it to the sky. A picture of the setup and surroundings is shown in Figure 5.10a. To experimentally achieve cooling below ambient, special care needs to be taken in the measurement setup to reduce the parasitic conduction and convection from the ambient. In our measurement, the device is placed on a low thermal conductivity aerogel blanket which is attached to the inner side of a petri-dish. The petri-dish is supported by three glass rods to suspend it above the roof. The top of the petri-dish is covered by a polyethylene film, allowing solar irradiation to come in and infrared radiation to go out. The temperatures of the device and ambient air are recorded by K-type thermocouples.

The measured temperatures of the polymer-silica-mirror, silica-mirror without poly-

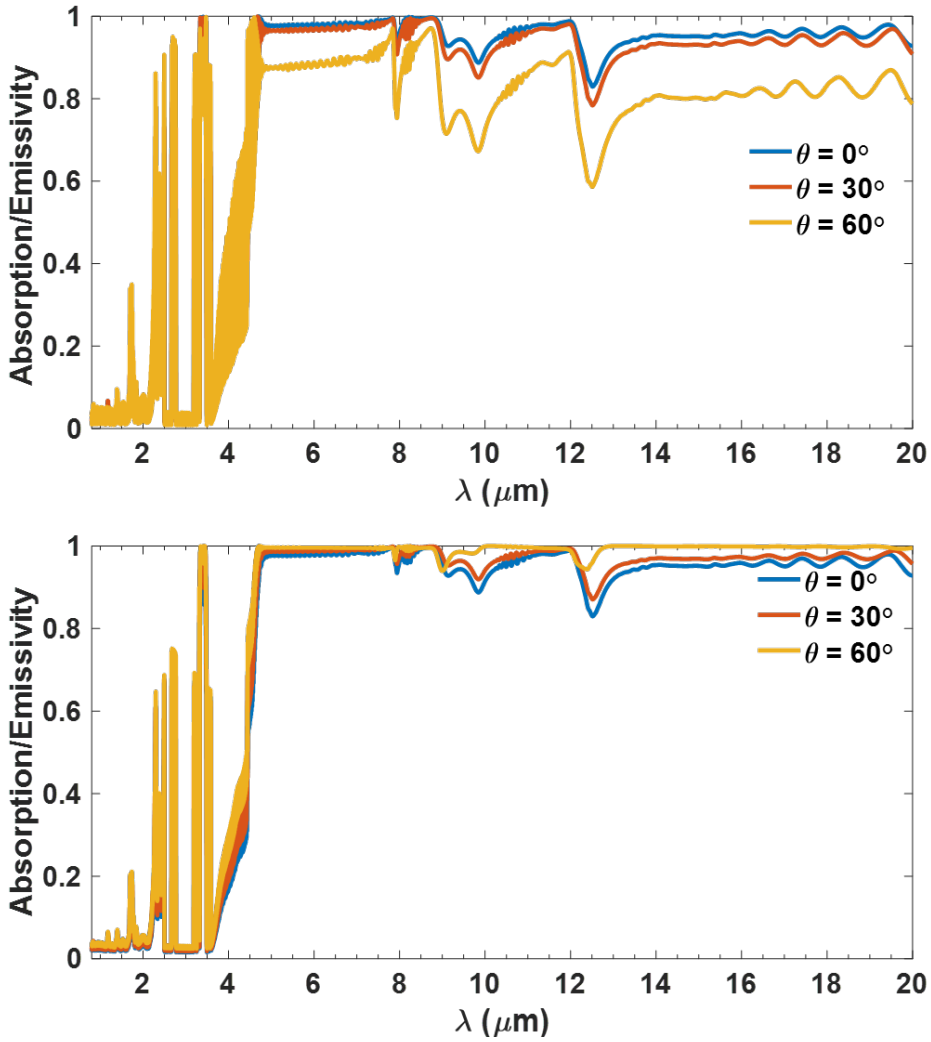


Figure 5.9: Calculated emissivity spectrum of the polymer-silica-mirror for *s* polarization (up) and *p* polarization (bottom).

mer coating and the ambient air are shown in Figure 2-2. The polymer-silica-mirror maintains a temperature that on average is 8.2 °C below the ambient air temperature throughout the period when it is exposed to the sun. At night, the device achieves 8.4 °C below ambient air temperature without sun irradiation. The daytime temperature drop is 1.0 °C lower than the silica-mirror and nearly 3 °C lower than that of the prior report (A. P. Raman et al., 2014). For comparison, we also include the field test results of a doped silicon wafer (resistivity of 8 - 12 Ω-cm) measured under the same conditions. Its temperature increases significantly after exposure to sunlight, reaching nearly 57 °C under the peak solar irradiation. Interestingly, the

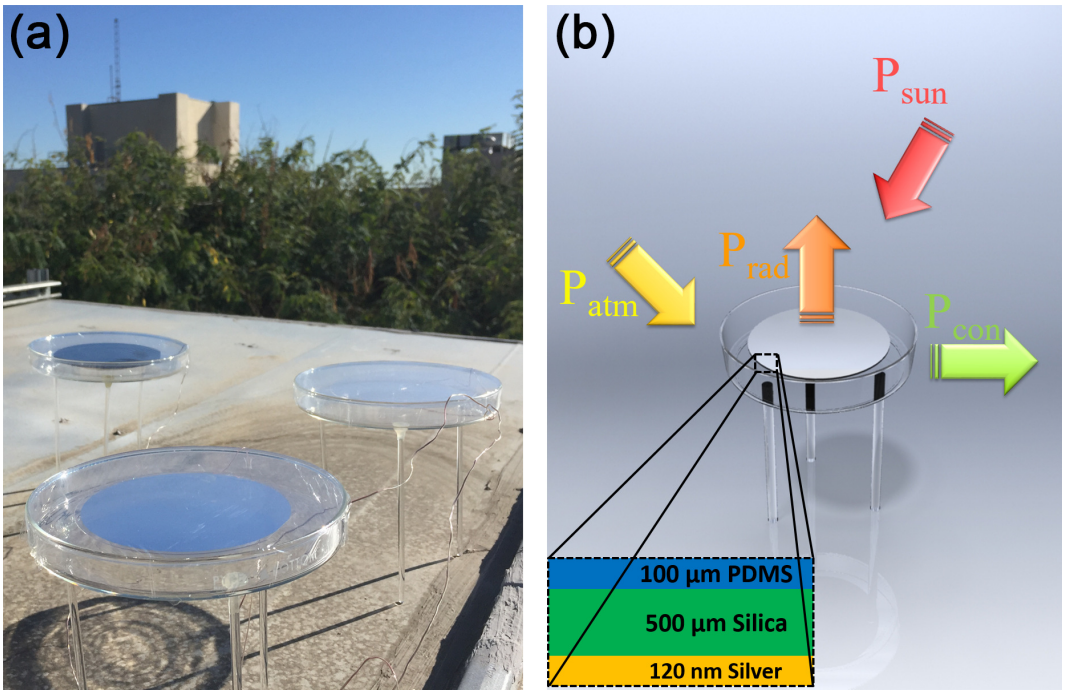


Figure 5.10: (a) Image of the samples under field test on the roof of a building in Pasadena, California. The device sits on top of an aerogel blankets attached to the bottom surface of a petri-dish with full access to the sky. The petri-dish is supported by three glass rods, suspending the petri-dish from the roof. The top of the petri-dish is covered by polyethylene film that allows solar irradiation to come in and infrared radiation to go out. (b) Schematic of the test setup. The input/output energy balance is labeled with $P_{rad}$, $P_{sun}$, $P_{atm}$, and $P_{con}$ denoting the radiated power from the cooler, absorpbed power from the sun, absorbed power from the atmosphere, and conduction/convection power loss, respectively.

doped silicon wafer also exhibits radiative cooling of about 5 °C below ambient air temperature after sunset, indicating the cooling ability of silicon solar cells. Here, the infrared absorption and emission is due to free carriers introduced by the doping.

To understand these observations, we measure the emissivity of the samples over the visible and infrared wavelength ranges using an ultraviolet/visible/near-infrared spectrometer and Fourier transform infrared spectroscopy (FTIR). The result is shown in Figure 5.12. Due to the transparency of fused silica and PDMS as well as the high reflectivity of silver from the visible to the near-infrared, the absorption for these wavelengths is minimal. However, a significant portion of the ultraviolet light is absorbed by the samples, resulting in about 23 $Wm^{-2}$ absorption power density for

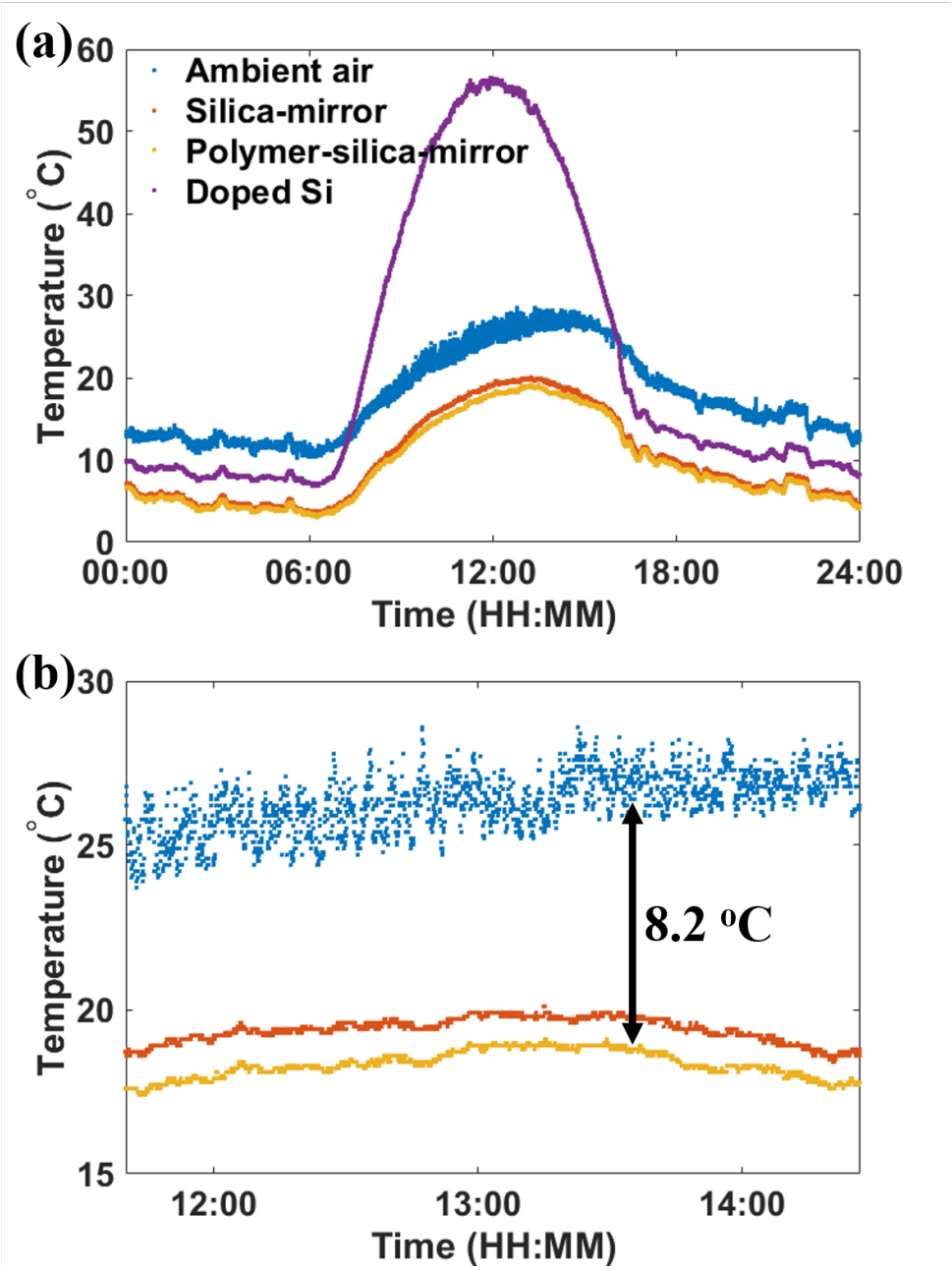


Figure 5.11: (a) Temperature measurement of the polymer-silica-mirror (orange), silica-mirror (red), ambient air temperature (blue), and bare doped silicon wafer (purple) during a 24-hour cycle. (b) Zoom-in of the temperature measurement when the device is under direct solar irradiation. The polymer-silica-mirror achieves a temperature that is 8.2 °C below ambient air temperature under these conditions.

the polymer-silica-mirror. The emissivity approaches unity for infrared wavelengths longer than 4.5 microns due to absorption of PDMS and silica. Counterintuitively, despite the fact that the sample has a high absorption outside the main atmospheric transparency window, we observe radiative cooling performance exceeding that of the nanophotonic cooler designed to emit only within the atmospheric transparency window of Raman et al (A. P. Raman et al., 2014).

## 5.4 Discussion

We investigate the origin of this observation by calculating the cooling performance of two additional cases with idealized emissivity profiles shown in Figure 5.12. For case 1, the emissivity is unity beyond 4.5 $\mu$m and zero otherwise, while for case 2 the emissivity is only unity in the main atmospheric transparency window.

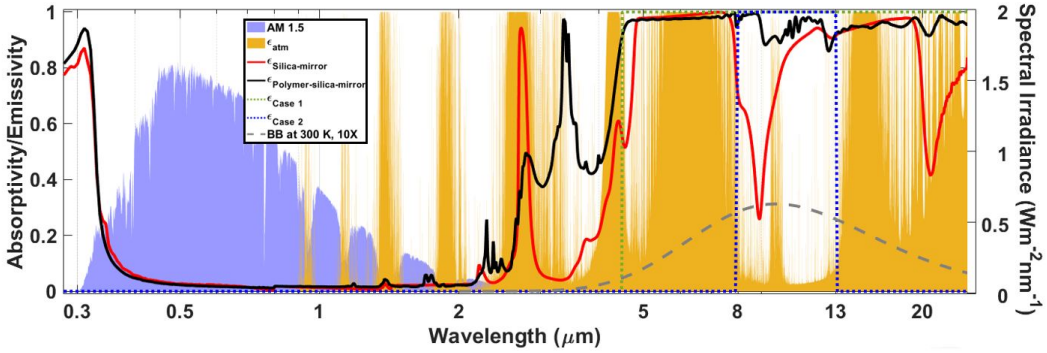


Figure 5.12: Measured emissivity of the polymer-silica-mirror (black solid line) and silica-mirror (red solid line) from ultraviolet to far infrared. Emissivity of two idealized cases: Case 1 (green dashed line) with unity emissivity beyond 4.5 $\mu$m and Case 2 (blue dashed line) with unity emissivity in the main atmospheric transparency window. The AM 1.5 solar spectrum, atmospheric absorption spectrum, and a blackbody radiation curve (grey dashed line) at 300 K are superimposed.

We begin by examining the radiative energy balance of the coolers under solar illumination. We take the cooler to be at temperature $T_{dev}$ and the ambient atmospheric temperature to be $T_{amb}$. The net cooling power density, defined as $P_{cool}$, is given by

$$P_{cool} = P_{rad}(T_{dev}) - P_{sun} - P_{atm}(T_{amb}) - P_{con}(T_{amb}, T_{dev}), \tag{5.1}$$

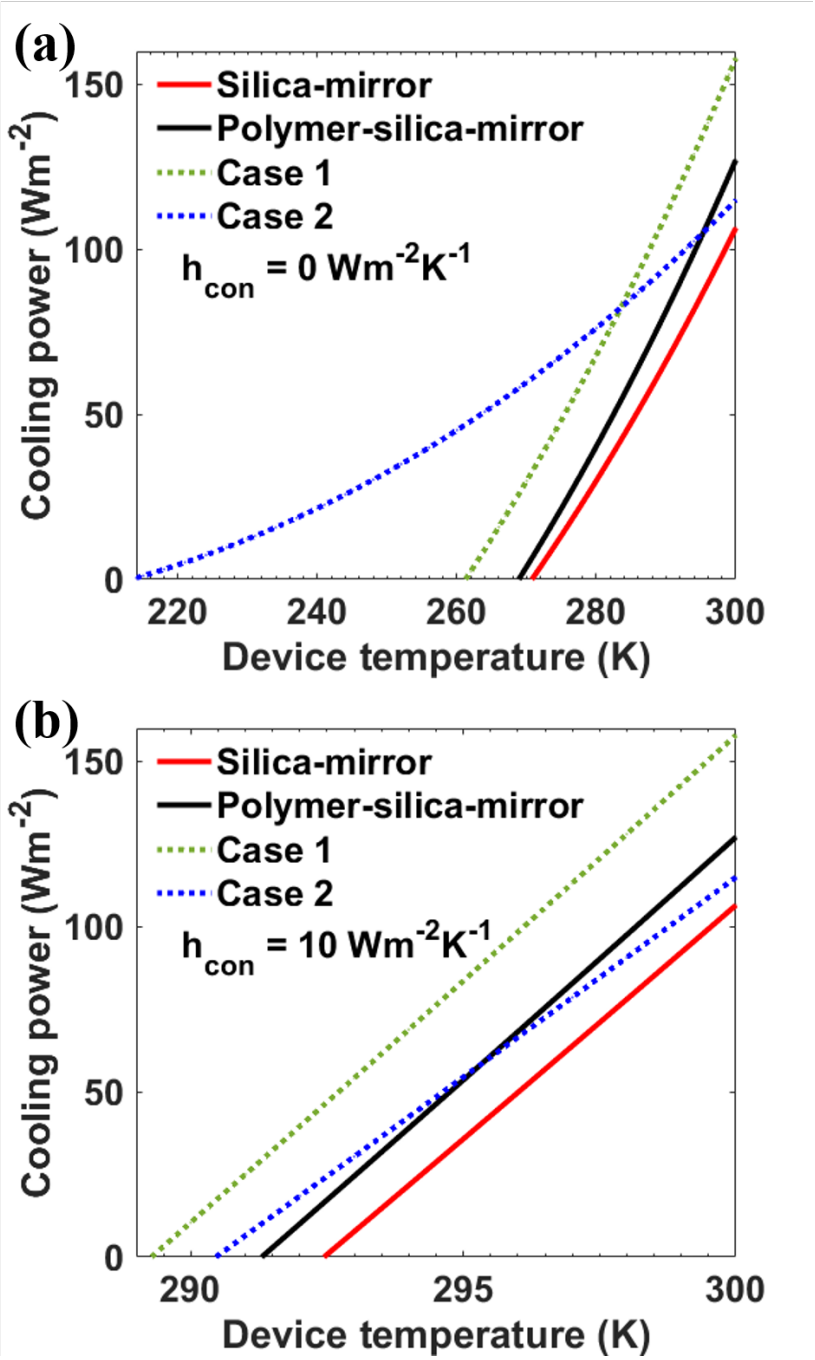


Figure 5.13: Net cooling power density of the polymer-silica-mirror, silica-mirror and the two idealized cases as a function of device temperature with different thermal coefficients (a) $h_{con} = 0$ and (b) $h_{con} = 10$ $Wm^{-2}K^{-1}$ under AM 1.5 illumination. The ambient temperature of the atmosphere is taken to be 300 K.

where $P_{rad}$ denotes the radiation power density of the device:

$$P_{rad}(T_{dev}) = \int d\Omega \cos(\theta) \int d\lambda I_{BB}(T_{dev}, \lambda)\epsilon_{dev}(\lambda, \theta) \tag{5.2}$$

with $I_{BB}$ indicating the spectral radiance of a blackbody. The absorbed power density by the device with surface facing the sun at angle $\Psi$ is given by

$$P_{sun} = \cos(\Psi) \int d\lambda \epsilon(\lambda, \Psi) I_{AM1.5}(\lambda). \tag{5.3}$$

$I_{AM1.5}$ is used as solar illumination intensity during daytime. The absorbed power density due to surrounding atmospheric thermal radiation is:

$$P_{atm}(T_{amb}) = \int d\Omega \cos(\theta) \int d\lambda I_{BB}(T_{amb}, \lambda)\epsilon_{dev}(\lambda, \theta)\epsilon_{atm}(\lambda, \theta). \tag{5.4}$$

The emissivity of the atmosphere is given by $\epsilon_{atm}(\lambda, \theta)$ (*IR Transmission Spectra, Gemini Observatory Kernel Description* n.d.). The last term from Equation (1) is the power density of thermal conduction and convection parasitically transferred to the cooler:

$$P_{con}(T_{amb}, T_{dev}) = h_{con}(T_{amb} - T_{dev}), \tag{5.5}$$

where $h_{con}$ is the thermal coefficient. Experimentally, the thermal coefficient is determined by heating up a 4-inch Si wafer and measuring the transient temperature of the wafer in the same petri-dish used for the radiative cooler. For this measurement, we maximize the influence of parasitic conduction and convection by coating the wafer with silver on both polished sides, thereby minimizing radiative losses. Fitting the transient temperature using a lumped capacitance analysis yields the thermal coefficient as around 10 $Wm^{-2}K^{-1}$.

We present the net cooling power density as a function of device temperature without and with the influence of parasitic convection and conduction in Figures 5.13a and b, respectively. The figure shows that Case 1, which emits outside the primary atmospheric transparency window and thus parasitically absorbs radiation from the atmosphere, has a larger cooling power density than Case 2 for cooler temperatures above 283 K. While the absorbed atmospheric radiation increases for Case 1, the power radiated outward increases by a larger amount. Thus, expanding the spectral range of high emissivity can be beneficial under some circumstances (Huang and Ruan, 2017; Z. Chen et al., 2016). For a cooler temperature of 300 K, Case 1 achieves a cooling power density 158 $Wm^{-2}$, 43 $Wm^{-2}$ higher than Case 2.

On the other hand, if the goal is to achieve cooling temperature substantially below ambient temperature, Case 2 is better due to its small absorption from the atmosphere (Huang and Ruan, 2017). Achieving such low temperatures requires high vacuum to minimize parasitic conduction and convection (Z. Chen et al., 2016). If such parasitic mechanisms are present, expanding the bandwidth of thermal emission is likely to be beneficial despite the increase in sky radiation absorption as shown in Figure 5.13b.

The above discussion shows why the polymer-silica-mirror achieves such good performance despite absorbing atmospheric radiation. Due to convection and conduction, the steady-state temperature only minimally differs from that of the atmosphere, thus decreasing the influence of the atmospheric radiation and making the near-unity emissivity over a broad bandwidth beneficial. The result is a net cooling power density of 127 $Wm^{-2}$ at ambient temperature of 300 K under AM 1.5 solar irradiation, 20 $Wm^{-2}$ higher than the silica-mirror and more than twice of that achieved by the nanophotonic structure (A. P. Raman et al., 2014). The predicted steady-state temperature at zero net cooling power using the measured $h_{con}$ = 10 $Wm^{-2}K^{-1}$ is 8.7 °C below ambient under direct sunlight, in good agreement with our measurement.

## 5.5 Conclusions

In summary, we have shown that abundant materials with strong infrared emission over a broad bandwidth such as fused silica and PDMS are capable of radiative cooling with performance exceeding that of more complex nanophotonic structures. For applications in which the desired temperature is not substantially different from ambient temperature, a radiative cooler with near unity emissivity over a broad infrared spectrum will achieve better performance than one that emits only in the atmospheric window. The presented radiative cooler can be easily realized with common bulk materials such as fused silica wafers with a metallic back reflector. Further improvements in the present cooler can be achieved if structure can be designed to reduce sunlight absorption in the ultraviolet. Our work advances the application of passive radiative cooling for applications such as dry cooling of power plants.

*Chapter 6*

# SUMMARY AND OUTLOOK

In this work, we have intensively studied methods to tailor the thermal radiation from near field to far field, both theoretically and experimentally. We summarize our key achievements and point out the direction for future explorations that could expand the scientific scope and application areas.

## 6.1 Near field radiative heat control

Firstly, works are focused on dynamic control of near field radiative heat transfer with electrically and optically modifying the carrier density inside porous silicon slabs. Results show that the tuning range of the electrical method is not large enough due to the limited breakdown electric field of the material and the width of the depletion region. Possible solutions could potentially be found by resolving to two dimensional materials such as graphene, h-BN with pattern structures, or conducting oxide such as indium tin oxide (ITO). Though the optical method provides a potential solution for large tuning range, its real application is limited due to its high input power density and requires complex optical setup and control. Possible solutions could also be two-dimensional materials by incorporating field resonant structure (Brar et al., 2015). Furthermore, liquid crystal is famous for its tuning properties under external electric field with a large change of refractive index and a response time on the order of ms to $\mu$s (D.-K. Yang, 2014; Meyer et al., 1975). Various switch techniques, such as in-plane switching, vertical alignment, and twisted nematic have been commercialized. A method to incorporate this fascinating material into near field radiative heat control would be of great interest.

## 6.2 Spectrally selective absorber and far field emitter

Secondly, we applied photonic design on semiconductors and experimentally demonstrated two different schemes of spectrally selective absorbers. Scalability of the germanium photonic crystal structure remains a big obstacle in field applications, mainly due to the nano-scale feature size. An initial small-scale test maybe realized by deep-UV lithography for wafer scale fabrication. On the other hand, the mid-/far-infrared spectral properties of the black silicon need further investigation. Structural, doping and etching method will potentially affect the results. Further tests could be performed with both concentrated and non-concentrated solar simulators. In addition, we could extend the design from broad band to narrow band and realized useful thermal emitters in the infrared (Xianliang Liu et al., 2011; Inoue T and S., 2015). A possible design is schematically shown in Figure 6.1. The thermal emitter is achieved by resistive heating the intra-cavity which is a plasmonic cavity that ensures narrow band emission. The metal caps can simultaneously work as the electrodes for thermal resistive heating of the cavity. With careful engineering design and fabrication methods, the emitter will be able to generate desired mid-/far-infrared emission in far field.

## 6.3 Passive radiative cooling

Thirdly, through the dedicated photonic design and fabrication consideration, we achieved record low temperature below ambient with passive radiative cooling under direct sunlight and normal atmospheric conditions. More design and fabrication study can be done with $Si_3N_4$, $Al_2O_3$ particles or porous structures (Zhai et al., 2017; Hsu, A. Y. Song, et al., 2016; Cai, Peng, et al., 2019). Improvement can be done to increase the reflection in the UV region by using UV transparent materials such as $CaF_2$, $MgF_2$ and fused silica. Further tests could be done by combining the radiative cooler with condenser to construct a cooling system for in-house cooling purpose (Goldstein, A. P. Raman, and Fan, 2017). Large scale applications could be realized by cutting down the cost of cooling in places like train stations, airports, and public libraries. Even larger scale deployment could be used to alleviate urban heat island effect or compensate the extra heat due to the $CO_2$-based global warming. Other directions include developing new structures and fabrication methods for achieving

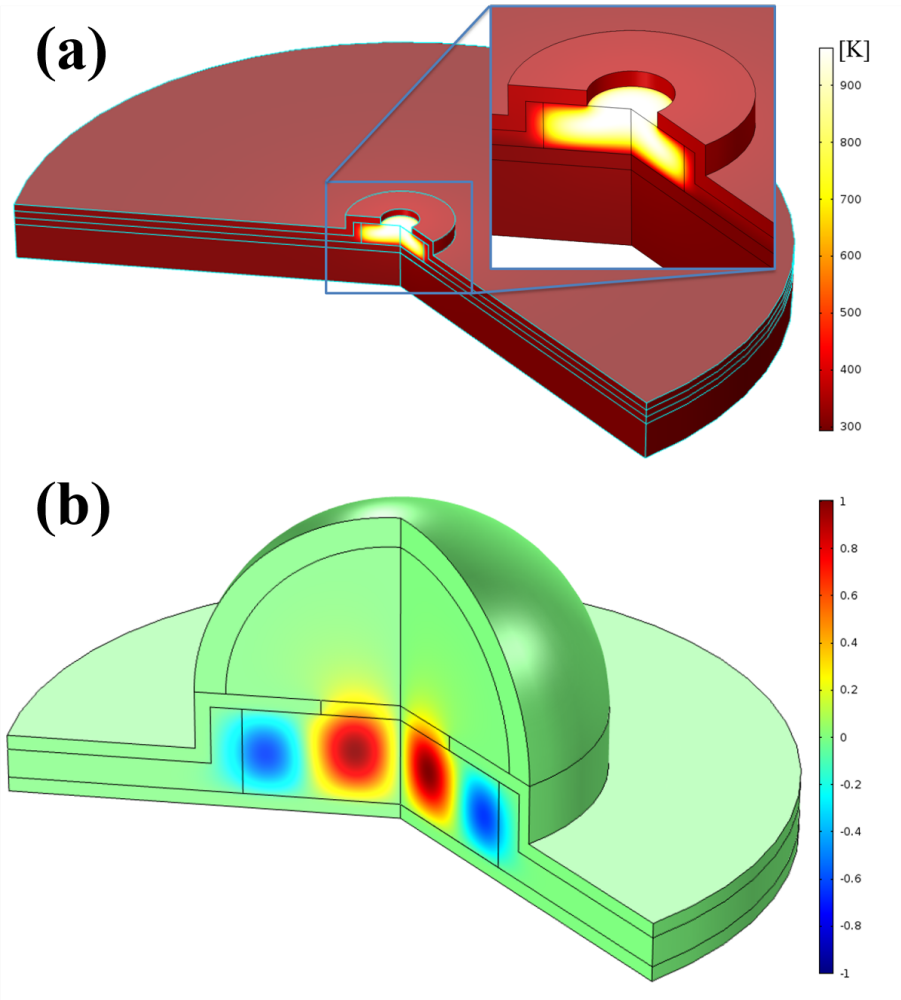


Figure 6.1: (a) Temperature and (b) relative field distribution of the proposed thermal emitter.

radiative cooling for solar cells, cooling objects while preserving their original color (L. Zhu, A. Raman, and Fan, 2013; L. Zhu, A. Raman, K. X. Wang, et al., 2014).

# BIBLIOGRAPHY

Abbott, Derek (2010). "Keeping the energy debate clean: How do we supply the world's energy needs?" In: *Proceedings of the IEEE* 98.1, pp. 42–66.

Arpin, Kevin A et al. (2013). "Three-dimensional self-assembled photonic crystals with high temperature stability for thermal emission modification". In: *Nature Communications* 4, p. 2630.

Bao, Hua et al. (2017). "Double-layer nanoparticle-based coatings for efficient terrestrial radiative cooling". In: *Solar Energy Materials and Solar Cells* 168, pp. 78–84.

Bard, Allen J and Marye Anne Fox (1995). "Artificial photosynthesis: solar splitting of water to hydrogen and oxygen". In: *Accounts of Chemical Research* 28.3, pp. 141–145.

Barshilia, Harish C et al. (2009). "Optical properties and thermal stability of pulsed-sputter-deposited AlxOy/Al/AlxOy multilayer absorber coatings". In: *Solar Energy Materials and Solar Cells* 93.3, pp. 315–323.

Basu, S, Y-B Chen, and ZM Zhang (2007). "Microscale radiation in thermophotovoltaic devices—a review". In: *International Journal of Energy Research* 31.6-7, pp. 689–716.

Basu, S, BJ Lee, and ZM Zhang (2010). "Near-field radiation calculated with an improved dielectric function model for doped silicon". In: *Journal of Heat Transfer* 132.2, p. 023301.

Basu, S, Bong Jae Lee, and ZM Zhang (2010). "Infrared radiative properties of heavily doped silicon at room temperature". In: *Journal of Heat Transfer* 132.2, p. 023301.

Basu, Soumyadipta and Mathieu Francoeur (2011). "Near-field radiative transfer based thermal rectification using doped silicon". In: *Applied Physics Letters* 98.11, p. 113106.

Bermel, Peter et al. (2010). "Design and global optimization of high-efficiency thermophotovoltaic systems". In: *Optics Express* 18.103, A314–A334.

Bierman, David M et al. (2016). "Enhanced photovoltaic energy conversion using thermally based spectral shaping". In: *Nature Energy* 1, p. 16068.

Brar, Victor W et al. (2015). "Electronic modulation of infrared radiation in graphene plasmonic resonators". In: *Nature Communications* 6, p. 7032.

Cai, Lili, Yucan Peng, et al. (2019). "Temperature Regulation in Colored Infrared-Transparent Polyethylene Textiles". In: *Joule*.

Cai, Lili, Alex Y Song, et al. (2018). “Spectrally selective nanocomposite textile for outdoor personal cooling”. In: *Advanced Materials* 30.35, p. 1802152.

Cao, Feng, Daniel Kraemer, et al. (2015). “Enhanced Thermal Stability of W-Ni-Al2O3 Cermet-Based Spectrally Selective Solar Absorbers with Tungsten Infrared Reflectors”. In: *Advanced Energy Materials* 5.2.

Cao, Feng, Kenneth McEnaney, et al. (2014). “A review of cermet-based spectrally selective solar absorbers”. In: *Energy & Environmental Science* 7.5, pp. 1615–1627.

Carslaw, Horatio Scott and John Conrad Jaeger (1959). “Conduction of heat in solids”. In: *Oxford: Clarendon Press, 1959, 2nd ed.*

Catalanotti, S et al. (1975). “The radiative cooling of selective surfaces”. In: *Solar Energy* 17.2, pp. 83–89.

Celanovic, Ivan, Natalija Jovanovic, and John Kassakian (2008). “Two-dimensional tungsten photonic crystals as selective thermal emitters”. In: *Applied Physics Letters* 92.19, p. 193101.

Chang, CW et al. (2006). “Solid-state thermal rectifier”. In: *Science* 314.5802, pp. 1121–1124.

Chen, Kaifeng, Parthiban Santhanam, and Shanhui Fan (2015). “Suppressing sub-bandgap phonon-polariton heat transfer in near-field thermophotovoltaic devices for waste heat recovery”. In: *Applied Physics Letters* 107.9, p. 091106.

Chen, Kaifeng, Parthiban Santhanam, Sunil Sandhu, et al. (2015). “Heat-flux control and solid-state cooling by regulating chemical potential of photons in near-field electromagnetic heat transfer”. In: *Physical Review B* 91.13, p. 134301.

Chen, Y-B and ZM Zhang (2007). “Design of tungsten complex gratings for thermophotovoltaic radiators”. In: *Optics Communications* 269.2, pp. 411–417.

Chen, Zhen et al. (2016). “Radiative cooling to deep sub-freezing temperatures through a 24-h day–night cycle”. In: *Nature Communications* 7, p. 13729.

Chuang, Shun Lien (2012). *Physics of photonic devices*. Vol. 80. John Wiley & Sons.

Cravalho, E, G Domoto, and C Tien (1968). “Measurements of thermal radiation of solids at liquid-helium temperatures”. In: *3rd Thermophysics Conference*, p. 774.

Cravalho, Ernest G, Chang L Tien, and RP Caren (1967). “Effect of small spacings on radiative transfer between two dielectrics”. In: *Journal of Heat Transfer* 89.4, pp. 351–358.

Cui, Longji et al. (2017). “Study of radiative heat transfer in Ångström-and nanometre-sized gaps”. In: *Nature Communications* 8, p. 14479.

Cui, Yi et al. (2019). *Infrared-transparent porous polymer textile for human body cooling and heating*. US Patent App. 16/066,247.

De Zoysa, Menaka et al. (2012). "Conversion of broadband to narrowband thermal emission through energy recycling". In: *Nature Photonics* 6.8, pp. 535–539.

Diatezua, Deda M et al. (1996). "Silicon oxynitride multilayers as spectrally selective material for passive radiative cooling applications". In: *Solar Energy Materials and Solar Cells* 40.3, pp. 253–259.

Diatezua, MD, PA Thiry, and R Caudano (1995). "Characterization of silicon oxynitride multilayered systems for passive radiative cooling application". In: *Vacuum* 46.8-10, pp. 1121–1124.

Ding, Ding, Taeyong Kim, and Austin J Minnich (2016). "Active thermal extraction of near-field thermal radiation". In: *Physical Review B* 93.8, p. 081402.

Donnadieu, A and BO Seraphin (1978). "Optical performance of absorber-reflector combinations for photothermal solar energy conversion". In: *JOSA* 68.3, pp. 292–297.

Dunkelberger, Adam D et al. (2018). "Active tuning of surface phonon polariton resonances via carrier photoinjection". In: *Nature Photonics* 12.1, p. 50.

Eriksson, TS, EM Lushiku, and CG Granqvist (1984). "Materials for radiative cooling to low temperature". In: *Solar Energy Materials* 11.3, pp. 149–161.

Fiorino, Anthony, Dakotah Thompson, et al. (2018). "Giant enhancement in radiative heat transfer in sub-30 nm gaps of plane parallel surfaces". In: *Nano Letters* 18.6, pp. 3711–3715.

Fiorino, Anthony, Linxiao Zhu, et al. (2018). "Nanogap near-field thermophotovoltaics". In: *Nature Nanotechnology* 13.9, p. 806.

Garnett, JC Maxwell (1905). "Colours in metal glasses, in metallic films and in metallic solutions.—II". In: *Proc. R. Soc. Lond. A* 76.511, pp. 370–373.

St-Gelais, Raphael et al. (2016). "Near-field radiative heat transfer between parallel structures in the deep subwavelength regime". In: *Nature Nanotechnology* 11.6, p. 515.

Gentle, Angus R and Geoffrey B Smith (2010). "Radiative heat pumping from the earth using surface phonon resonant nanoparticles". In: *Nano Letters* 10.2, pp. 373–379.

Gentle, AR, JLC Aguilar, and GB Smith (2011). "Optimized cool roofs: Integrating albedo and thermal emittance with R-value". In: *Solar Energy Materials and Solar Cells* 95.12, pp. 3207–3215.

Goldstein, Eli A, Aaswath P Raman, and Shanhui Fan (2017). "Sub-ambient non-evaporative fluid cooling with the sky". In: *Nature Energy* 2.9, p. 17143.

Granqvist, CG and A Hjortsberg (1980). “Surfaces for radiative cooling: Silicon monoxide films on aluminum”. In: *Applied Physics Letters* 36.2, pp. 139–141.

Granqvist, CG, A Hjortsberg, and TS Eriksson (1982). “Radiative cooling to low temperatures with selectivity IR-emitting surfaces”. In: *Thin Solid Films* 90.2, pp. 187–190.

Green, Martin A et al. (2011). “Solar cell efficiency tables (version 37)”. In: *Progress in Photovoltaics: Research and Applications* 19.1, pp. 84–92.

Greffet, Jean-Jacques et al. (2002). “Coherent emission of light by thermal sources”. In: *Nature* 416.6876, pp. 61–64.

Guo, Peijun et al. (2016). “Ultrafast switching of tunable infrared plasmons in indium tin oxide nanorod arrays with large absolute amplitude”. In: *Nature Photonics* 10.4, p. 267.

Hargreaves, CM (1969). “Anomalous radiative transfer between closely-spaced bodies”. In: *Physics Letters A* 30.9, pp. 491–492.

Head, AK (1959). “Method and means for refrigeration by selective radiation”. In: *Australian Patent* 239364.

Hildenbrand, Jürgen et al. (2010). “Micromachined mid-infrared emitter for fast transient temperature operation for optical gas sensing systems”. In: *IEEE Sensors Journal* 10.2, pp. 353–362.

Hossain, Md Muntasir, Baohua Jia, and Min Gu (2015). “A metamaterial emitter for highly efficient radiative cooling”. In: *Advanced Optical Materials* 3.8, pp. 1047–1051.

Hsu, Po-Chun, Chong Liu, et al. (2017). “A dual-mode textile for human body radiative heating and cooling”. In: *Science Advances* 3.11, e1700895.

Hsu, Po-Chun, Alex Y Song, et al. (2016). “Radiative human body cooling by nanoporous polyethylene textile”. In: *Science* 353.6303, pp. 1019–1023.

Hu, Lu et al. (2008). “Near-field thermal radiation between two closely spaced glass plates exceeding Planck’s blackbody radiation law”. In: *Applied Physics Letters* 92.13, p. 133106.

Huang, Zhifeng and Xiulin Ruan (2017). “Nanoparticle embedded double-layer coating for daytime radiative cooling”. In: *International Journal of Heat and Mass Transfer* 104, pp. 890–896.

Huldt, L (1971). “Band-to-band Auger recombination in indirect gap semiconductors”. In: *Physica Status Solidi (a)* 8.1, pp. 173–187.

Ihlefeld, Jon F et al. (2015). “Room-temperature voltage tunable phonon thermal conductivity via reconfigurable interfaces in ferroelectric thin films”. In: *Nano Letters* 15.3, pp. 1791–1795.

Ilic, Ognjen, Peter Bermel, et al. (2016). “Tailoring high-temperature radiation and the resurrection of the incandescent source”. In: *Nature Nanotechnology* 11.4, pp. 320–324.

Ilic, Ognjen, Marinko Jablan, et al. (2012). “Near-field thermal radiation transfer controlled by plasmons in graphene”. In: *Physical Review B* 85.15, p. 155422.

Ilic, Ognjen, Nathan H Thomas, et al. (2018). “Active Radiative Thermal Switching with Graphene Plasmon Resonators”. In: *ACS Nano* 12.3, pp. 2474–2481.

Inoue T De Zoysa M, Asano T. and Noda S. (2015). “Realization of narrowband thermal emission with optical nanostructures”. In: *Optica* 2.1, pp. 27–35.

Inoue, Takuya, Menaka De Zoysa, et al. (2014). “Realization of dynamic thermal emission control”. In: *Nature Materials* 13.10, pp. 928–931.

Inoue, Takuya, Kohei Watanabe, et al. (2018). “Near-field thermophotovoltaic energy conversion using an intermediate transparent substrate”. In: *Optics Express* 26.2, A192–A208.

*IR Transmission Spectra, Gemini Observatory Kernel Description*. `http://www.gemini.edu/?q=node/10789`. accessed Nov. 20, 2016.

Ito, Kota et al. (2017). “Dynamic modulation of radiative heat transfer beyond the blackbody limit”. In: *Nano Letters* 17.7, pp. 4347–4353.

Jeong, Wonho et al. (2015). “Scanning probe microscopy for thermal transport measurements”. In: *Nanoscale and Microscale Thermophysical Engineering* 19.4, pp. 279–302.

Kamali, Seyedeh Mahsa et al. (2016). “Decoupling optical function and geometrical form using conformal flexible dielectric metasurfaces”. In: *Nature Communications* 7, p. 11618.

Karalis, Aristeidis and John D Joannopoulos (2016). “‘Squeezing’near-field thermal emission for ultra-efficient high-power thermophotovoltaic conversion”. In: *Scientific Reports* 6, p. 28472.

Kats, Mikhail A et al. (2013). “Vanadium dioxide as a natural disordered metamaterial: perfect thermal emission and large broadband negative differential thermal emittance”. In: *Physical Review X* 3.4, p. 041004.

Kecebas, Muhammed Ali et al. (2017). “Passive radiative cooling design with broadband optical thin-film filters”. In: *Journal of Quantitative Spectroscopy and Radiative Transfer* 198, pp. 179–186.

Kennedy, Cheryl E (2002). *Review of mid-to high-temperature solar selective absorber materials*. Tech. rep. National Renewable Energy Lab., Golden, CO.(US).

Kim, Kyeongtae et al. (2015). “Radiative heat transfer in the extreme near field”. In: *Nature* 528.7582, p. 387.

Kimball, BA (1985). “Cooling performance and efficiency of night sky radiators”. In: *Solar Energy* 34.1, pp. 19–33.

Kinsey, N et al. (2015). “Epsilon-near-zero Al-doped ZnO for ultrafast switching at telecom wavelengths”. In: *Optica* 2.7, pp. 616–622.

Kischkat, Jan et al. (2012). “Mid-infrared optical properties of thin films of aluminum oxide, titanium dioxide, silicon dioxide, aluminum nitride, and silicon nitride”. In: *Applied Optics* 51.28, pp. 6789–6798.

Kraemer, Daniel et al. (2011). “High-performance flat-panel solar thermoelectric generators with high thermal concentration”. In: *Nature Materials* 10.7, p. 532.

Krueger, Neil A et al. (2016). “Porous Silicon Gradient Refractive Index Micro-Optics”. In: *Nano Letters* 16.12, pp. 7402–7407.

Kussmaul, Michael, Michael J Mirtich, and Arthur Curren (1992). “Ion beam treatment of potential space materials at the NASA Lewis Research Center”. In: *Surface and Coatings Technology* 51.1-3, pp. 299–306.

Lampert, Carl M (1979). “Coatings for enhanced photothermal energy collection I. Selective absorbers”. In: *Solar Energy Materials* 1.5-6, pp. 319–341.

Laroche, Marine, Rémi Carminati, and Jean-Jacques Greffet (2006). “Near-field thermophotovoltaic energy conversion”. In: *Journal of Applied Physics* 100.6, p. 063704.

Lau, Japheth Z-J and Basil T Wong (2017). “Thermal energy conversion using near-field thermophotovoltaic device composed of a thin-film tungsten radiator and a thin-film silicon cell”. In: *Journal of Applied Physics* 122.8, p. 084302.

Lenert, Andrej et al. (2014). “A nanophotonic solar thermophotovoltaic device”. In: *Nature Nanotechnology* 9.2, p. 126.

Li, Pengfei et al. (2015). “Large-Scale Nanophotonic Solar Selective Absorbers for High-Efficiency Solar Thermal Energy Conversion”. In: *Advanced Materials* 27.31, pp. 4585–4591.

Li, Xiao-Fan et al. (2007). “High solar absorption of a multilayered thin film structure”. In: *Optics Express* 15.4, pp. 1907–1912.

Lin, Shawn-Yu, JG Fleming, and I El-Kady (2003). “Three-dimensional photonic-crystal emission through thermal excitation”. In: *Optics Letters* 28.20, pp. 1909–1911.

Lin, Shawn-Yu, J Moreno, and JG Fleming (2003). “Three-dimensional photonic-crystal emitter for thermal photovoltaic power generation”. In: *Applied Physics Letters* 83.2, pp. 380–382.

Liu, Xianliang et al. (2011). “Taming the blackbody with infrared metamaterials as selective thermal emitters”. In: *Physical Review Letters* 107.4, p. 045901.

Liu, Xinyu and Willie J Padilla (2017). "Reconfigurable room temperature metamaterial infrared emitter". In: *Optica* 4.4, pp. 430–433.

Ma, Rujun et al. (2017). "Highly efficient electrocaloric cooling with electrostatic actuation". In: *Science* 357.6356, pp. 1130–1134.

Maier, Stefan Alexander (2007). *Plasmonics: fundamentals and applications*. Springer Science & Business Media.

Messina, Riccardo and Philippe Ben-Abdallah (2013). "Graphene-based photovoltaic cells for near-field thermal energy conversion". In: *Scientific Reports* 3, p. 1383.

Meyer, Robert B et al. (1975). "Ferroelectric liquid crystals". In: *Journal de Physique Lettres* 36.3, pp. 69–71.

Michell, D and KL Biggs (1979). "Radiation cooling of buildings at night". In: *Applied Energy* 5.4, pp. 263–275.

Mills, David (2004). "Advances in solar thermal electricity technology". In: *Solar Energy* 76.1-3, pp. 19–31.

Moss, David J et al. (2013). "New CMOS-compatible platforms based on silicon nitride and Hydex for nonlinear optics". In: *Nature Photonics* 7.8, p. 597.

Narayanaswamy, Arvind, Sheng Shen, and Gang Chen (2008). "Near-field radiative heat transfer between a sphere and a substrate". In: *Physical Review B* 78.11, p. 115303.

Ni, George et al. (2016). "Steam generation under one sun enabled by a floating structure with thermal concentration". In: *Nature Energy* 1.9, nenergy2016126.

Nilsson, NA, TS Eriksson, and CG Granqvist (1985). "Infrared-transparent convection shields for radiative cooling: Initial results on corrugated polyethylene foils". In: *Solar Energy Materials* 12.5, pp. 327–333.

Nilsson, Torbjörn MJ and Gunnar A Niklasson (1995). "Radiative cooling during the day: simulations and experiments on pigmented polyethylene cover foils". In: *Solar Energy Materials and Solar Cells* 37.1, pp. 93–118.

Nilsson, Torbjörn MJ, Gunnar A Niklasson, and Claes G Granqvist (1992). "A solar reflecting material for radiative cooling applications: ZnS pigmented polyethylene". In: *Solar Energy materials and Solar cells* 28.2, pp. 175–193.

Ocier, Christian R et al. (2017). "Tunable Visibly Transparent Optics Derived from Porous Silicon". In: *ACS Photonics* 4.4, pp. 909–914.

Okawachi, Yoshitomo et al. (2011). "Octave-spanning frequency comb generation in a silicon nitride chip". In: *Optics Letters* 36.17, pp. 3398–3400.

Okuyama, Masanori et al. (1980). “Selective absorber using glow-discharge amorphous silicon for solar photothermal conversion”. In: *Solar Energy Materials* 3.3, pp. 405–413.

Otey, Clayton R, Wah Tung Lau, and Shanhui Fan (2010). “Thermal rectification through vacuum”. In: *Physical Review Letters* 104.15, p. 154301.

Peng, Yucan et al. (2018). “Nanoporous polyethylene microfibres for large-scale radiative cooling fabric”. In: *Nature Sustainability* 1.2, p. 105.

Querry, Marvin (1987). *Optical constants of minerals and other materials from the millimeter to the ultraviolet*. Tech. rep. Chemical Research Development and Engineering Center Aberdeen Proving Groundmd.

Raman, Aaswath P et al. (2014). “Passive radiative cooling below ambient air temperature under direct sunlight”. In: *Nature* 515.7528, pp. 540–544.

Rephaeli, Eden and Shanhui Fan (2008). “Tungsten black absorber for solar light with wide angular operation range”. In: *Applied Physics Letters* 92.21, p. 211107.

Rephaeli, Eden, Aaswath Raman, and Shanhui Fan (2013). “Ultrabroadband photonic structures to achieve high-performance daytime radiative cooling”. In: *Nano Letters* 13.4, pp. 1457–1461.

Rousseau, Emmanuel et al. (2009). “Radiative heat transfer at the nanoscale”. In: *Nature Photonics* 3.9, p. 514.

Rytov, Sergej M (1959). *Theory of electric fluctuations and thermal radiation*. Tech. rep. AIR FORCE CAMBRIDGE RESEARCH LABS HANSCOM AFB MA.

Sai, Hitoshi et al. (2003). “Solar selective absorbers based on two-dimensional W surface gratings with submicron periods for high-temperature photothermal conversion”. In: *Solar Energy Materials and Solar Cells* 79.1, pp. 35–49.

Sathiaraj, T Stephen et al. (1990). “Ni-Al2O3 selective cermet coatings for photothermal conversion up to 500 C”. In: *Thin Solid Films* 190.2, pp. 241–254.

Schuller, Jon A, Thomas Taubner, and Mark L Brongersma (2009). “Optical antenna thermal emitters”. In: *Nature Photonics* 3.11, pp. 658–661.

Shchegrov, Andrei V et al. (2000). “Near-field spectral effects due to electromagnetic surface excitations”. In: *Physical Review Letters* 85.7, p. 1548.

Shen, Sheng, Arvind Narayanaswamy, and Gang Chen (2009). “Surface phonon polaritons mediated energy transfer between nanoscale gaps”. In: *Nano Letters* 9.8, pp. 2909–2913.

Shi, Norman Nan et al. (2015). “Keeping cool: Enhanced optical reflection and radiative heat dissipation in Saharan silver ants”. In: *Science* 349.6245, pp. 298–301.

Silvestrini, Vittorio, Mario Peraldo, and Enrico Monza (1982). *Covering Element screening off the solar radiation for the applications in the refrigeration by radiation*. US Patent 4,323,619.

Sipe, John E (1987). "New Green-function formalism for surface optics". In: *JOSA B* 4.4, pp. 481–489.

Song, Bai, Yashar Ganjeh, et al. (2015). "Enhancement of near-field radiative heat transfer using polar dielectric thin films". In: *Nature Nanotechnology* 10.3, p. 253.

Song, Bai, Dakotah Thompson, et al. (2016). "Radiative heat conductances between dielectric and metallic parallel plates with nanoscale gaps". In: *Nature Nanotechnology* 11.6, p. 509.

Soum-Glaude, Audrey et al. (2017). "Optical characterization of TiAlNx/TiAlNy/Al2O3 tandem solar selective absorber coatings". In: *Solar Energy Materials and Solar Cells* 170, pp. 254–262.

Suichi, Takahiro et al. (2017). "Structure optimization of metallodielectric multilayer for high-efficiency daytime radiative cooling". In: *Thermal Radiation Management for Energy Applications*. Vol. 10369. International Society for Optics and Photonics, 103690E.

Sze, Simon M and Kwok K Ng (2006). *Physics of semiconductor devices*. John wiley & sons.

Thomas, Nathan H et al. (2017). "Semiconductor-based Multilayer Selective Solar Absorber for Unconcentrated Solar Thermal Energy Conversion". In: *Scientific Reports* 7.1, p. 5362.

Tong, Jonathan K et al. (2015). "Thin-film 'thermal well'emitters and absorbers for high-efficiency thermophotovoltaics". In: *Scientific Reports* 5, p. 10661.

Wang, Ning et al. (2011). "A novel high-performance photovoltaic–thermoelectric hybrid device". In: *Energy & Environmental Science* 4.9, pp. 3676–3679.

Weinstein, Lee A et al. (2015). "Concentrating solar power". In: *Chemical Reviews* 115.23, pp. 12797–12838.

Wu, Jia-Ye et al. (2017). "Diurnal cooling for continuous thermal sources under direct subtropical sunlight produced by quasi-Cantor structure". In: *Chinese Physics B* 26.10, p. 104201.

Xiao, T Patrick et al. (2018). "Electroluminescent refrigeration by ultra-efficient GaAs light-emitting diodes". In: *Journal of Applied Physics* 123.17, p. 173104.

Yablonovitch, Eli et al. (1986). "Unusually low surface-recombination velocity on silicon and germanium surfaces". In: *Physical Review Letters* 57.2, p. 249.

Yang, Deng-Ke (2014). *Fundamentals of liquid crystal devices*. John Wiley & Sons.

Yang, Ki Youl et al. (2016). “Broadband dispersion-engineered microresonator on a chip”. In: *Nature Photonics* 10.5, p. 316.

Yang, Yue and Liping Wang (2016). “Spectrally enhancing near-field radiative transfer between metallic gratings by exciting magnetic polaritons in nanometric vacuum gaps”. In: *Physical Review Letters* 117.4, p. 044301.

Yariv, Amnon and Pochi Yeh (2006). “Photonics: optical electronics in modern communications (the oxford series in electrical and computer engineering)”. In: *Oxford University Press, Inc* 231, p. 232.

Yeng, Yi Xiang et al. (2012). “Enabling high-temperature nanophotonics for energy applications”. In: *Proceedings of the National Academy of Sciences* 109.7, pp. 2280–2285.

Zhai, Yao et al. (2017). “Scalable-manufactured randomized glass-polymer hybrid metamaterial for daytime radiative cooling”. In: *Science* 355.6329, pp. 1062–1066.

Zhao, Bo et al. (2017). “High-performance near-field thermophotovoltaics for waste heat recovery”. In: *Nano Energy* 41, pp. 344–350.

Zheng, Ruiting et al. (2011). “Reversible temperature regulation of electrical and thermal conductivity using liquid–solid phase transitions”. In: *Nature Communications* 2, p. 289.

Zhiqiang, Yin (2005). “Development of solar thermal systems in China”. In: *Solar Energy Materials and Solar Cells* 86.3, pp. 427–442.

Zhou, Lin et al. (2016). “3D self-assembly of aluminium nanoparticles for plasmon-enhanced solar desalination”. In: *Nature Photonics* 10.6, p. 393.

Zhu, Jia, Kedar Hippalgaonkar, et al. (2014). “Temperature-gated thermal rectifier for active heat flow control”. In: *Nano Letters* 14.8, pp. 4867–4872.

Zhu, Jia, Zongfu Yu, et al. (2008). “Optical absorption enhancement in amorphous silicon nanowire and nanocone arrays”. In: *Nano Letters* 9.1, pp. 279–282.

Zhu, Linxiao, Anthony Fiorino, et al. (2019). “Near-field photonic cooling through control of the chemical potential of photons”. In: *Nature* 566.7743, p. 239.

Zhu, Linxiao, Aaswath P Raman, and Shanhui Fan (2015). “Radiative cooling of solar absorbers using a visibly transparent photonic crystal thermal blackbody”. In: *Proceedings of the National Academy of Sciences* 112.40, pp. 12282–12287.

Zhu, Linxiao, Aaswath Raman, and Shanhui Fan (2013). “Color-preserving daytime radiative cooling”. In: *Applied Physics Letters* 103, p. 223902.

Zhu, Linxiao, Aaswath Raman, Ken Xingze Wang, et al. (2014). “Radiative cooling of solar cells”. In: *Optica* 1.1, pp. 32–38.

Zou, Chengjun et al. (2017). “Metal-Loaded Dielectric Resonator Metasurfaces for Radiative Cooling”. In: *Advanced Optical Materials* 5.20, p. 1700460.